Physik Department

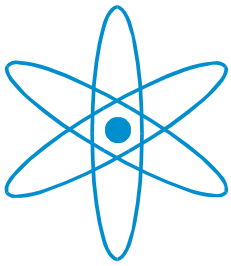

Inclusive $\Lambda(1116)$ production in p + Nb reactions at 3.5 GeV with HADES

Diplomarbeit
von

Oliver Werner Arnold

October 9, 2013

Technische Universität München
Excellence Cluster - 'Origin of the Universe'

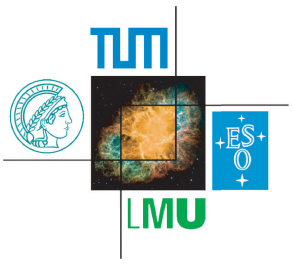

Abstract

The HADES detector is located in Darmstadt, Germany, at the GSI Helmholtzzentrum für Schwerionenforschung. It is a fixed target experiment, which was designed to measure rare dielectron e^+e^--pairs stemming from decays of light vector mesons inside a strongly interacting medium at beam energies of $1 - 2A$GeV. Several experimental runs were performed e.g. C+C, Ar+KCl or p+Nb reactions to study particle spectra and characteristics of different systems.
Despite the fact that the experiment was constructed for dilepton measurements it is also possible to identify hadrons with the spectrometer. This offers the additional possibility to investigate in-medium modifications of hadrons when they interact with a medium.
In this thesis we focus on the reconstruction of the strange $\Lambda(1116)$ baryon in the p+Nb system with a proton kinetic beam energy of 3.5 GeV. Because the Λ hyperon decays with a branching ratio of $\sim 64\%$ in the charged particle $p\pi^-$-pair it is possible to measure it with the energy loss in the Multi-Wire-Drift Chambers. We analyze $\sim 3.1 \cdot 10^9$ (downscaled) events from which we extract about 1M Λs. This large statistic allows us to perform a double differential analysis in two independent kinematic variables: the transverse momentum p_t and the rapidity of the particle y_{CM} in the nucleon-nucleon center of mass frame. The data measured with the HADES detector has to be corrected for acceptance and efficiency. We explain in detail how to correct for acceptance and efficiency effects and perform a so called self-consistency check to be sure that our correction is model independent.
To extract physical information from the experimental spectra we compare them to predictions of transport models, with which we simulate the p+Nb reaction. We have chosen two different models and present their structure to understand their similarities and differences and compare their predictions with the efficiency corrected two dimensional Λ phase space.
In the second part of the thesis we investigate the effect of particle correlations after they are emitted from a source, which is commonly known as final state interactions. This effect is based on the intensity interferometry technique, which compares a coincidence yield between the emitted particles to the product of their single-particle detection probabilities. Originally developed in radio astronomy to measure (angular) source sizes of astronomical objects it found its way to particle and nuclear physics, where it is used to gain information about the particle emitting source. We concentrate on the specific case of two-particle correlations between protons and describe how one determines the correlation function experimentally and introduce the theoretical Koonin-Pratt formalism which is used to extract the source size from the experimental signal.

Zusammenfassung

Der HADES Detektor befindet sich in Darmstadt an der Gesellschaft für Schwerionenforschung (GSI). Es ist ein Fixed-Target-Experiment, und wurde entwickelt um seltene Zerfälle von leichten Vektormesonen in einem stark wechselwirkenden Medium in Dielektronenpaare e^+e^- zu detektieren. Es wurden verschiedene Reaktionen wie z.B. C+C, Ar+KCl, oder p+Nb untersucht, um Teilchenspektren und Eigenschaften verschiedener Systemen zu studieren.
Ursprünglich wurde das Experiment zur Dileptonenidentifikation entworfen, jedoch ist es auch möglich Hadronen mit dem Spektrometer zu identifizieren. Dies ermöglicht beispielsweise auch die Untersuchung von Hadronmodifikationen, wenn diese in ein stark wechselwirkendes Medium eingebettet sind.
In dieser Arbeit konzentrieren wir uns auf die Rekonstruktion des Λ Hyperons, welches in p+Nb Reaktionen bei einer kinetischen Protonenergie von 3.5 GeV erzeugt wird. Das Λ Teilchen hat eine Zerfallsbreite von 64% in den $p\pi^-$ Kanal. Die geladenen Zerfallsteilchen können mit Hilfe der Energieverlustmethode in den Vieldraht-Driftkammern identifiziert werden, und dies ermöglicht die Rekonstruktion des Λ Mutterteilchens. Wir analysieren etwa $\sim 3.1 \cdot 10^9$ Events, und erhalten dadurch ca. 1M Λs als Ausbeute. Diese große Anzahl an Teilchen erlaubt es uns, eine doppelt differentielle Analyse in zwei unabhängigen Variablen, nämlich dem Transversalimpuls p_t und der Rapidität y_{CM} (im Nukleon-Nukleon Schwerpunktsystem) des Λ Teilchens, durchzuführen. Um die Daten mit theoretischen Modellen vergleichen zu können, muss eine Effizienzkorrektur durchgeführt werden. Wir werden die genauen Schritte der Korrektur erklären, und einen Selbstkonsistenztest vorstellen, mit dessen Hilfe wir sicher gehen können, dass die Effizienzkorrektur modellunabhängig ist.
Um physikalische Aussagen über unsere Spektren zu treffen, vergleichen wir diese mit Vorhersagen von Transportrechnungen. Wir haben uns für zwei verschiedene Modelle entschieden, und stellen deren Arbeitsweise vor, ihre Gemeinsamkeiten, und ihre Unterschiede.
Im zweiten Teil dieser Arbeit beschäftigen wir uns mit Effekten von Korrelationen zwischen Teilchen, nachdem diese eine Emissionsquelle verlassen haben. Teilchenkorrelationen basieren auf der Methode der Intensitätsinterferometrie, die ursprünglich in der Radioastronomie verwendet wurde um Quellradien von astronomischen Objekten zu bestimmen. Unabhängig davon fand die Technik auch Einzug in die Teilchen- bzw. Kernphysik, und wird dort verwendet um Informationen über Teilchenemissionsquellen zu gewinnen. Wir fokussieren uns speziell auf die Untersuchung von Zweiteilchenkorrelationen zwischen identischen Protonen. Wir zeigen sowohl wie man die experimentelle Korrelationsfunktion aus den Daten gewinnt, als auch den theoretischen Koonin-Pratt Formalismus mit dessen Hilfe wir Quellradien aus dem experimentellen Korrelationssignal gewinnen können.

Contents

1 Introduction

In the 20th century, one of the major problems of nuclear physics was the construction of a theory describing the forces between nucleons. The first attempt building a model for the nucleon-nucleon (NN) interaction was made by Yukawa [Yuk35] introducing the pion being exchanged between the nucleons, which was the starting point of the pion-theories. Yukawa's idea of one pion exchange was very successful describing NN scattering data [Mac11].
With the discovery of quantum chromodynamics (QCD), a new progress was made to understand the nature of strong interaction. QCD is a field-theory constructed on the basis of the gauge-principle using a local non-abelian $SU(3)_C$ color symmetry. Its ingredients are fermions, called quarks, and bosons, called gluons, arising automatically from the local gauge symmetry and acting as the force carrier between the quarks. Because the color symmetry is of non-abelian nature, it is the root of a rich class of new phenomena in comparison to abelian local gauge theories like quantum electrodynamics (QED). The main two features are known as asymptotic freedom, stating that the coupling between quarks and gluons becomes weaker at small distances, and the second one is confinement, according to which quarks and gluons are bound to colorless objects called hadrons (color singlets under $SU(3)_C$) in nature. Confinement leads to a constraint of possible groups of observable hadrons, yet experimentally confirmed were baryons containing three quarks and mesons containing a quark- anti-quark pair.
Theoretically confinement is described by the running coupling α_S of QCD, which is small for high energies and becomes larger for decreasing energies. Whereas in the high energy regime QCD can be treated perturbatively, at low energies the relevant degrees of freedom describing the dynamics of strongly interacting physical systems have to be exchanged, namely quarks and gluons for colorless objects of baryons and mesons. This is done by introducing the concept of effective field theory to low-energy QCD. Another important underlying global symmetry of QCD is used to connect both concepts, the chiral symmetry $(SU(2)_L \times SU(2)_R)$. Chiral symmetry is based on the fact that the masses of "up"- and "down" quarks (also the "strange" quark concerning three flavors) are relatively small (5-10 MeV/c^2) compared to the intrinsic scale of QCD $\Lambda_{QCD} \sim 350$ MeV, and it can be understood as the handedness also called chirality of the particles in the massless limit. Chiral symmetry is explicitly broken because of the finite quark masses, but also broken spontaneously to its vector subgroup $SU(2)_V$. The spontaneous symmetry breakdown to the QCD ground-state is associated with the appearance of massless pseudoscalar particles according to Goldstone's theorem - the pions (and kaons and the eta meson for three quark flavors). In this way we retrieve a theory with the structure of Yukawa's discovery, however constructed and constrained by symmetries of QCD. The force between hadrons can now be understood as a residual color interaction similar to the van der Waals force between neutral molecules [Mac11].

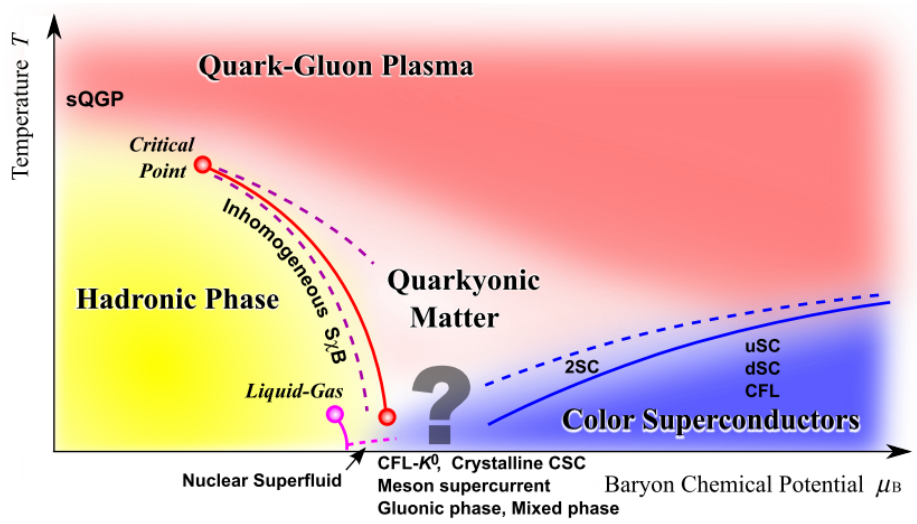

Figure 1.1: The phase diagram of QCD from [Fuk11].

1.1 Equation of state (EoS) of QCD matter

The fundamental behavior of QCD is that at high energies the coupling between quarks and gluons becomes weak, which is known as asymptotic freedom. It is therefore expected that QCD matter at high energy densities undergoes a phase transition from a state with confined hadrons into a new state of matter with quarks and gluons [Fuk11]. Such theoretical statements can be tested with heavy-ion colliders like the Relativistic Heavy-Ion Collider RHIC at Brookhaven National Laboratory or the Large Hadron Collider LHC at CERN. In general, QCD at finite density and temperature is described by the nuclear EoS, which defines a relation between state variables in thermal equilibrium. The complex phase diagram of QCD governed by its symmetries is shown in Figure 1.1. Besides the transition to a quark-gluon plasma (QGP), QCD predicts the condensation of quark Cooper pairs leading to the effect of color superconductivity (CSC) in the region of asymptotically high baryon density ($\mu_B \gg \Lambda_{QCD}$). In recent years continuous efforts have been made to explore the dense and cold region of QCD matter in the phase diagram realized in astrophysical objects like neutron stars. With the recent finding of a two solar mass neutron star [Dem10] new constraints for theoretical nuclear EoS for dense nuclear matter and their underlying microscopic models are available. The influence of the particle content of massive stars and the particle interactions on the stiffness of the EoS will be discussed in the next section.

1.2 The $\mathbf{\Lambda}(1116)$ hyperon and its possible role in neutron stars

Hyperons (Y) are baryons containing at least one strange quark. The $\mathbf{\Lambda}(1116)$ hyperon is part of the baryon octet and built of an up- down- and strange-quark. Hyperons may play an important role in dense systems like in the core of neutron stars. Calculated properties of a free gas of hadrons and leptons in β-equilibrium are showing that Λ hyperons appear at around $8n_0$ [Amb60], where n_0 is the nuclear saturation density. Including nuclear forces reduces the critical density to about $2n_0$ [Sah63]. Figure 1.2 illustrates a possible particle content for dense systems [Sch08a].

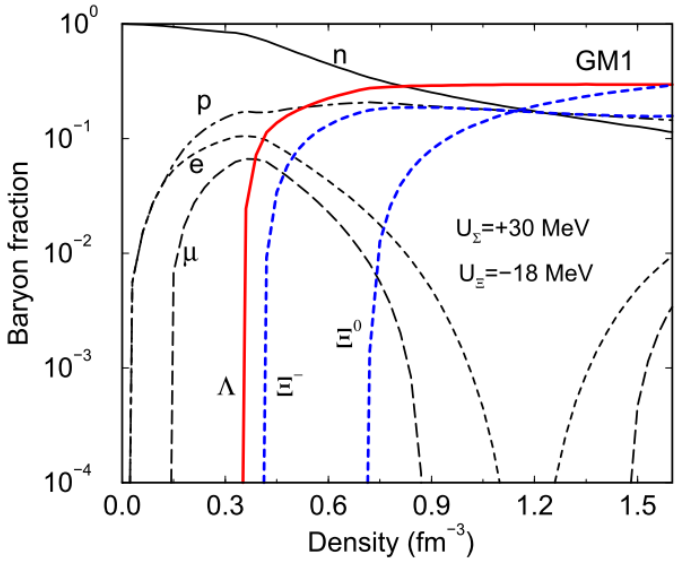

Figure 1.2: Baryon fraction as a function of density calculated with a relativistic mean-field model (RMF) according to [Sch08a]. Λ hyperons appear in this model at about $2.3n_0$.

Therefore, it is crucial to include the strong interaction among nucleons but also between nucleons and hyperons. To study the YN interaction in particular, one defines mathematically a single-particle potential U_Λ as the difference between the dispersion relation in-medium and the free one ($U_Y = \omega^* - \omega$) [Wan99a]. Physically, this potential describes the average field created by the other baryons and felt by the Λ. Different theoretical single-particle potentials for Λ hyperons as a function of density for symmetric nuclear matter [Dja10] are displayed in Figure 1.3. The black square represents the experimental value extracted from hypernuclei data $U_\Lambda(n = n_0)_{p=0} \approx -30$ MeV. Most curves coincide with experiment at saturation density, but differ at higher densities.

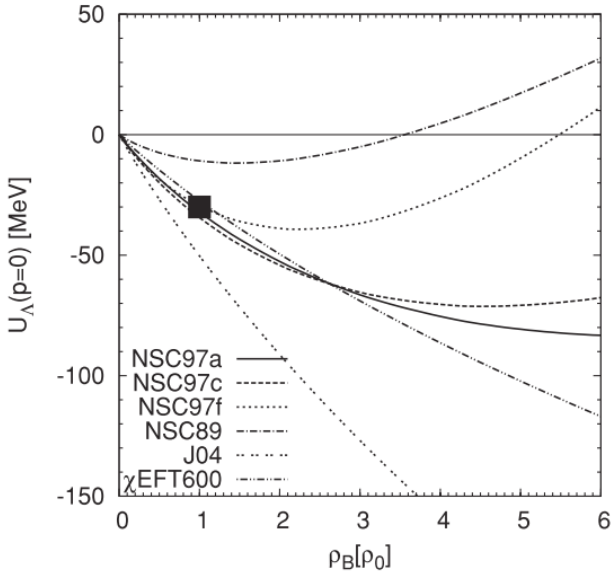

Figure 1.3: The Λ hyperon single-particle potential for symmetric matter, calculated for different models from [Dja10].

In general hyperons appear in dense matter if their in-medium energy is equal to their chemical potential $\mu(Y) = \omega(Y) = m(Y) + U_Y(\rho)$ [Sch08a]. It is then energetically favored that hyperons are produced via the weak decay of neutrons. Additional fermionic degrees of freedom, in this case hyperons, start then to populate new Fermi levels lower the overall Fermi energy and momentum of baryons and leptons, which leads to a reduced pressure of the system. This implies a softening of the EoS, compared to the pure nucleonic case. In a descriptive picture, high energetic nucleons are replaced by slowly moving more massive hyperons [Cha13].
The EoS is an ingredient of the Tolman-Oppenheimer-Volkoff (TOV) equations [Tol39] [Opp39], which are based on principles of general relativity and used to determine the maximum mass of a compact physical object. The TOV equation for a static spherical symmetric star in hydrostatic equilibrium is given by:

$$\frac{\mathrm{d}P}{\mathrm{d}r} = -\frac{G\rho\mathcal{M}}{r^2}\left(1+\frac{P}{\rho c^2}\right)\left(1+\frac{4\pi P r^3}{\mathcal{M}c^2}\right)\left(1-\frac{2G\mathcal{M}}{rc^2}\right)^{-1}. \tag{1.1}$$

The maximum mass calculated with help of Equation (1.1) must be in agreement with the discovery of a rather heavy neutron star PSR J1614-2230 with a measured mass of $1.97 \pm 0.04 M_\odot$ [Dem10].
Most models containing hyperons predict too low star masses. Sophisticated Brueckner-Hartree-Fock calculations generally give not larger masses than $1.6 M_\odot$. Also estimations of the maximum mass by the inclusion of three-body forces in such calculations (by introducing density-dependent contact terms) do not help to overcome the threshold of two solar masses [Vid11] as seen in Figure 1.5 (the authors point out that studies for more realistic three-body forces are needed). This strong softening of the EoS leads to a "hyperon puzzle" [Cha13], as hyperons appear in a "natural way" in dense systems, but are not able to produce large star masses.
Relativistic mean field (RMF) models also have problems describing such heavy stars and obtain masses in the range of $1.4 - 1.8 M_\odot$ (see [Wei12c] and included references). Some models obtain stiffer EoS by pushing the threshold density for the appearance of hyperons to larger values or using density dependent couplings (references are in [Wei12c]).
Another attempt is to insert the ϕ-meson into RMF models mediating the repulsive part of the YY-interaction and leading to stiffer EoS as suggested in [Wei12b]. In a recent study of the parameter space of a RMF model including the ϕ-meson, the authors question the underlying $SU(6)$ symmetry (a composite symmetry of flavor and spin of the quarks) which relates the couplings of hyperons to nucleons [Wei12c]. This also allows the possibility of N-ϕ interaction and results in stiffer EoS shown in Figure 1.4. The maximum mass of the star for different EoS is plotted versus the strangeness fraction (the number of strange quarks divided by the total number of quarks). By varying model parameters (and violating $SU(6)$) one decreases the strangeness fraction and enlarges the maximum mass.
In conclusion one can say, that the particle content in dense systems and the interactions among them is still a controversial topic. The finding of PSR J1614-2230 puts a tight constraint on possible EoS and most models with hyperon content struggle to reproduce such a large mass. The introduction of three-body forces does not help yet to reach large mass limits. There is also a discussion going on that even a heavier neutron star exists with a mass of about $2.4 M_\odot$ [van11] putting additional focus on the "hyperon puzzle" and aggravates it. An even stiffer EoS would then be needed, which means that already pure

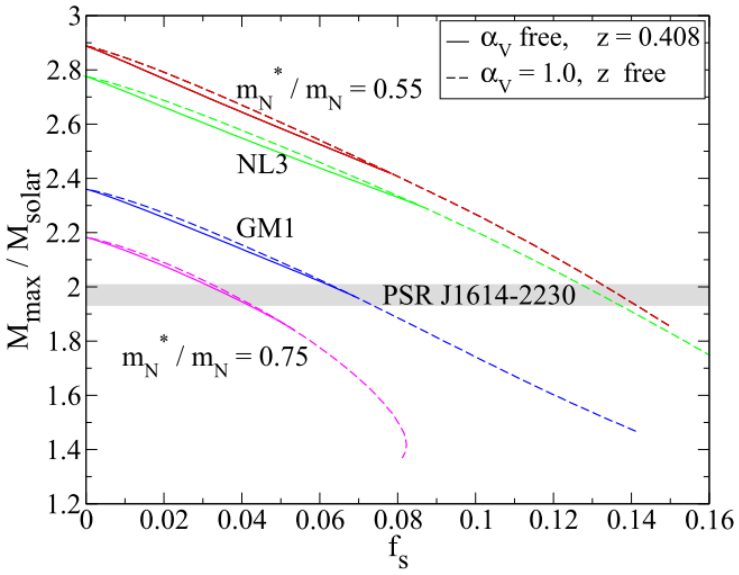

Figure 1.4: Maximum mass of a neutron star as a function of the strangeness fraction from [Wei12b]. Different curves are for different EoS. The violation of $SU(6)$ symmetry by varying the parameter sets (α_V, z) leads to different strangeness fractions. A decreasing strangeness fraction results in stiffer EoS and higher masses.

nucleonic models would have problems reproducing such a large mass.

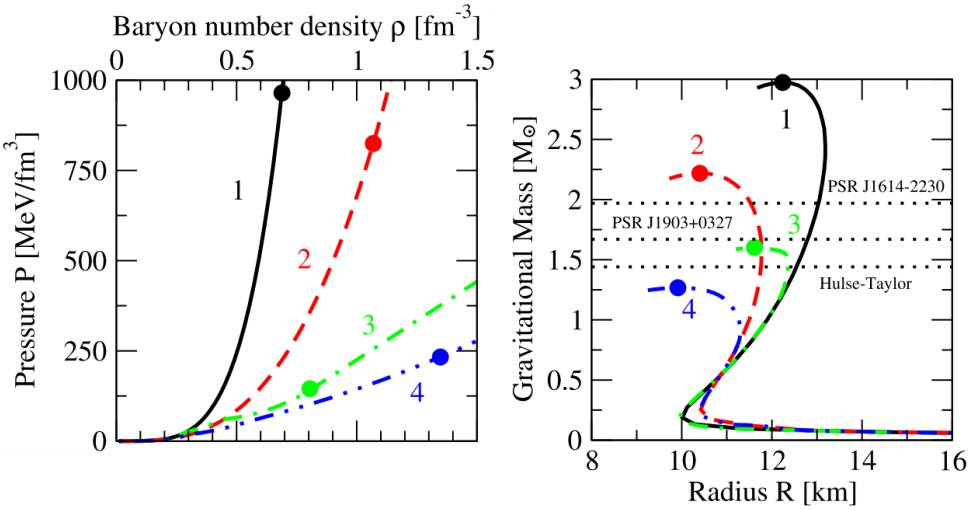

Figure 1.5: Different equations of state of nuclear matter and the connection to the mass of the object, according to [Vid11]. Calculations are based on Brueckner-Hartree-Fock theory including three-body forces. Curves 1 and 2 correspond to purely nucleonic stars, whereas 3 and 4 include hyperons. The inclusion of hyperons clearly softens the EoS and leads to lower neutron star masses.

1.3 Motivation of this work

As discussed in the preceding section, strangeness physics could have a large impact on physical, especially on global astrophysical observables like masses of heavy stars which act as huge laboratories where theoretical assumptions of nuclear EoS can be tested. Studying the dense EoS in terrestrial laboratories is done with heavy-ion experiments where two nuclei are collided to create highly excited nuclear matter reaching a few times saturation density. Because of their production threshold it is more probable that strange particles are produced in the early collision stage, thus carrying information of the system where the matter was in a compressed state. Especially kaons arouse interest, because of their long mean free path they pass relatively undistorted the medium and deal therefore as a probe of the dense region. Additionally it was shown on theory side that kaon production is sensitive to the EoS of nuclear matter [Aic85]. Experimental investigations of the stiffness of dense matter by measuring K^+ multiplicities in heavy-ion collisions followed [Stu01], which could explain their data with a soft EoS.
Apart from studying properties of the colliding medium with strange particles the particles behavior itself by embedding them in a strongly interacting environment became the focus of attention, measured with mean-field potentials which express the differences of particles to their vacuum characteristics. In heavy-ion runs a repulsive potential strength for neutral kaons was measured $U_{KN} \approx 38$ MeV [Aga10]. A different study of pion induced reactions on different targets reported a repulsive potential for K^0 of $U_{KN} \approx 20$ MeV [Ben09]. This discrepancy triggered further investigations of neutral kaons in p+p and p+A reactions measured with the HADES detector.
The production of kaons is closely connected to the production of Λs because of conserving strangeness in strong interaction processes. For this reason it was only natural that heavy-ion experiments were searching for modifications of Λ hyperons and an expected attractive potential by looking at flow observables [Li,98] [Li,96] [Wan99a]. The spectral shape of simulations showed a better agreement with the experimental results when an attractive mean-field was included as illustrated in Figure 1.6.

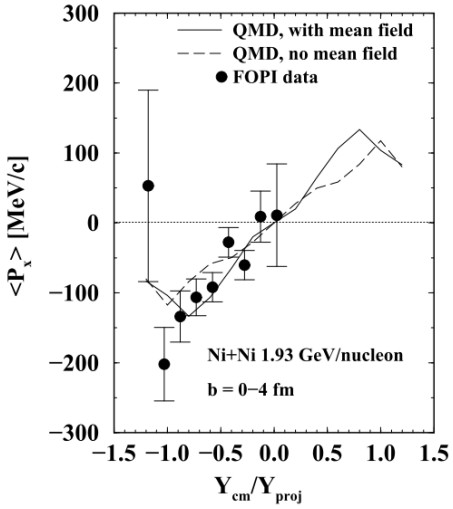

Figure 1.6: Study of the effect of a mean-field potential on Λ flow from [Wan99a].

As we have seen, most studies were performed with heavy-ion reactions where one has to deal with complex situations like evolving systems which implies a variation of the cross sections with density and particle propagation in very dense regions. One can reduce the complexity and also uncertainties with studying p+A reactions. They act as a link between elementary reactions and heavy-ion collisions. The target nucleus represents a well defined fixed environment with an average constant density n_0. This advantage is the starting point of our work. We analyze the inclusive Λ production in proton niobium (p+Nb) reactions with a proton kinetic energy of 3.5 GeV measured with the HADES detector. Besides the advantage of a fixed target density the experiment provides also a high statistic Λ sample which allows us to study hyperons in specific kinematic configurations to make precise statements about possibly particle modifications.

In the first part of this thesis we compare the experimental results with theoretical transport predictions. In the second part we employ a different study based on the so called intensity interferometry. If particles are emitted from a source there is a possibility that they get correlated due to final state interactions (FSI), measurable in the relative three-velocity of both particles in the center of mass frame of the pair.
Correlation measurements are on the one hand used to gain information about the particle emitting source and on the other hand they offer the possibility to learn more about the interaction between the emitted particles. For example the STAR collaboration could extract constrains on the scattering length about the very unknown interaction of $\bar{\Lambda}p$ and $\Lambda\bar{p}$ by looking at final state interactions [Ada06].
We want to use this method to study in future the interaction of Λs with protons by measuring their correlations and obtain also with this method information about the p+Nb particle emitting system. This would be a first measurement of Λp correlations in p+A reactions. However, in an intermediate step we have to develop all necessary tools to construct correlation functions which we tested in the construction of proton-proton correlations. This work will in detail be presented in Chapter 5.

2 The HADES Experiment

2.1 The HADES experiment and the aimed measurements

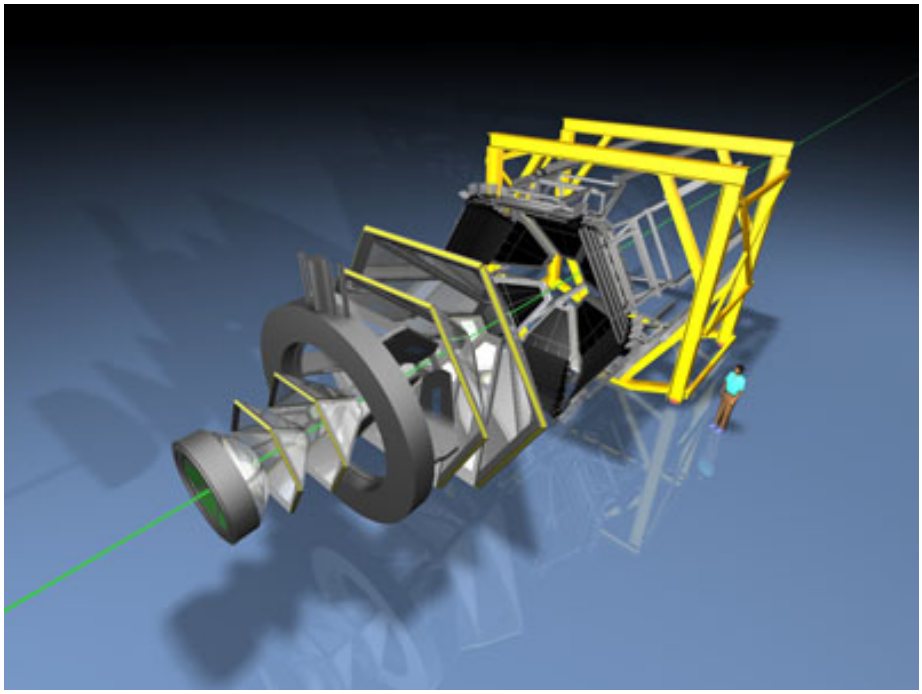

Figure 2.1: Setup of the HADES detector.

According to theoretical models, hadrons change their properties if embedded in a strongly interacting matter environment. To test such effects it is useful to measure particles which have a short lifetime, to enlarge the probability that they decay inside the medium. The light vector mesons ω, ρ and ϕ provide such properties. An additional advantage of these mesons is that they have electromagnetic decay channels into e^+e^- pairs, which are not subject to strong interactions and deliver a nearly undistorted signal of the matter phase [Aga09].
The **H**igh **A**cceptance **D**i-**E**lectron **S**pectrometer (HADES) was designed to measure such rare decays in fixed target reactions. It is located in Darmstadt, Germany, at the GSI Helmholtzzentrum für Schwerionenforschung. The HADES heavy ion program is focused on beam energies of 1-2 AGeV achieved with the heavy-ion synchrotron SIS18. At these energies the compression duration of colliding nuclei in heavy ion reactions is comparable to the lifetime of light vector mesons. Primarily designed for measuring electron pairs, it is also possible to measure hadrons with the detector setup. This allows one to investigate an even broader field of physics like the properties of strange hadrons [Sch08b], their production mechanisms in elementary reactions and their modifications in a cold nuclear environment. In the following sections all parts of the detector and their tasks are presented.

2.2 Experimental setup

2.2.1 Basic design

An expanded view of the HADES detector system is shown in Figure 2.1. It consists of six identical sectors defined by the superconducting coils arranged symmetrically around the beam axis optimized for dielectron measurements. It has an almost full azimuthal coverage of about 85% and covers the polar angle from $\Theta = 15°$ to $\Theta = 85°$. Figure 2.2 illustrates the schematic layout of the detector system and all the important detector parts.

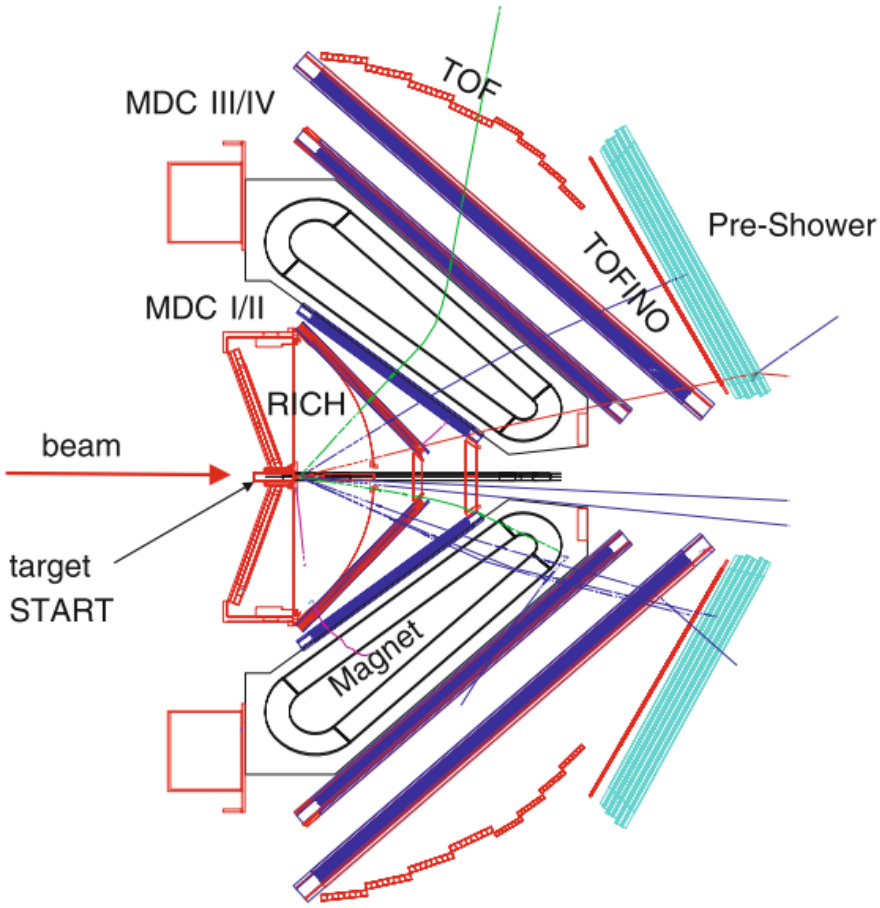

Figure 2.2: Side view of the HADES detector system and its detector components.

2.2.2 The target

The fixed target is located in front of the RICH detector. Elementary reactions are studied with a liquid hydrogen target, whereas for heavy-ion collisions or p+A reactions a segmented solid state target was used [Sie13]. A start detector delivers the starting time for the reaction time measurement (in the p+Nb run no start detector was used).

2.2.3 The RICH detector

The RICH (Ring Imaging Cherenkov) detector is used to identify electrons and positrons in the momentum range 0.1 GeV/c $\leq$ p $\leq$ 1.5 GeV/c. The detector contains as radiator gas

perfluorobutane (C_4F_{10}) with a Cherenkov threshold of $\gamma_{thresh} = 18$. Because of this large threshold the RICH detector is hadron blind in the SIS18 energy regime. The Cherenkov light generated by electrons and positrons while passing the radiator gas is reflected by a low mass carbon shell spherical mirror and finally hits the photosensitive CsI cathodes of six Multi-Wire Proportional Chambers (MWPC). Finally, the light is focused to rings because of the detector geometry in a way that the ring radius stays nearly constant. The information of the ring position together with a reconstructed particle track is used to identify electrons and positrons. A schematic layout of the RICH detector is given in Figure 2.3.

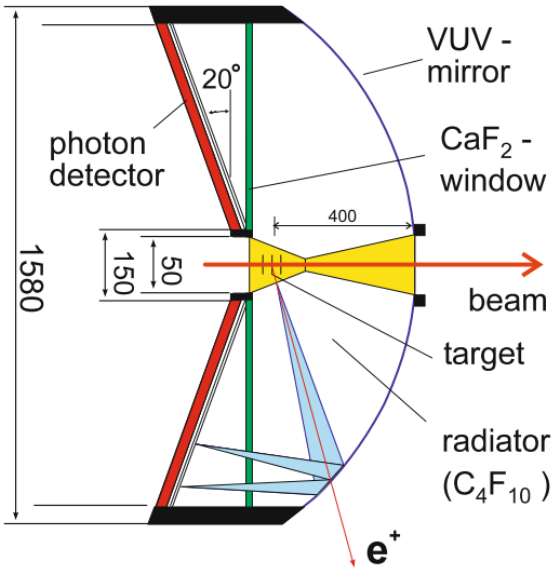

Figure 2.3: Schematic layout of the RICH detector. The Cherenkov light of the positron is reflected at the mirror and focused to a ring on the readout pads.

2.2.4 The Multi-Wire-Drift Chambers

The HADES program aims to measure in-medium modifications of particles. To reach this goal a good momentum reconstruction, which means a good spatial resolution of the tracked particles together with a large detector acceptance is needed. Therefore, 24 trapezoidal planar **M**ulitwire **D**rift **C**hambers MDC are placed symmetrically around the beam axis in six identical sectors. Each sector contains four tracking planes (I-IV), two planes in front (I-II) of the magnet and two behind (III-IV) as illustrated in Figure 2.2. The place between the planes II-III defines the active area of the chambers, where charged particles are deflected thanks to the magnetic field. Each of the 24 MDCs are divided into six anode wire frames (about 1100 tungsten wires per frame) oriented in six different angles ($\pm 0°, \pm 20°, \pm 40°$) as displayed in Figure 2.4. This setup enlarges the spatial resolution in polar direction.

The chambers are flushed with a counting gas. A charged particle traversing the gas is ionizing it along the particle trajectory forming so called clusters. The produced electrons in the gas are accelerated towards the wires because of an active electric field. The amount of electrons is multiplied during the acceleration by the avalanche effect and finally the cloud of electrons reaches the wires and introduces an electric signal, which can be read out.

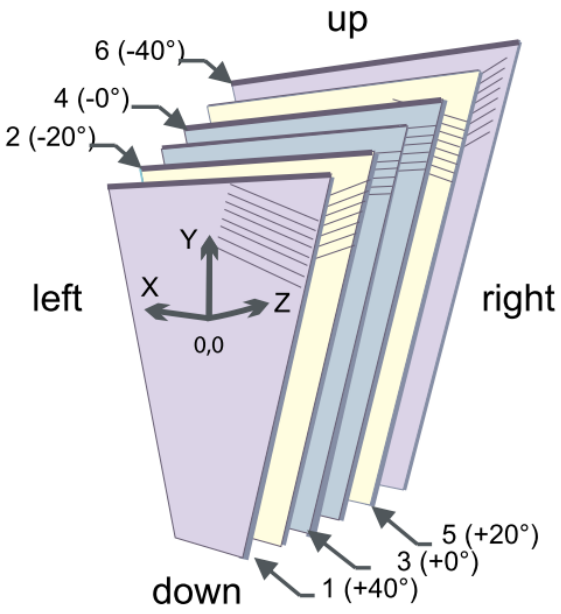

Figure 2.4: Schematic view of the drift chambers oriented at $\pm 0°, \pm 20°, \pm 40°$.

With this principle hit positions in the MDC layers (I-IV) are determined. The hit points in MDC I and II are grouped together to an inner track segment and from MDC III and IV to an outer one. The points in the inner and outer segment are connected with the assumption of straight tracks, because they are in an almost free magnetic field region. In the active area the particles are deflected and the momentum is determined solving its equation of motion in the field region in a recursive way with the Runge-Kutta method using the hit points as initial conditions.

2.2.5 The Magnet

A charged particle entering a magnetic field region is deflected according to the Lorentz force, whereas the total momentum stays constant. By measuring the deflection one is able to obtain the momentum of the particle. To make use of this principle, the HADES detector contains six superconducting magnets placed around the beam axis among the drift chambers. The magnets create a strong inhomogeneous toroidal magnetic field with field strengths ranging from $B = 0.9$ T up to $B = 3.6$ T at the sector edge. The magnet was built in such a way that the target region and the active volume of the RICH detector is free of any magnetic field to not influence the particle reactions and identification of electrons and positrons.

2.2.6 The Time-of-flight detectors

The three time of flight detectors are part of the Multiplicity Electron Trigger Array META system. Particles traversing the META system give an additional hit point which is used for momentum reconstruction. The detector subsystems are in detail:

- TOF detector
  The TOF detector covers a polar acceptance of $44° < \Theta < 88°$ and follows the

azimuthal six-fold symmetry of the whole HADES setup. Each one of the six detectors consists of eight modules, and each module is subdivided into eight scintillator rods. A charged particle induces a photon emission in the scintillators measured with Photo-Multiplier-Tubes PMT's, which deliver the arrival time and also a signal height. The signal height is related to an energy loss, which can be used for particle identification. The time resolution of the TOF detector was obtained by using dileptons from C+C reactions and is of the order $\sigma_{\mathrm{TOF}} \approx 150$ ps.

- TOFINO
  The TOFINO detector has a polar acceptance of $18° < \Theta < 45°$. It is a low granularity system divided into six sectors each containing 4 scintillator paddles with a trapezoidal form. The lower granularity increases the probability of double hits. Its time resolution is worse than those of the TOF of about $\sigma_{\mathrm{TOFINO}} \approx 420$ ps.

- Pre-Shower
  The Pre-Shower is located just behind the TOFINO detector. It is used for dilepton identification and based on the fact that electrons and posistrons induce an electromagnetic shower in the converter made out of lead.

- Resisitve Plate Chambers (RPC)
  To achieve better time resolutions of about $\sigma_{\mathrm{RPC}} \approx 100$ ps, which leads to an improved particle identification and to be able to work at SIS intensities of $2 \cdot 10^7$ Hz, expected in Au+Au collisions at 1.5 GeV/A [Alv04], the new RPC wall ESTRELA (Electrically Shielded Timing RPC Ensemble for Low Angles) was developed and exchanged for the TOFINO detector [Gil07] in an upgrade which started in 2009. It covers the low polar angle acceptance region $18° < \Theta < 45°$ with 2π azimuthal coverage.

2.2.7 The Forward Wall

HADES started in 2007 to investigate proton deuteron reactions. A characteristic feature of these reactions is that spectator nucleons move in forward direction at small polar angles. The HADES spectrometer covers polar angles from $15° < \Theta < 85°$, not able to register these spectators. For this purpose, a forward wall scintillator hodoscope was built. It consists of about 300 scintillating cells having a thickness of 2.54 cm each and are read out by photomultipliers [Lap09]. It was placed 7 m downstream the target and covers a polar acceptance of $0.33° < \Theta < 7.17°$.

3 Inclusive $\Lambda(1116)$ analysis

3.1 The p+Nb experiment

The experiment was performed in September 2008. Protons with a kinetic energy of $T_p = 3.5$ GeV were incident on a 12-fold segmented niobium target. The niobium target was chosen because it is a good compromise of maximizing the number of in medium decays of ρ and ω mesons and keeping the γ conversion probability low since the main aim of the experiment was to study the virtual photons stemming from the ω and ρ mesons produced in cold nuclear matter [Tec06]. The target was also used in other experiments e.g. JLAB, which offers the possibility of consistency checks with additional data. Details of the run are listed in Table 3.1 [Lor12].

Beam energy T_p	3.5 GeV
Average beam intensity	$2 \cdot 10^6$ particles/s
Target	$^{93}_{41}$Nb
Target diameter	$d = 2.5$ mm
Number of segments	12
Distance between segments	$\Delta z = 4.5$ mm
Thickness of segment	$t = 0.45$ mm
Interaction probability	2.8%
Downscaled Events	$3.15 \cdot 10^9$

Table 3.1: Information about the p+Nb run performed in September 2008.

This run allows the study of different particle species. We are interested in the search of strange Λ hyperons, inclusively. Inclusive in this sense means that we only identify the Λ and do not study additionally produced particles in the event like protons, pions, or even other strange particles.

$p + Nb \rightarrow \Lambda + X$

The production threshold for a Λ in elementary collisions is closely connected to the threshold of Kaons in particular K^+ and K^0 because of strangeness conservation. The simplest channels to produce Λs are:

$$p + p \rightarrow p + K^+ + \Lambda$$

$$p + n \rightarrow p + K^0 + \Lambda$$

The threshold kinetic energy of protons to produce these three particles is 1.58 GeV or in units of the invariant collision energy $\sqrt{s}_0 = m_K + m_\Lambda + m_p = 2.55$ GeV. At our energies we reach $\sqrt{s} = 3.18$ GeV which means we are above the threshold and can produce additional particles in the channels stated above like additional $\pi^\pm\pi^\mp$-pairs (excess energy $\varepsilon = \sqrt{s} - \sqrt{s}_0 \approx 0.63$ GeV).

3.2 Particle identification

The HADES framework was mainly built to identify dileptons with the RICH detector which is hadron blind. The MDCs provide besides the momentum determination the information of the energy loss of a particle with the measured time over threshold (ToT), which is the time that an electronic signal exceeds an adjusted threshold. The time over threshold is related to the energy loss of the particle $ToT = f(dE/dx)$.
The principle of energy loss is that a charged particle which crosses a medium scatters inelastically with electrons bound in atoms in the medium. This causes an energy loss of the traversing particle. At each collision process n the particle loses the energy $E_n - E_0$ and it collides with a rate (per unit length) of $N\sigma$ where σ is the cross section. This motivates the ansatz for the energy loss [Sak94]:

$$\frac{\mathrm{d}E}{\mathrm{d}x} = N \sum_n (E_n - E_0) \int \frac{\mathrm{d}\sigma}{\mathrm{d}\Omega}\, dq. \tag{3.1}$$

A full relativistic treatment was given by Bethe and Bloch in the famous Bethe-Bloch formula [Bet30]:

$$-\left\langle \frac{\mathrm{d}E}{\mathrm{d}x} \right\rangle = 4\pi N_A r_e^2 m_e c^2 z^2 \frac{Z}{A} \frac{1}{\beta^2} \left[\ln\left(\frac{2m_e c^2 \beta^2 \gamma^2 T_{max}}{I^2} \right) - \beta^2 - \frac{\delta}{2} \right]. \tag{3.2}$$

The factors in detail are:

z : charge of the incident particle
Z,A : atomic and mass number of the traversed medium
m_e : rest mass of the electron
r_e : Bohr electron radius
N_A : Avogadro number
I : mean excitation potential of the material
δ : density correction
T_{max} : maximum kinetic energy which can be transferred

Equation (3.2) depends on the charge ($z \cdot e$) and on the momentum ($p/m = \gamma\beta$) of the particles. Through the dependence of the momentum on the mass we expect different curves for different particle species and this separation allows one to identify them.
We want to use this basic principle to reconstruct the unstable and charge neutral Λ hyperon which has a mass of $m_\Lambda = 1115.683 \pm 0.006$ MeV/c ^{2} and a mean lifetime of $\tau_\Lambda = (2.632 \pm 0.020) \cdot 10^{-10}$ s [Gro08]. Thanks to the short lifetime the Λ decays already inside the HADES detector which makes it possible to identify it via its decay products. The decay modes are listed in Table 3.2 extracted from [Gro08].

Decay Mode:		*Fraction* Γ_i/Γ_{tot}
Γ_1	$p\pi^-$	$63.9 \pm 0.5\%$
Γ_2	$n\pi^0$	$35.8 \pm 0.5\%$
Γ_3	$n\gamma$	$(1.75 \pm 0.15) \cdot 10^{-3}$
Γ_4	$p\pi^-\gamma$	$(8.4 \pm 1.4) \cdot 10^{-4}$
Γ_5	$pe^-\bar{\nu}_e$	$(8.32 \pm 0.14) \cdot 10^{-4}$
Γ_6	$p\mu^-\bar{\nu}_\mu$	$(1.57 \pm 0.35) \cdot 10^{-4}$

Table 3.2: Listing of Λ decay modes.

The decay modes $\Gamma_i,\ i > 2$ can be neglected because they are very improbable to occur. Due to the lack of a calorimeter in the HADES setup it is also not possible to detect any of the neutral particles in the second decay channel, e.g. with the identification of $\pi^0 \to \gamma\gamma$. The channel $p\pi^-$ is the dominant one and the energy loss of the charged decay products can be measured in the MDCs.
Figure 3.1 shows the energy loss as a function of momentum and polarity of all charged particles in the p+Nb experiment registered and measured in the MDCs. The identification of protons and negative pions is made with graphical cuts around the theoretically predicted Bethe-Bloch curves according to Equation (3.2). Because the energy loss and momentum are smeared by finite resolution effects of the detector, we always have to choose broader cuts than the optimal theoretical curves.

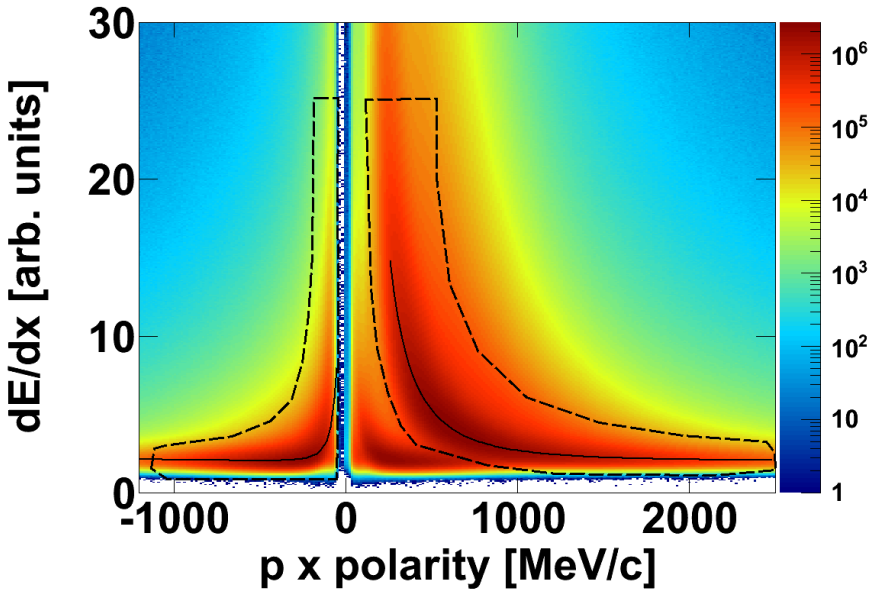

Figure 3.1: Energy loss as a function of momentum and charge obtained from measurements in the MDCs. Solid lines are theoretical Bethe-Bloch curves for protons and negative pions. Dashed lines are graphical cuts used in this analysis for particle identification.

The reconstruction of the Λs is done with the invariant mass technique. The HADES detector measures the 3-momentum and the energy loss of the particle. The latter is used for identification which provides us with the full 4-vector information after knowing the particle and its corresponding mass. Constructing the invariant mass of a proton-pion pair should result in a mass of about 1116 MeV/c^2 if the mother particle was a Λ.

$$p_\mu p^\mu = m_\Lambda^2 = (1116\ \mathrm{MeV/c^2})^2 = E_\Lambda^2 - \vec{p}_\Lambda^{\,2} = (E_p + E_{\pi^-})^2 - (\vec{p}_p + \vec{p}_{\pi^-})^2. \tag{3.3}$$

This variable is the cornerstone of the analysis. It is Lorentz invariant by construction and can easily be investigated with several auxiliary conditions which will be explained in detail in further sections.

3.2.1 Trigger conditions

As already mentioned, the HADES detector aims for detecting rare e^+e^- pairs stemming from decays of light vector mesons. To suppress purely hadronic channels, an event filtering procedure (trigger system) is included in the setup. It also helps to avoid overloading of the data acquisition system and of the front-end electronics. The trigger system consists of two different trigger conditions:

- **LVL1 Trigger** :
  The TOF and TOFINO detectors (building the META system) determine the multiplicity M of an event. The first level trigger (LVL1) rejects events that do not exceed an predefined multiplicity condition. In the p+Nb run a M3 trigger was used registering only events with at least three hits in the META system. The effect of this operation is twofold. Firstly, from all occurred minimum biased events only a

subclass is selected which are called LVL1 events. Secondly, this selected subclass contains events coming from more central regions of the nucleus as can be seen in the impact parameter distribution shown in Figure 3.2. Indeed, the probability to produce M3 events is larger for more central events due to the fact that the particles have a higher chance to produce secondary particles in the nucleus. The selection of more central events has an influence on the multiplicity of the Λ hyperon, also shown in Figure 3.2 where in the right panel the Λ multiplicity as a function of the trigger condition is displayed. By modifying the trigger condition by raising the necessary hits in the META system the Λ multiplicity increases.
The trigger factor associated with M0 and M3 trigger events is calculated with help of simulations (UrQMD and GiBUU). It is defined as the ratio of multiplicities for the desired particle (in this case hyperons) inside the HADES acceptance determined with the M3 and with the M0 trigger decisions (M0 is the trigger logic to collect minimum biased events which are events with hypothetical multiplicity $M_{LVL1} = 0$):

$$\mathcal{F} = \frac{N_{\Lambda}^{acc}/N_{LVL1}(M3)}{N_{\Lambda}^{acc}/N_{LVL1}(M0)}. \tag{3.4}$$

This quantity slightly depends on the particle under investigation. The Λ provides with its decay products already two particles ($p\pi^-$) and only one additional META-hit is needed to obtain a positive LVL1 trigger signal whereas e.g. for K^+ two more hits are needed.

- **LVL2 Trigger** :
  The second level trigger (LVL2) is important for lepton analysis. During a run, data samples recorded by the corresponding detector parts are evaluated by Image Processing Units (IPU) for possible lepton signatures like RICH-rings. The Matching Unit (MU) connected to all IPUs correlates the signatures and provides a trigger decision (e.g. at least one ring is needed to give a positive trigger decision).

- **Downscaled Events**
  We are only interested in hadronic reactions and do not consider the LVL2 trigger decision. To not introduce any trigger bias into the data sample the term downscaled event was invented. In the data acquisition process the LVL2 trigger gives a positive signal if there is a sign for a leptonic event. Only events with a positively LVL1 and LVL2 decisions are recorded except for a fixed fraction of events independent of the second level trigger decision. These events are called downscaled events. The amount of LVL1 events recorded without paying attention to the LVL2 trigger output is fixed by the downscaling factor DS. In the p+Nb run DS was set to three which means that every third event was written to tape. Downscaled events become denoted by a DS1 flag which can afterwards be used to distinguish them from other events in the hadron analysis. For more details we refer to [HAD05].

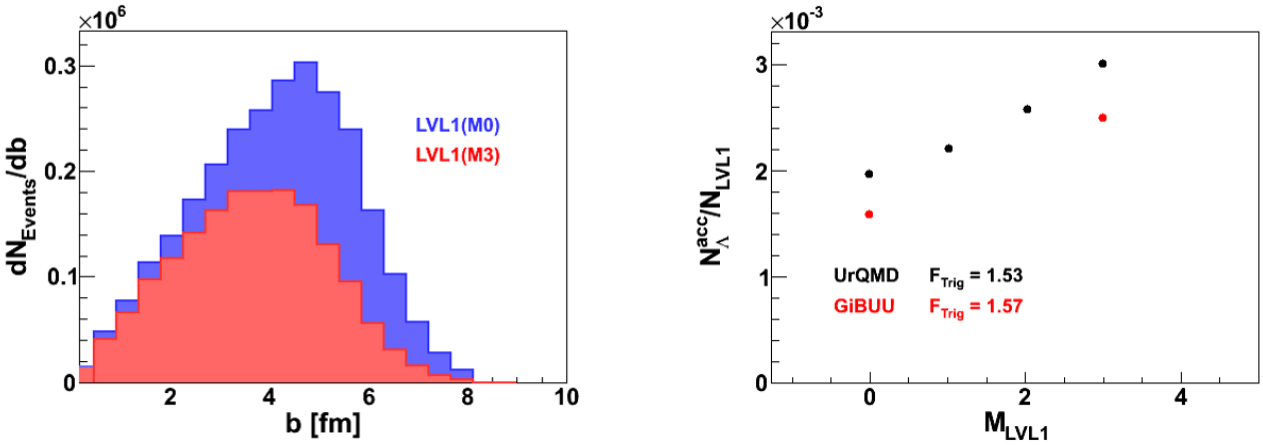

Figure 3.2: Left: Effect of the LVL1 trigger determined with UrQMD simulations. By switching the M3 trigger on, the total amount of events is reduced but also more central events are selected.
Right: Multiplicity dependence of Λ hyperons on the selected trigger condition. The multiplicity increases with the trigger condition. The trigger factor is explained in the text.

3.2.2 Topological Cuts - Primary Vertex

As mentioned before, the niobium target is a 12-segmented solid state target. The reaction takes place in the niobium discs. Each particle registered by HADES is tracked and the tracking information can be read out. To suppress background contamination from other sources like secondary particles produced not in the niobium discs we employ a primary vertex cut to analyze only events where the particles come from the target region.
Technically, one uses the track information of each particle and calculates the primary vertex. This is done by obtaining the intersection points of all tracks with each other or the points of closest approach if the tracks do not intersect. The mean value of all calculated points is the primary vertex position. If the primary vertex does not lie inside the target region the event is rejected. The resolution of the vertex reconstruction is not sufficient to distinguish the individual target discs. For this reason we apply the weaker cut condition that the primary vertex lies inside a cylinder spanned by the discs illustrated in Figure 3.3. A larger radius of the cylinder is chosen in comparison to the disc radius of the target to consider finite vertex resolution effects. Its dimensions are $r = 5$ mm radius, and $L = 60$ mm length.

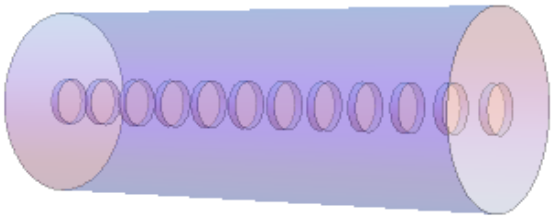

Figure 3.3: Target cylinder with embedded niobium discs. If the primary vertex lies inside the cylinder the event is analyzed further otherwise it gets rejected.

Projections of the cylinder in the x-y and x-z direction prepared with experimental events can be seen in Figure 3.4. The target cylinder is shifted in x direction by a mean value of $\Delta\bar{x} = 2$ mm, to match the shift of the beam position of 2 mm.

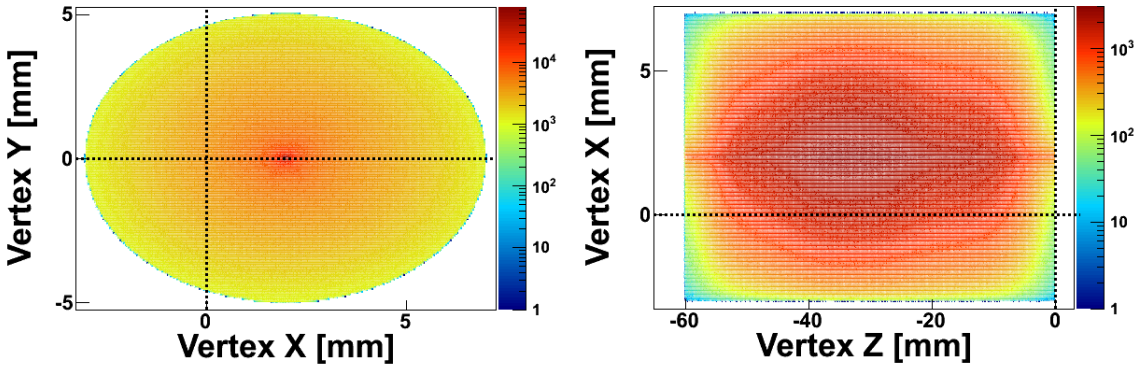

Figure 3.4: Projections of the target cylinder on the x-y and x-z plane. The resolution of the primary vertex does not allow to resolve the 12 niobium discs.

3.2.3 Topological Cuts - Secondary Vertex

The primary vertex cut was used to constrain an event by the requirement that the primary vertex should lie inside the target region. If an event passes this cut it is analyzed further. In our particular case the remaining events are scanned for Λ hyperons. This is done by combining protons and negative pions to pairs with the invariant mass technique. Frequently in Λ events other protons and pions are produced or other particles are accidentally identified as protons and pions. The combination of them gives us a non-Λ background signal. To reduce this background source one applies secondary off-vertex cuts. This is mainly possible due to fact that the Λ has a finite lifetime, which is translated into a "distance" $c\tau = 3 \cdot 10^8 \frac{\mathrm{m}}{\mathrm{s}} \times 2.6 \cdot 10^{-10}$ s ≈ 7.8 cm in the center of mass frame of the Λ. Transforming this value to the laboratory frame gives us a rough estimation how far the produced Λs are flying at SIS energies (we call this distance Δs):

$$\begin{pmatrix} ct \\ \Delta s \end{pmatrix} = \begin{pmatrix} \gamma & \gamma\beta \\ \gamma\beta & \beta \end{pmatrix} \begin{pmatrix} ct' \\ \Delta s' \end{pmatrix} \overset{\text{CMS}}{=} \begin{pmatrix} \gamma & \gamma\beta \\ \gamma\beta & \beta \end{pmatrix} \begin{pmatrix} c\tau \\ 0 \end{pmatrix} \tag{3.5}$$

The relation $\Delta s = \gamma\beta c\tau = \frac{p}{m} c\tau$ follows from Equation (3.5). With a mean Λ momentum at our energies of about 700 MeV/c we obtain a distance $\Delta s \approx 4.8$ cm that a Λ flies before it decays. This circumstance allows us to introduce four secondary off-vertex cuts shown in Figure 3.5. The procedure is the following. With the proton and pion track one calculates the secondary decay vertex (which is usually the point of closest approach), evaluates a hypothetical Λ track and calculates the primary vertex with all other particles in the event. Together with the decay vertex information one extracts the distance between the primary vertex and secondary vertex Δs, which is then used as a cut parameter.
The distance between the decay product tracks can also be used to suppress background contamination. If the mother particle was a Λ both tracks should not be far apart denoted by $MinTrackDist$ (standing for minimum track distance).
The last two off-vertex cuts are the distances of closest approach $(VerDist(p), VerDist(\pi^-))$ between the proton and pion track to the primary vertex. Tracks stemming from a Λ

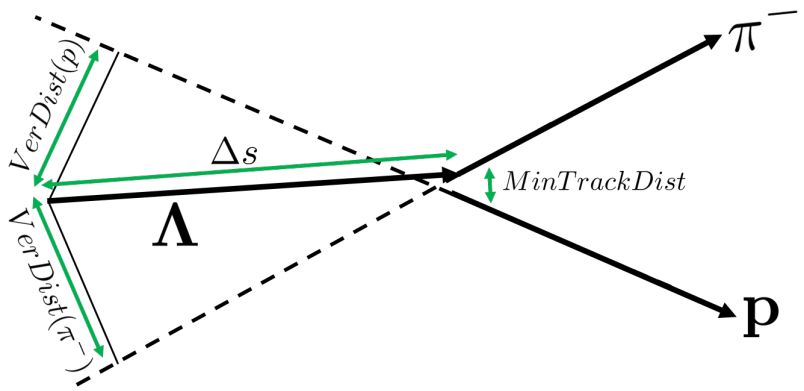

Figure 3.5: Illustration of secondary vertex cuts.

decay usually have a minimum distance to the primary vertex, displayed in Figure 3.5. This circumstance allows us to distinguish better between e.g. protons from Λs and other protons.
We have now four parameters whereby Δs should lie in a region indicated by the estimated value which we calculated above. One has to find a good combination of all four parameters to suppress the background and enlarge the Λ signal. This is done with maximizing two variables the signal to background ratio S/B which selects configurations where the background contamination is low and the ratio of S^2/B to enlarge the signal. In doing so, one chooses proper start values (the very first parameter values are simply guesses and from the best obtained parameter set one starts the study again), and varies one cut value whereby the other three are kept fixed obtains S/B and S^2/B and takes the next cut value to start the two ratio calculations of the signal and background again. In the analysis a good cut combination was found to be the one which is listed in Table 3.3:

Cut parameter	*Value [mm]*
MinTrackDist	< 10
VerDist(p)	> 4
VerDist(π^-)	> 10
Δs	> 43

Table 3.3: Set of parameters chosen in the analysis to enlarge the Λ signal and suppress background contamination.

3.3 Performing the $\mathbf{\Lambda}(1116)$ analysis

In the last section we explained all important tools to search for Λ hyperons in the HADES data sample. In this section we will apply them. We have to find a proper phase space region for the study, this means we have to find the region of the phase space which is mainly populated by hyperons. Later we will see that the Λ statistic is large enough to perform a double differential analysis in two independent variables. Another effect we have to consider is the finite acceptance of the HADES detector. Mainly because of its geometry,

the detector covers only a certain part of the full particle phase space and measures the particles with a finite efficiency mainly due to geometrical cuts we perform in the analysis. The data can be corrected for such effects with help of simulations. This will also be presented in the next sections.

3.4 Primary vertex of Λ hyperons

As shown in section 3.2.2 the production vertex should lie inside the target cylinder to reduce background sources. We discussed this issue for all experimental events, but now we want to concentrate especially on the vertex position of the Λ. To study this, we divide the cylinder in position bins and obtain the invariant mass spectra in these bins. Subsequently, we fit the spectra, subtract the background and obtain the signal. The dimensions of the target cylinder $-3 < x < 7$ mm $-5 < y < 5$ mm and $-60 < z < 0$ mm was divided in 40 position bins, respectively. The results are shown in Figure 3.6, where the Λ distribution as a function of the three primary vertex positions is plotted. The black points illustrate the experimental data points and red are simulation predictions.
For efficiency correction, which we will explain later, we have to select a simulation model. The model output should be close to the experimental observables to deliver a reasonable efficiency correction. For this reason we compare the experimental data with the chosen UrQMD simulation [Bas98].

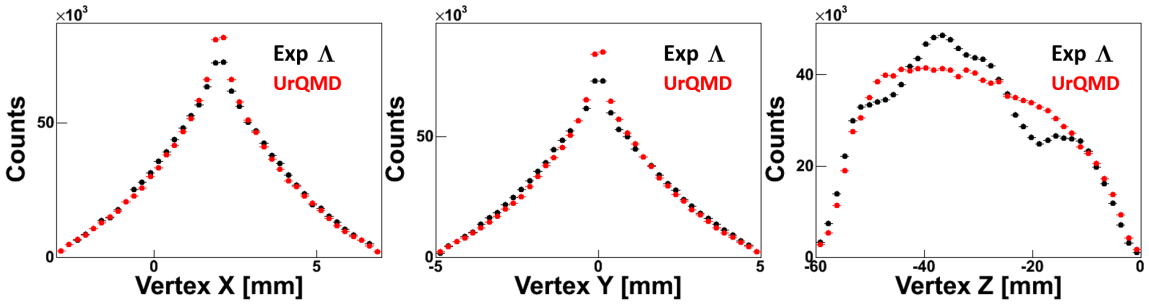

Figure 3.6: Primary vertex positions for experimental Λs (black) in comparison with the UrQMD transport model (red).

Figure 3.6 shows that the x and y components are well described by simulations. Most Λs are produced in the center of the target as we would expect. In the z component we have some discrepancies noticeable in an unsteady behaviour of the experimental curve. In the simulation framework we also included the 12 niobium discs geometry perfectly aligned, which results in a smooth simulation curve. Because of the unsteady experimental curve the conjecture appeared that some target discs were fallen out from their target position and were not hit by the beam. This hypothesis was excluded after the target was X-Rayed as shown in Figure 3.7 [Web11]. All 12 discs were inside of the carbon tube, however, they showed some misalignment and individual discs were slightly tilted and shifted from their designated position which explains the irregular behaviour in the z-vertex distribution.

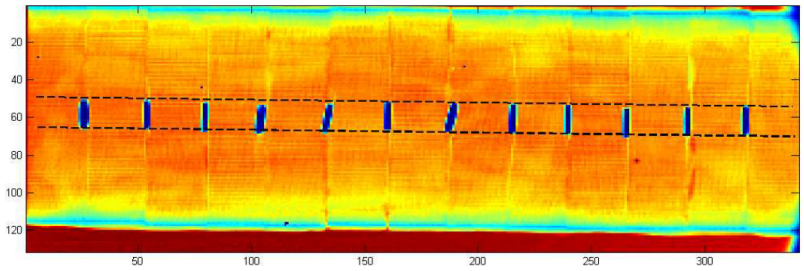

Figure 3.7: X-Ray capture of the target taken from [Web11]. The 12 niobium discs are depicted in blue color. The dashed lines show the deviation from a linear alignment. Some discs were slightly tilted.

3.5 Secondary off-vertex position for Λ hyperons

The same strategy of section 3.4 was applied to the four secondary vertices, which are presented in Figure 3.8 together with the cuts we use to enlarge the Λ signal. The experimental Λ distribution as a function of the secondary vertices is again plotted in black and UrQMD predictions in red. The UrQMD model is able to describe the shape of the vertex distributions. It is therefore reasonable to use this model for efficiency corrections.

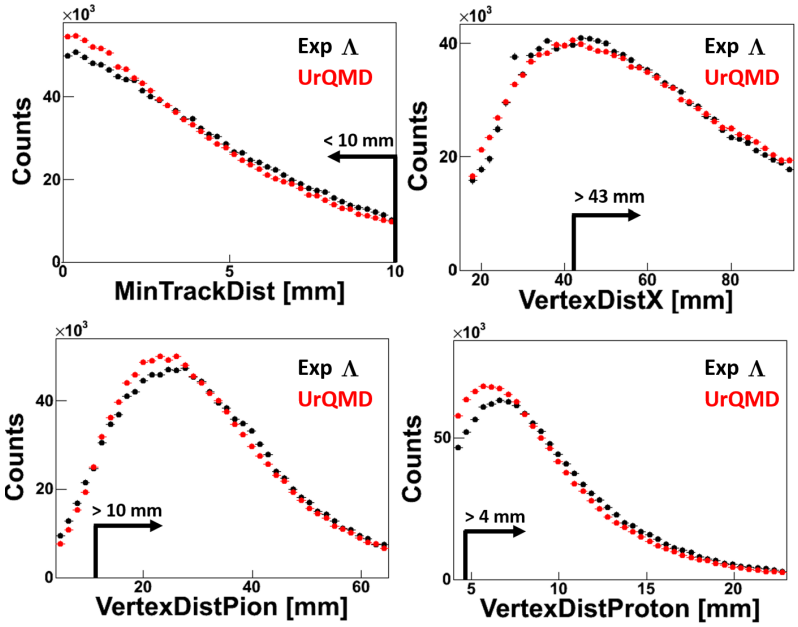

Figure 3.8: Secondary vertices compared to the UrQMD transport model. The simulation spectra describes the experimental data points.

3.6 Λ analysis

The application of all discussed vertex cuts results in an global invariant $p\pi^-$ mass spectrum illustrated in Figure 3.9. The red curve is a fit of the signal together with the background distribution and the blue curve is the raw experimental Λ yield after background subtraction. A signal peak in correspondence with the nominal Λ mass is visible. This distribution

was fitted with a sum of two Gaussians, a Landau function and a polynomial of fourth order. The Landau and the polynomial function were used to describe the background of the distribution besides and under the peak region. Because the Λ produces a narrow peak we are allowed to extrapolate into the peak region with the fit function to model the background beneath the peak and can trust the function that it reproduces the shape of the background in this region.
The sum of two Gaussians is used to reconstruct the peak originated from the Λ decay. Two Gaussian are needed to describe the full peak structure. On the one hand we use one Gauss to describe the finite width of the Λ peak and the broadening caused by finite resolution effects. On the other hand the second Gauss is needed to describe an additional broadening caused by multiple scattering of the Λ in the detector. To have only one peak width we average the two widths of the Gaussians according to formula (3.6) to the area $\sim A_i\sigma_i$ enclosed by each Gaussian, where A_i and σ_i are the amplitude and width of Gauss i:

$$\bar{\sigma} = \frac{A_1\sigma_1^2 + A_2\sigma_2^2}{A_1\sigma_1 + A_2\sigma_2}. \tag{3.6}$$

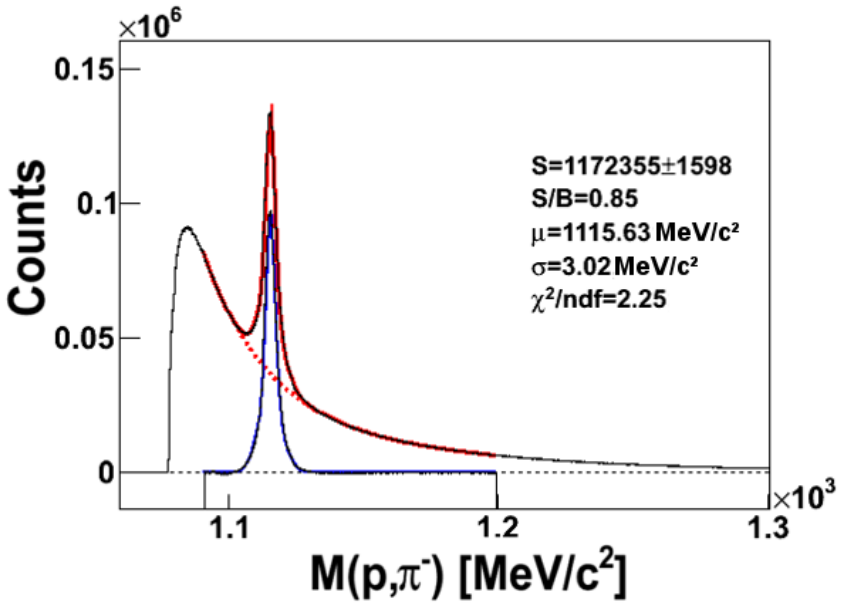

Figure 3.9: Invariant mass spectrum of $p\pi^-$ pairs measured with HADES after applying all secondary vertex cuts. The curve was fitted with a sum of a polynomial and a Landau function for the background distribution plus two Gaussians for the peak region. The blue curve illustrates the raw Λ yield after background subtraction.

We end up with a sample of about $1M$ Λs, with a signal to background ratio of $S/B = 0.85$. The large statistic allows us to perform a double differential analysis in two independent variables, which offers us the possibility to study the particles in particular kinematic configurations and is also important for efficiency corrections explained later. Because we have to deal with relativistic energies the variables should be Lorentz invariant or have simple

transformation properties. This makes it also much easier to discuss the data in different moving systems. Two variables providing such features are the transverse momentum p_t and the rapidity y of the particles. If we align the z-axis with the beam direction (as in HADES), then the variables are defined as follows (in natural units "$c = 1$"):

Rapidity of a particle:

$$y = \frac{1}{2} \ln \left(\frac{E + p_L}{E - p_L} \right) = \frac{1}{2} \ln \left(\frac{1 + \beta \cos(\Theta)}{1 - \beta \cos(\Theta)} \right), \tag{3.7}$$

where p_L denotes the momentum of the particle along the beam axis, which is in our case p_z, and E is its energy. One can think of rapidity as an abstract measurement of the longitudinal velocity $\beta \cos(\Theta)$ of the particle.
A brief remark on terminology: $y = 0$ is called mid-rapidity, and according to the previous Equation (3.7), at mid-rapidity the particles are emitted at $\Theta = 90°$ (or have no longitudinal velocity).

The transverse momentum is defined perpendicular to the beam axis, which excludes the dominating beam component p_z:

$$p_t = \sqrt{p_x^2 + p_y^2}. \tag{3.8}$$

One can think of p_t as a variable carrying the information from the interaction process. In the limit where a particle interacts only very weakly or even misses its target it flies only further in forward direction which means zero p_t. Whereas in a hard reaction process a bunch of additional particles are produced flying in different space directions and the magnitude of the reaction process is reflected in the magnitude of p_t.

The Lorentz transformations under (longitudinal) boosts read:

$$p_t \to p_t' = p_t, \tag{3.9}$$

$$y \to y' = y + y_0, \tag{3.10}$$

where y_0 is only a constant offset resulting from transforming from one frame to another.

We found proper variables for displaying the phase space. We now have to find appropriate ranges for them. This we can do by filling the phase space with the application of the optimized secondary vertex cuts and a cut on the invariant mass of the Λ in a $2\bar{\sigma}$ region. This sample contains only Λ candidates because it is still not completely background free, but it is a good starting point to find the required ranges. We have chosen for the phase space representation the nucleon-nucleon (NN) center of mass frame (CM). This choice only influences the Λ rapidity variable according to equation (3.10) by a constant shift, which is in the NN case $y_0 = 1.118$ $(y_{lab} = y_{CM} + y_0)$.

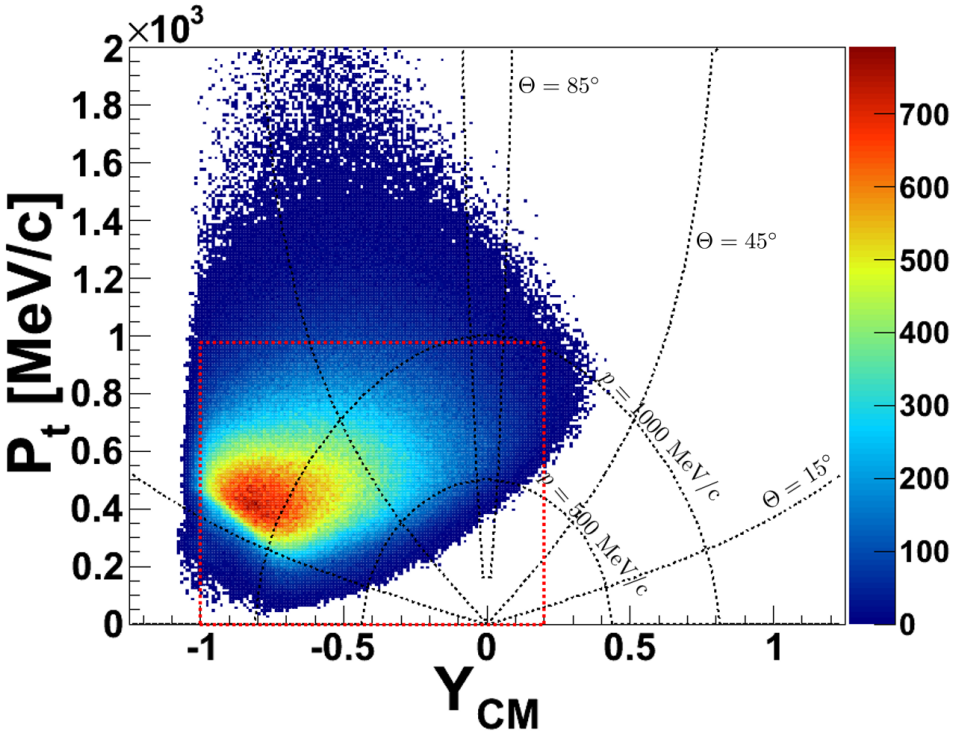

Figure 3.10: Phase space of Λ candidates. It was filled with applying secondary off-vertex cuts and a cut on the invariant mass of the Λ in a $2\bar{\sigma}$ range. The red dashed square represents the chosen analysis region.

Figure 3.10 shows the measured two-dimensional (p_t,y_{CM}) phase space for Λ candidates. Additionally, the center of mass variables for constant p_{CM} (500,1000) MeV/c and Θ_{CM} (15°,45°,85°) are plotted in black dashed lines. The phase space is mainly populated between $y_{CM} \approx -1.1 \rightarrow 0.2$ and $p_t \approx 0 \rightarrow 1000$ MeV/c. The population dies at low transverse momentum. This is an artefact of the limited acceptance of HADES, where the polar coverage starts at about $\Theta \sim 15°$ and Λs produced in very forward direction, more specifically, the decay products in forward direction (which is mainly the proton because of its mass) are not registered by the detector. For transport model studies it is important to collect as much statistic as possible at small p_t, because there the models are more sensitive to in-medium modifications of particles (slower particles stay longer in the medium).
We have chosen the following binning of the experimental data: $-1 < y_{CM} < 0.2$ in 6 Bins ($\Delta y_{CM} = 0.2$) and $0 < p_t < 975$ MeV/c in 13 Bins ($\Delta p_t = 75$ MeV/c). Another advantage of this binning is that there exists already data of analyzed K^0_S mesons in p+p as well as p+Nb reactions, performed also in the HADES collaboration, which use the same widths of the bins and thus offers us the possibility to compare them with the Λ results quite easily. With finding suitable phase space limits for the analysis, we can now extract the pure Λ signal via subtraction of the background which was still inside in Figure 3.10. For this purpose, we fill the invariant mass spectra with kinematic constraints given by the phase space binning. An example is shown in Figure 3.11 where the invariant $p\pi^-$ mass is plotted in the phase space region $-0.2 < y_{CM} < 0$, $375 < p_t < 450$ MeV/c. We repeat this for

all phase space bins which results in Figure 3.12 displaying the full phase space of raw background subtracted experimental hyperons in the HADES acceptance. This sample we have to treat further.

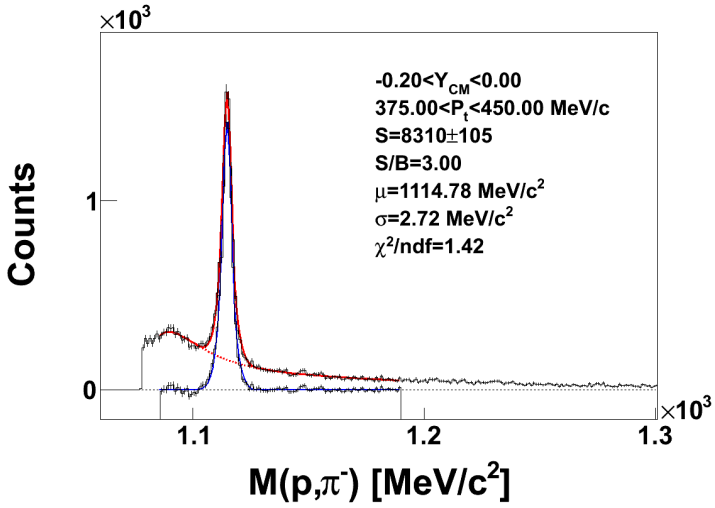

Figure 3.11: Invariant mass spectrum within a specific phase space region.

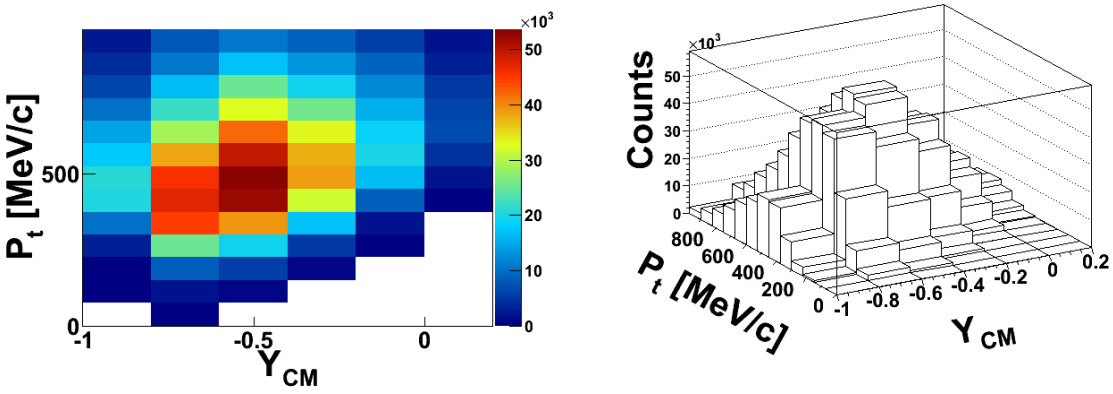

Figure 3.12: Phase space population of background free Λ hyperons in the HADES acceptance.

3.7 Efficiency correction

At this point of the analysis we have a Λ data sample of raw experimental data, which is free of combinatorial background. In a final step we want to compare the results with theoretical transport predictions. For this purpose, we correct the raw data for acceptance and efficiency effects of the detector to obtain an undistorted physical signal. Usually a finite acceptance in position space is reflected in a finite coverage in momentum space (p_t, y_{CM}), where only a fraction of the possible available phase space is measured. Events where the decay particles do not fly into the detector system are lost. The decay particles which were measured, are influenced by intrinsic detector properties like tracking efficiencies and resolution effects.

3.7.1 Strategy

Calculations of efficiency effects can be done with simulations. We have chosen the UrQMD transport model, as already mentioned. The simulation output has to be analyzed in the same way as experimental data (so called full-scale analysis). The analyzed data are then used to extract a correction matrix, which is applied to experimental data. The steps are in detail:

- **Simulation input**
  At the beginning one has to choose a model to simulate the phase space distribution. In p+A reactions one usually uses transport codes which offer the possibility to define different targets and projectiles and simulate the p+Nb reaction at 3.5 GeV in a realistic way. About every 1000 event is an event containing a Λ produced together with a bunch of other particles. We select only events with Λs and obtain a realistic phase space population in 4π without any detector effects.

- **HGEANT**
  HGEANT [HGe08] is a tool based on the Fortran package Geant [Gea95]. It contains the full HADES setup and simulates particle interactions with the detector material like secondary collisions and scatterings but also energy loss and bending in the magnetic field. As an input it uses tracks from another simulation in our case the particles produced by UrQMD.

- **SimDST**
  The output from HGEANT is in a specific form and has to be converted into a digitized format which is done in SimDST simulations. This simulated signal has exactly the same format like experimental DST files. Additionally, SimDST also takes into account detector response efficiencies like noise, finite resolution effects etc. by e.g. calculating particle momenta from the MDC hit position information with the Runge Kutta algorithm. On SimDST level it is also possible to switch on the LVL1 trigger which was used in the p+Nb run to incorporate the multiplicity threshold of three. In the end the SimDST files can be treated like real experimental data and additionally the HGEANT information is stored.

- **Analysis**
  In the last step of the full scale analysis, we analyze the simulated DSTs like experimental data. We identify the proton and negative pions with graphical cuts in the energy loss vs. momentum distribution, apply cuts on the primary and the secondary vertices with the same values taken as in the experimental case and finally construct the invariant mass to obtain the hyperon signal.

A sketch of the full scale analysis procedure is depicted in Figure 3.13.

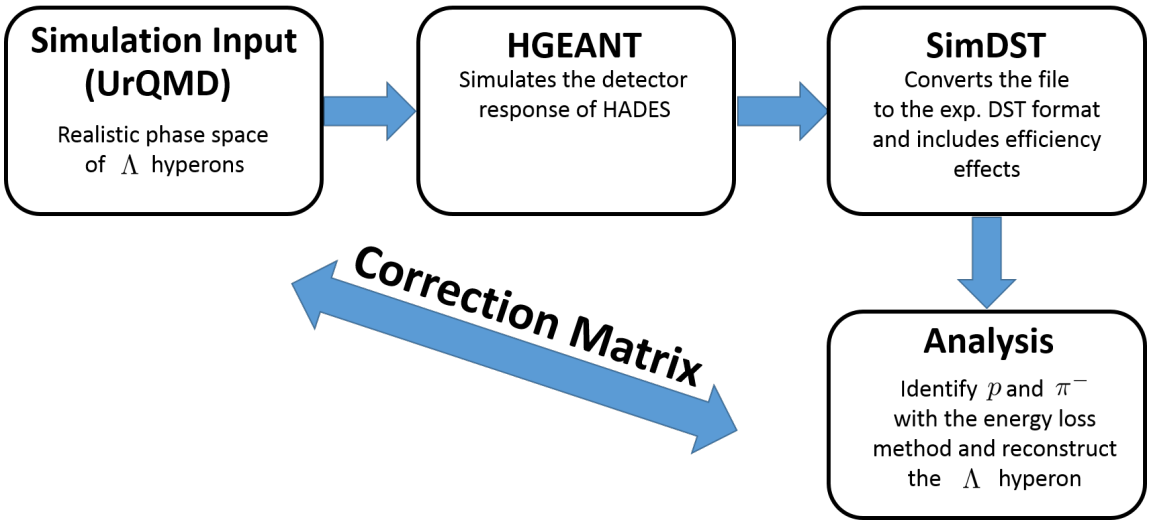

Figure 3.13: Steps of the full scale analysis. With the reconstructed Λs from simulations one is able to determine a correction matrix for acceptance and efficiency effects.

To perform an efficiency correction one needs a large statistic Λ sample. We simulated with UrQMD $\sim 1.78 \cdot 10^9$ events which results in $\sim 27 \cdot 10^6$ Λs. After the full scale analysis only about $3.67 \cdot 10^5$ Λs were left which is $\sim 1.4\%$ of the input.
Figure 3.14 displays an example of finite resolution effects of the detector. In UrQMD the Λ mass is fixed to a sharp value of $m_\Lambda = 1115.68$ MeV/c^2 (left plot). After full scale analysis the mass is visibly smeared with a finite width of $\sigma = 3.3$ MeV/c^2 (right plot).

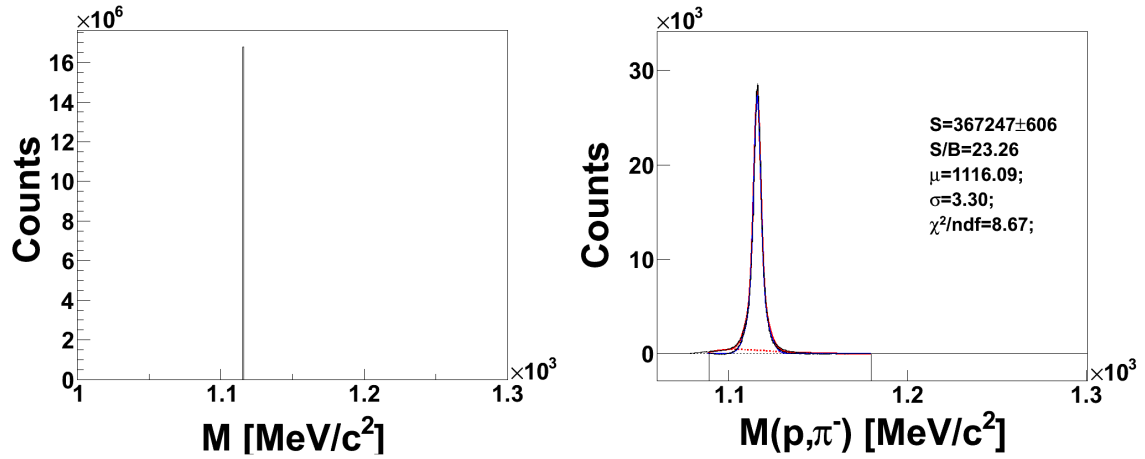

Figure 3.14: Effect of the full scale analysis. Left: Λs used as an input of the analysis chain, simulated with UrQMD.
Right: Λs after full scale analysis. The mass is clearly smeared due to finite resolution effects.

3.7.2 Determination of a correction matrix

In section 3.7.1 we explained the steps of the full scale analysis. After processing the simulated spectra through all steps it is convoluted with the efficiency of the HADES detector. But we also have the undistorted simulation input and this allows us to correct for the efficiency effect. The efficiency depends on the kinematics of the particles. For this

reason it is useful to do the correction as a function of two independent kinematic variables. We already have chosen the representation (p_t, y_{CM}) which we use now for the correction with the same binning as in the experimental case.

Let us define the Λ input from simulations for every phase space bin as

$$N^{in}(p_t,y_{CM})_{ij}. \tag{3.11}$$

The number of reconstructed particles after full scale analysis we define as

$$N^{out}(p_t,y_{CM})_{ij}, \tag{3.12}$$

where i,j number the phase space elements.

With the two definitions we can determine a matrix to correct experimental data for efficiency and acceptance. It is defined as

$$\varepsilon(p_t,y_{CM})_{ij} \equiv \left(\frac{N^{out}(p_t,y_{CM})}{N^{in}(p_t,y_{CM})}\right)_{ij}. \tag{3.13}$$

Figure 3.15 illustrates the behaviour of the simulated phase space after full scale analysis. In the left plot the simulated UrQMD input is shown. Most of the Λs in the reaction are produced at small rapidities in forward direction (small p_t). After full scale analysis the peak is shifted to larger rapidities and transverse momenta due to detector effects. At very low transverse momentum we are not even able to reconstruct Λs anymore explainable with the finite polar coverage of the HADES detector. Most Λs produced in very forward direction fly into the hole of HADES where we have no possibility to reconstruct them.
Figure 3.16 shows the correction matrix according to Equation (3.13). From this plot one can see immediately that it is important to perform the efficiency correction in two dimensions. The efficiency depends clearly on the Λ kinematics thus on the region where it flies into the detector. Λs with lower transverse momenta obtain a larger correction than Λs with larger p_t.

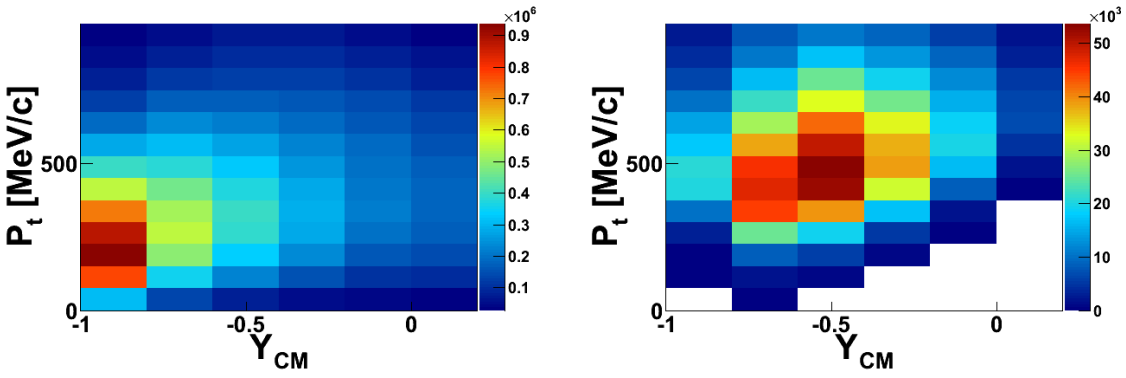

Figure 3.15: Left: UrQMD phase space used as input for full scale analysis
Right: UrQMD phase space after full scale analysis. The phase space is clearly modified due to the finite acceptance and efficiency.

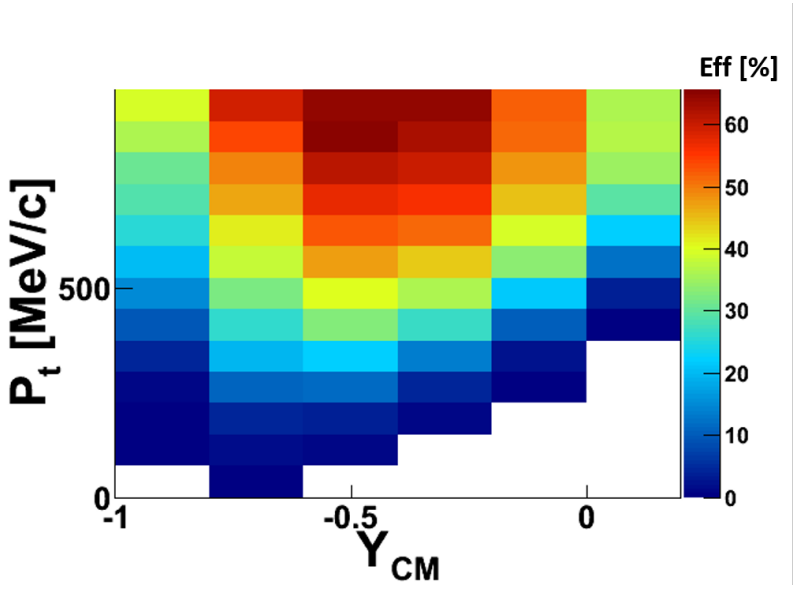

Figure 3.16: Efficiency matrix for Λ hyperons. Λs with lower transverse momenta obtain a larger correction in comparison to high p_t hyperons.

3.8 Λ hyperons corrected for acceptance and efficiency

In section 3.7.2 we obtained the necessary matrix to perform the efficiency correction. Let us define the raw experimental Λ signal as:

$$N^{raw}(p_t,y_{CM})_{ij}. \tag{3.14}$$

With help of Equation (3.13) we can calculate the undistorted experimental signal:

$$N^{corr}(p_t,y_{CM})_{ij} = \left(\frac{N^{raw}(p_t,y_{CM})}{\varepsilon(p_t,y_{CM})}\right)_{ij}. \tag{3.15}$$

The efficiency corrected phase space is illustrated in Figure 3.17. We are now allowed to compare the experimental results with theoretical calculations or transport model predictions. In principle, if one performs the correction in two dimensions with independent variables the correction matrix should be model independent. If we for example scale one specific phase space region by some factor also the output is scaled and the ratio stays the same which is the efficiency. This leads to the so called self-consistency check. We present this check in full detail in section 3.9.2.

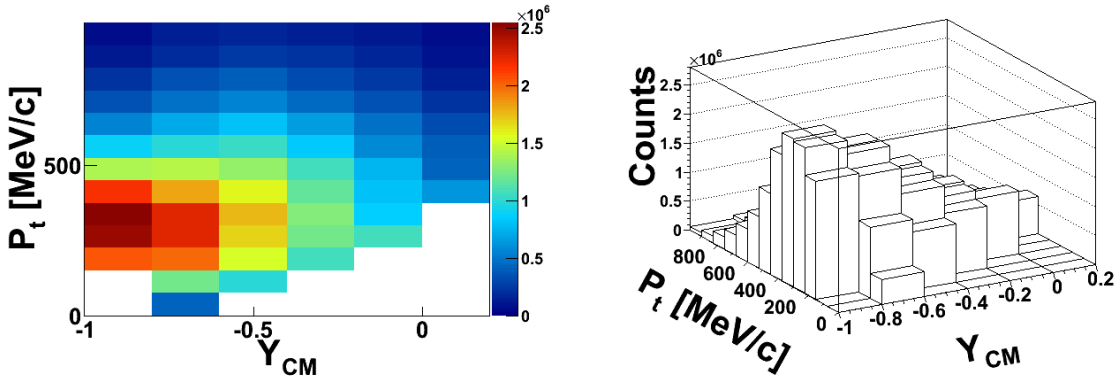

Figure 3.17: Experimental hyperons corrected for acceptance and efficiency of the HADES detector.

For the data representation we have to choose a proper normalization scheme. Especially in point of view for comparing the data with transport models it is important to have an appropriate representation to judge, if the model is able to describe the experimental data. For this reason, we have chosen an absolute normalization scheme to the total cross section of the p+Nb reaction which is $\sigma_{pNb} = 848 \pm 126$ mb [Aga13] [Tlu10]. It was determined with a comparison of π^- multiplicities measured with HADES to a systematic study of pion production in p+A reactions by the HARP-CDP collaboration.
For cross section normalization we further need the total number of events N_{tot}. To determine this number we extracted from Figure 3.2 the fraction of all minimum biased events which passes the LVL1 trigger by integrating the area beneath the $M3$ and $M0$ event curve over all impact parameters b and calculate the ratio. We obtain:

$$C(M3 \rightarrow M0) \equiv \frac{N_{LVL1}(M3)}{N_{LVL1}(M0)} = 0.58 \ . \tag{3.16}$$

We also have to take into account the number of "empty events" in the experimental data where no reaction took place, which are $\sim 17\%$ of all measured events. The total number of events used to normalize the spectra are finally:

$$N_{tot} = 0.83 \cdot \frac{N_{LVL1}(M0)}{C(M3 \rightarrow M0)} = 0.83 \cdot \frac{3.1533 \cdot 10^9}{0.58} = 4.512 \cdot 10^9 \ . \tag{3.17}$$

The experimental corrected data absolutely normalized to cross sections is shown in Figure 3.18 together with a fit of a Boltzmann-like function (see further text).

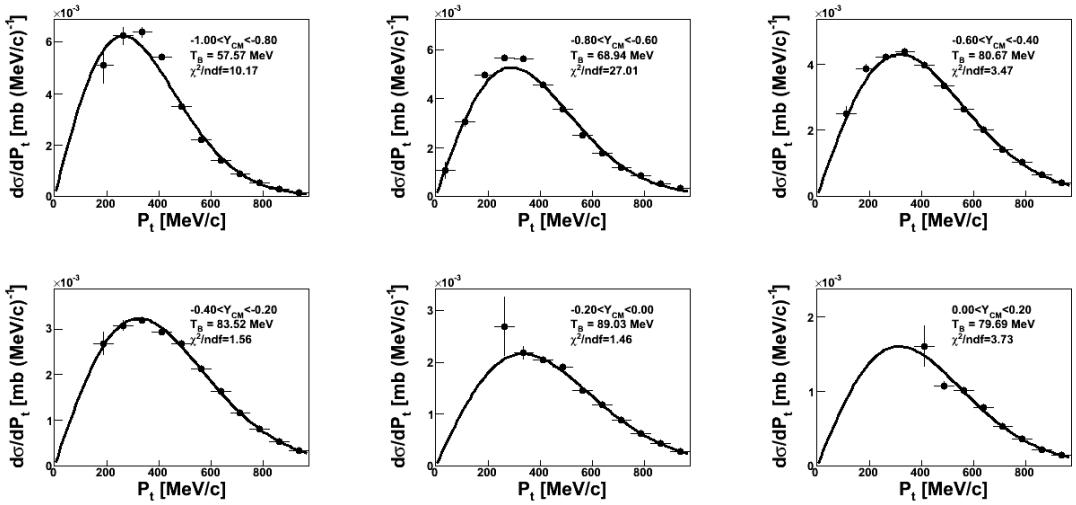

Figure 3.18: Detailed representation of the experimental data with absolute normalization to the total cross section of the p+Nb reaction. The solid black lines are fits based on a Boltzmann-like function.

Another important quantity is the rapidity-density distribution. It is obtained by integrating the two-dimensional phase space over p_t. The problem is, we do not have data points at low transverse momenta and also at very high momenta. To overcome this problem we extrapolate into this regions with a Boltzmann-like function by fitting it to the experimental data points. Whenever we have data points we sum them up and in regions where we have no yield we integrate the fit function.
A brief remark on the fit function. Lets imagine we would have a (classical) thermal source emitting particles isotropically. In the rest frame of the source the particles' momenta are distributed according to ($k_B = 1$) [Leo97]:

$$\frac{\mathrm{d}N}{d^3p} = \frac{V}{(2\pi)^3} \exp\left(-\frac{p^0}{T}\right), \tag{3.18}$$

where $p^0 = \sqrt{m^2 + \vec{p}^2}$ is the energy of the emitted particle, V the spatial volume of the thermal system (at freeze-out) and T the freeze-out temperature. To discuss the experimental results, we have to transform to the chosen variables p_t and y, with a new 4-vector:

$$p^\mu = \begin{pmatrix} m_t \cosh(y) \\ p_t \sin(\phi) \\ p_t \cos(\phi) \\ m_t \sinh(y) \end{pmatrix}, \tag{3.19}$$

where we have introduced the transverse mass $m_t = \sqrt{p_t^2 + m^2}$. After calculating the Jacobian determinant for the new variables we obtain for the particle distribution:

$$\frac{\mathrm{d}N}{\mathrm{d}y\mathrm{d}p_t^2\mathrm{d}\phi} = \frac{V}{2(2\pi)^3} m_t \cosh(y) \exp\left(-\frac{m_t \cosh(y)}{T}\right). \tag{3.20}$$

We have an azimuthal symmetric system which allows us to integrate over ϕ. After introducing an inverse slope parameter $T_B(y) = T/\cosh(y)$ and rewriting Equation (3.20) to the representation of p_t, we obtain the desired fit function:

$$\frac{\mathrm{d}N}{\mathrm{d}y\mathrm{d}p_t} = A(y)p_t\sqrt{p_t^2 + m^2}\exp\left(-\frac{\sqrt{p_t^2 + m_t^2}}{T_B(y)}\right), \tag{3.21}$$

where we have introduced a rapidity dependent fit parameter $A(y)$ in addition to the inverse slope parameter $T_B(y)$ which are both free parameters and fixed by fitting them to the experimental points. The fit function (3.21) is evaluated separately in every rapidity bin shown in Figure 3.18.
The concept of a thermal source is a helpful tool which leads to a smooth function following the trend of the data and it is only used for the purpose to extrapolate in regions where we have no data points.
We also see immediately from the fit function the advantage of choosing proper coordinates for the phase space representation. Imagine we would have chosen (p,Θ) as coordinates. Formula (3.18) would be still valid, but to calculate the fit function we would have to boost into a moving system with an unknown velocity $\vec{\beta}_S$ of the source which one has to determine first with some uncertainty before fitting the other two parameters.
After performing the integrations over p_t ($\int dp_t\ dN/dp_t dy_{CM}$) in the two-dimensional phase space we obtain the one-dimensional rapidity-density distribution shown in Figure 3.19, which we also normalized to the total cross section.

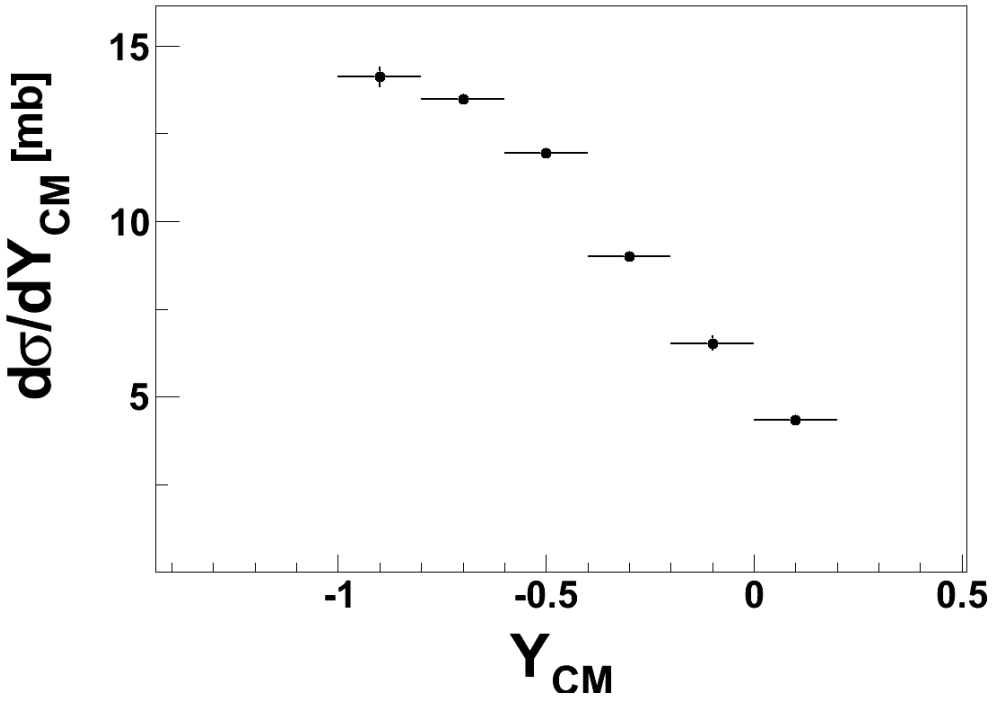

Figure 3.19: Rapidity-density distribution normalized to the cross section of the p+Nb reaction.

The rapidity-density distribution increases going from large rapidities to target rapidities ($y_{CM} = -1.18$). In a symmetric collision system (like p+p or A+A) the rapidity distribution would be symmetric around its maximum located at the center of mass rapidity zero ($y_{CM} = 0$) in the nucleon-nucleon system [Aga11b] [Bar01]. The asymmetric behaviour in our case is based on the fact that we have a highly asymmetric collision system p+Nb. Most produced Λs are rescattered and stopped by the target nucleus which explains the larger yield in direction of target rapidity and the asymmetric shape of the distribution. We checked with simulations (GiBUU) that if we switch off any YN-interaction we get a nearly symmetric distribution because also the system becomes then nearly symmetric (p+p or p+n). In the region of target rapidity we do not have data points anymore, which is directly related to the upper polar acceptance of $\Theta = 85°$. This region we can only study with help of simulations, which we will do in the next chapter.

In a last step we determine a distribution of the inverse slope parameter $T_B(y_{CM})$ obtained from fitting the data as displayed in Figure 3.21 with the Boltzmann-like function. According to the thermal model the transformation of Equation (3.18) to Equation (3.21) leads to a relation of the freeze-out temperature T_{eff} to the inverse slope parameter:

$$T_B(y_{CM}) = \frac{T_{eff}}{\cosh(y_{CM} - Y_0)}, \tag{3.22}$$

where Y_0 was introduced as an additional fit parameter. This curve is symmetric around Y_0. For a better illustration we plotted an example of Equation (3.22) in Figure 3.20 ($T_{eff} = 80$ MeV, $Y_0 = 3$).

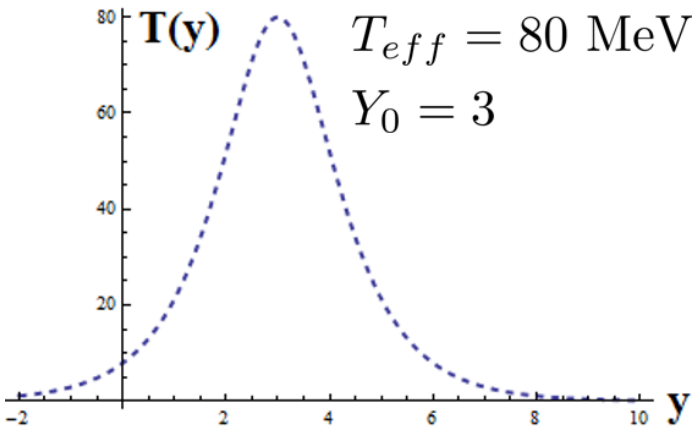

Figure 3.20: Inverse slope parameter $T_B(y)$ as a function of rapidity according to Equation (3.22).

By fitting the inverse slope spectra, we obtain the red dashed line in Figure 3.21. Y_0 is fixed to the rapidity where we have the maximum inverse slope value of the p+Nb system $T_B(Y_0 = -0.1) = 89.03$ MeV. In this plot the effective temperature T_{eff} was treated as a free fit parameter, which was set to the value $T_{eff} = 84.14$ MeV by the fit procedure. The function follows the trend of the data points, but we cannot claim that it is reproducing the data. Unfortunately, at higher rapidities we do not have data points which would reveal information on the symmetry of the experimental curve around $Y_0 = -0.1$ to confirm the

validity of Equation (3.22). The last bin in the region $0 < y_{CM} < 0.2$ seems to contradict a mirror symmetry around $Y_0 = -0.1$.
If we set the effective temperature in the fit function of Equation (3.22) to the maximal inverse slope value $T_{eff} = T_B(Y_0 = -0.1) = 89.03$ MeV (assuming we reach the maximal freeze-out temperature in this rapidity region, which is a reasonable assumption because at larger rapidities the inverse slope parameter decreases) we see that the data points lie below the curve and do not fulfill the assumption of a thermal model.
In simulations we checked (see next chapter) that the first chance production of Λs influences mainly the region of large rapidities ($y_{CM} > -0.4$). The number of YN collisions in this range are smaller which means that the produced hyperons are nearly undistorted after production. At least in this range the assumption of a isotropic thermal source becomes doubtful because of a lack of any thermalisation processes. In general one has to check carefully the applicability of statistical thermodynamics in A+A and in particular in p+A reactions. We only deal with a small amount of matter in tiny volumes, on time scales of the order of 10^{-23} s over space dimensions of a few fermi.

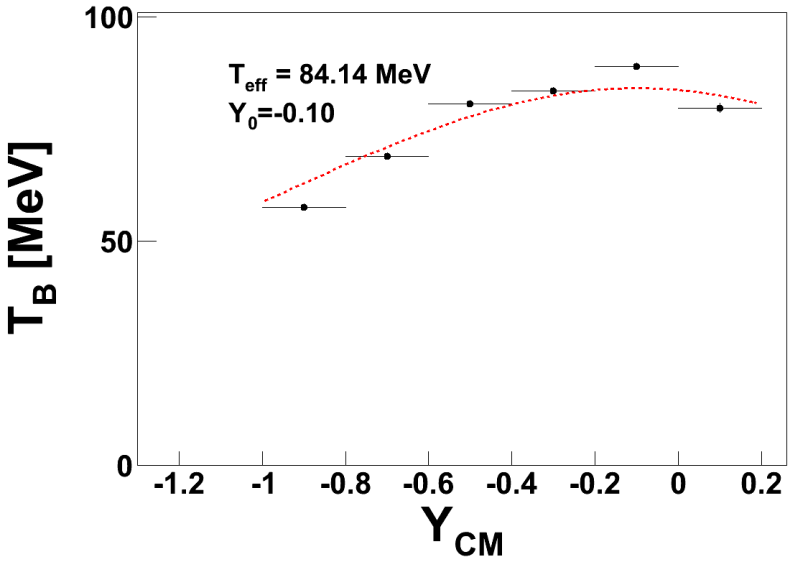

Figure 3.21: Plot of inverse slope parameters extracted from the Boltzmann fit function (dots). The red dashed line illustrates the fit function of the thermal model with the freeze-out temperature treated as a free fit parameter.

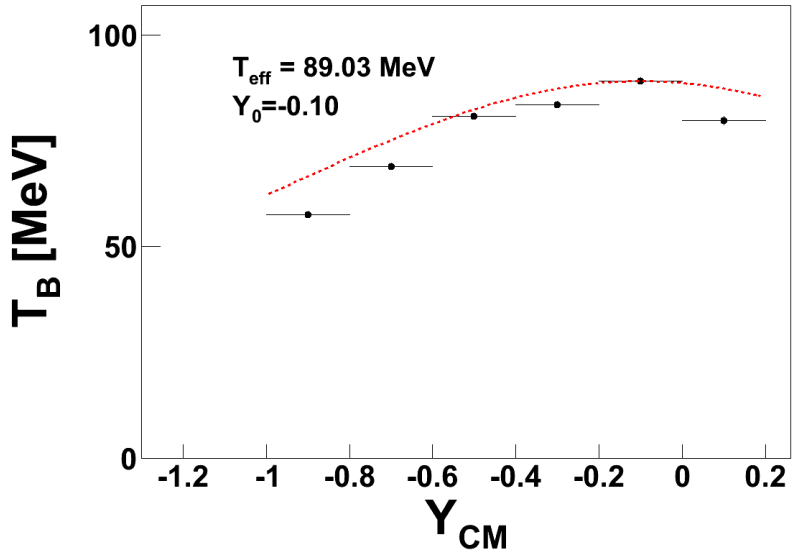

Figure 3.22: The parameters of the thermal fit function were set to the maximal reachable freeze-out temperature T_{eff} = 89.03 MeV. The experimental data points lie below the dashed curve of the thermal model.

3.9 Efficiency correction - Consistency checks

The efficiency correction is an important step in the analysis because afterwards we compare the experimental data to theoretical models. To check the reliability of the efficiency correction we performed two different checks. In the first check we used only one model (UrQMD) and this test deals with the chosen phase space parametrization and bin sizes of the correction matrix. In a second check we perform corrections using the information from an additional model (GiBUU). This test address the problem of the model independence in the efficiency correction process. If the analysis passes both checks we can trust the correction and can be sure that the corrected data are based on solid ground.

3.9.1 Check within one model

The principle of doing a consistency check within one model (UrQMD) is the following. We are free to choose two different independent variables to perform the correction. Instead of (p_t,y_{CM}) we could have also chosen (p,Θ) and determine the efficiency matrix in this representation. Eventually, we use this matrix to correct the experimental data which is given the (p_t,y_{CM})-space. This tags mainly the problem of binning effects as we will see in a moment.
At first we have to select again a proper range for the variables in the (p,Θ)-space. Figure 3.23 shows the population of Λ candidates together with the selected analysis region (red dashed lines).

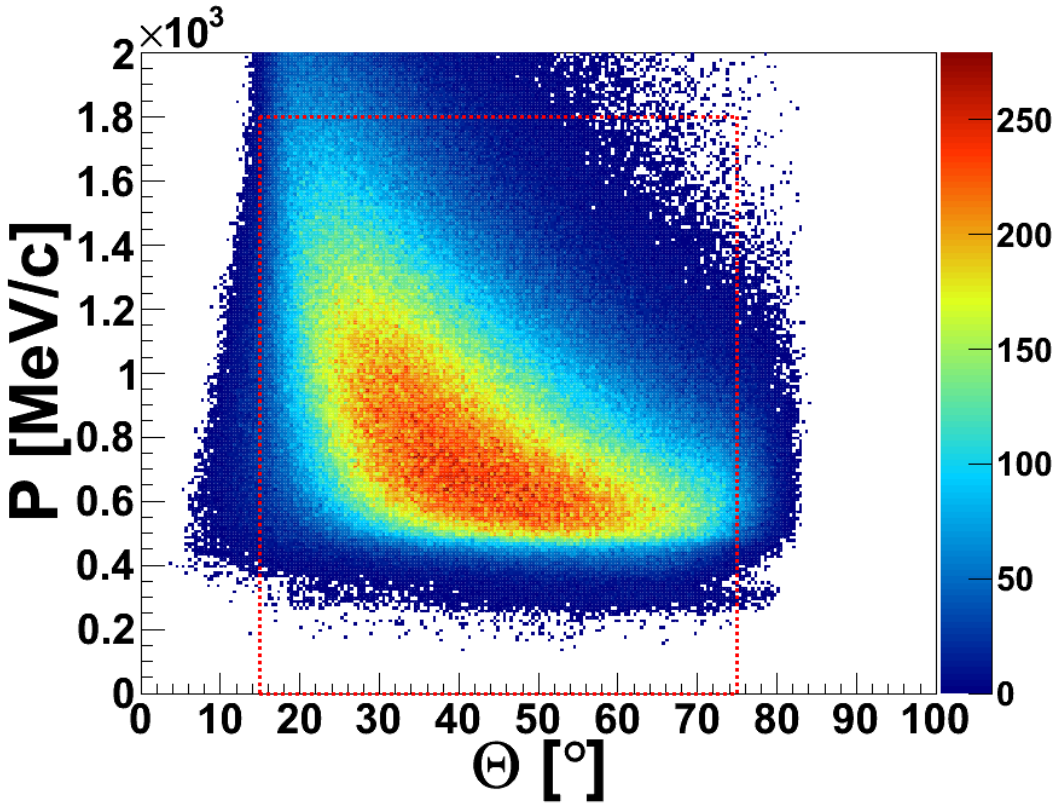

Figure 3.23: Phase space population of Λ candidates in the (p,Θ) representation. The red dashed line illustrates the chosen analysis range.

We have chosen for the analysis in (p,Θ)-space the following binning:

$0 < p < 1800$ MeV/c in 12 Bins
$15° < \Theta < 75°$ in 6 Bins

The steps are the same as in section 3.7.2. We fit the experimental data and subtract the background to determine the raw experimental phase space for Λs. We calculate the efficiency matrix in the (p,Θ)-space by performing a full-scale analysis with the simulation data and divide the outcome by the simulation input. The efficiency matrix for (p,Θ)-coordinates has the shape as illustrated in Figure 3.24.

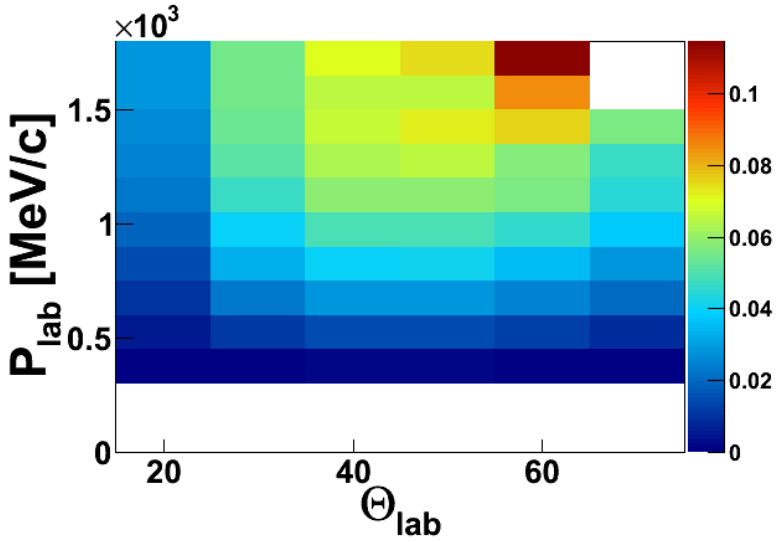

Figure 3.24: Efficiency matrix in the (p,Θ)-space obtained with the UrQMD model.

We want to use this matrix to correct the data in the (p_t,y_{CM})-space. This procedure is not straightforward, because both representations are connected with non-linear transformations as illustrated in Figure 3.25 where we plotted the two-dimensional phase space (p_t,y). The black dashed lines are lines of constant linear momentum p and polar angle Θ. One can immediately see that the Cartesian matrix elements of Figure 3.24 become curved in the (p_t,y)-space (for better illustration we plotted black dots in every matrix element which should represent a constant efficiency in the (p,Θ)-space). Loosely spoken we cannot simply reshuffle all matrix elements of Figure 3.24 to obtain the correction matrix in the (p_t,y_{CM}) representation.

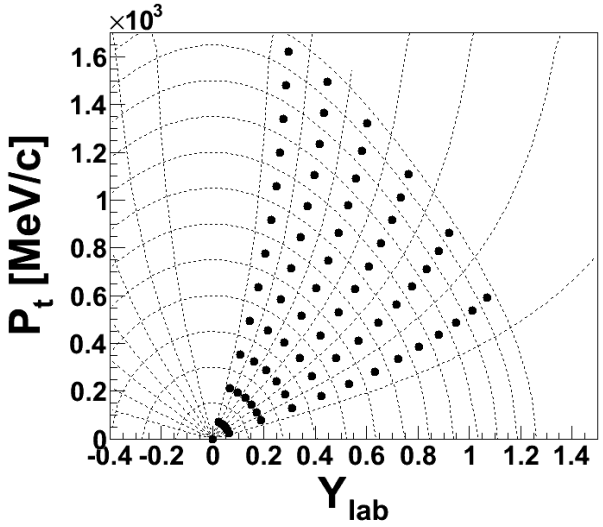

Figure 3.25: Transformation (p,Θ) $\rightarrow$ (p_t,y). The dashed lines illustrate the lines of constant momenta p and angle Θ.

To solve the problem, we define the mean value of every matrix element of the correction matrix in Figure 3.24 as a grid point. Subsequently, all points define a grid which is used for an interpolation technique. After interpolation we are able to calculate the efficiency at any point in the selected (p,Θ) range. Interpolation is possible because the efficiency varies only slowly as a function of the particles momentum p and angle Θ. We end up with a smooth efficiency surface, displayed in Figure 3.26.

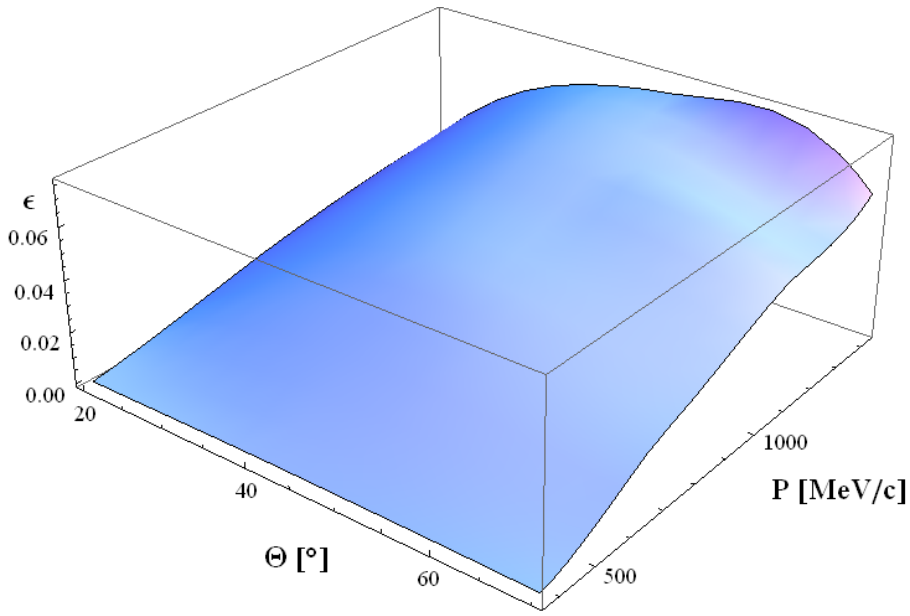

Figure 3.26: Smooth efficiency matrix surface in (p,Θ)-space determined with an interpolation technique.

Now we are able to calculate the efficiency at every coordinate (p,Θ). Both phase space representations are connected with the Equations:

$$p = \frac{\sqrt{p_t^2 + m^2 \tanh^2(y)}}{1 - \tanh^2(y)}, \tag{3.23}$$

$$\Theta = \arcsin\left(\frac{p_t}{p}\right). \tag{3.24}$$

We plug in the (p_t,y_{CM}) values in the Equations (3.23) and (3.24) to calculate the corresponding (p,Θ) coordinates. Knowing them, we determine the efficiency $\varepsilon(p,\Theta)$ for these points from the two dimensional interpolation function of Figure 3.26.
Let us compare the two different methods of efficiency corrections, which are shown in Figure 3.27. Red data points represent the direct way via the efficiency matrix evaluated in section 3.7.2, whereas black points were corrected in the indirect way as just presented.

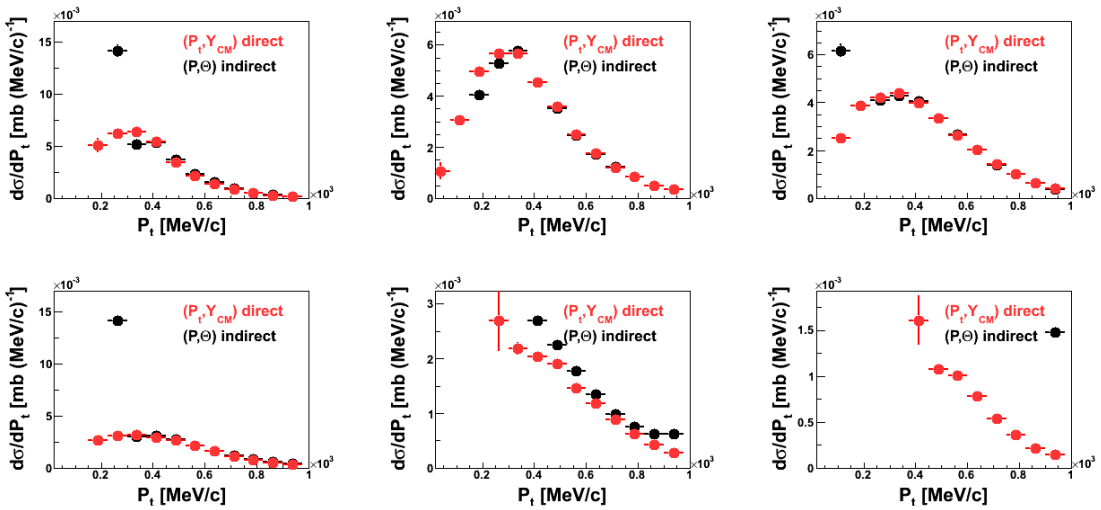

Figure 3.27: Comparison of both efficiency correction methods. Red dots were obtained by using the direct method, whereas black dots represent the method over a different phase space representation.

In some regions we had no interpolation value and an extrapolation method was used. This clearly fails which explains that some data points at low transverse momentum are completely off. In the last rapidity bin interpolation was not possible, which is the reason why there are no (indirect) points plotted. In all other bins the method worked quite well. We learn from this consistency check two things:

- The analysis of the data does not depend on the chosen phase space parametrization as long as we use two independent variables. In this particular case (p_t,y_{CM}) and (p,Θ) give equivalent results.
- When we subdivide the phase space into bins with constant size we correct them with the efficiency value for these bins. In the indirect correction procedure the bin size varied and the difference to the fixed bin size is not large. As long as we choose the dimension of the correction matrix large enough, which means a sufficient number of correction matrix elements, the correction works well.

3.9.2 Check using an additional model

Comparing efficiency corrections within one model showed that the data does not depend on the chosen phase space parametrization and also not on the binning, if the dimension of the correction matrix is large enough. To check especially the model independence of the efficiency correction process, one has to use the information from an additional model. Imagine we have two completely different simulation models 1 and 2. With both models we perform a full scale analysis to have their data in the HADES acceptance folded with the detector efficiency. The strategy is now to calculate with one of the two models, lets say model 2, a correction matrix. This matrix is used to correct data in the HADES acceptance of model 1. The corrected yield of model 1 can now be compared to the original input of model 1 and both curves should match each other, if the correction process is model independent. The whole process is often called self-consistency check. Figure 3.28 illustrates

the strategy of the self-consistency check in a flow diagram, where we assumed that the correction matrix is calculated with model 2 (also the other way round is possible).

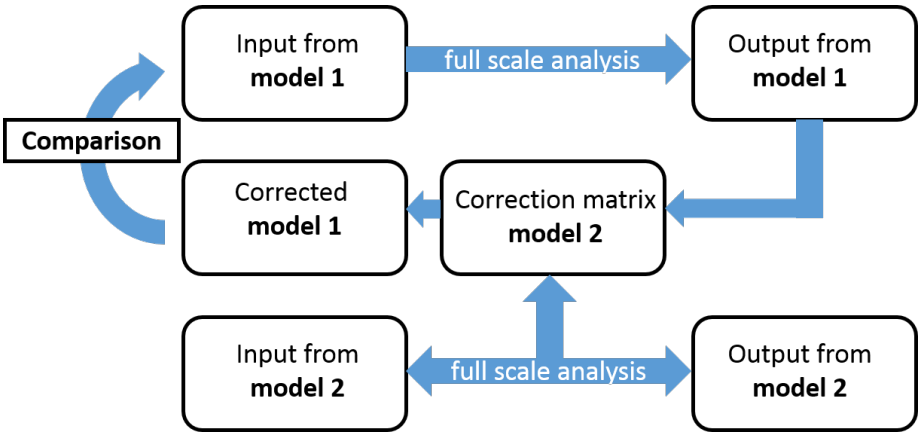

Figure 3.28: The strategy of the self consistency check in a flow diagram. With both models a full scale analysis is performed. Model 2 is used to calculate a correction matrix with the aim to correct the output of model 1 data in the HADES acceptance. The corrected output of model 1 is finally compared to the original input of model 1.

For the self-consistency check we use the data from UrQMD as model 1. As a second model we have chosen GiBUU, with which we simulated an input sample containing about 6M Λs (could be raised in future and is only limited due to computation time) and calculated a correction matrix. In a first step we compare the correction matrices of both models for the two dimensional phase space (p_t,y_{CM}) in Figure 3.29.

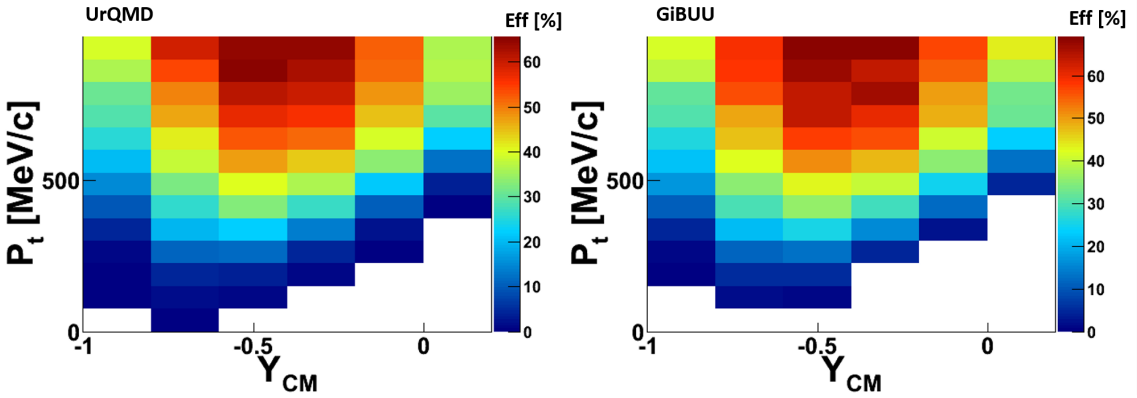

Figure 3.29: Correction matrices from UrQMD (left) and GiBUU (right). The shape looks quite similar. Because of the lower simulated statistic of GiBUU we have no correction factor in some bins of very low transverse momenta.

The shape of the two matrices look quite similar. Both models predict the same kinematic dependency of the efficiency, for example a larger correction for lower transverse momenta. To examine the model independence and validate the efficiency correction, we have to compare the corrected UrQMD data with its input, which is shown in Figure 3.30 for the whole two-dimensional phase space.

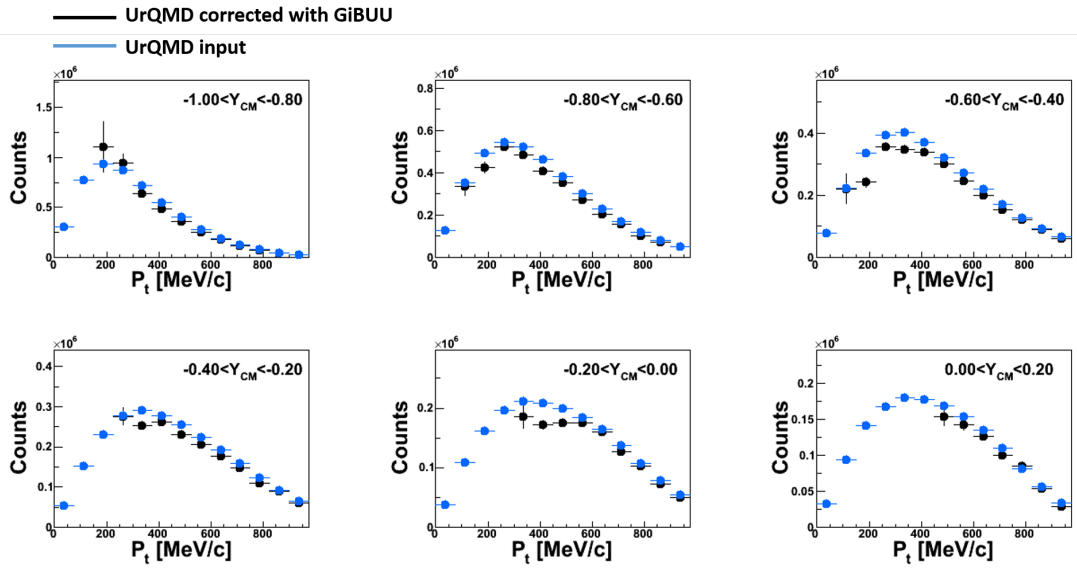

Figure 3.30: Comparison of the original UrQMD input (blue) with corrected UrQMD data (black) using the correction matrix calculated with GiBUU.

We see that the yield and trend of the black points, which are UrQMD data corrected with GiBUU and the blue points from the original UrQMD input is nearly the same. This was already indicated by the similar shape of the correction matrices in Figure 3.29. At lower transverse momenta some bins exhibit larger deviations, which is based on the fact that we have a lower statistic in the simulation input of the GiBUU model. Nevertheless, the curves show a nice agreement, which is a clear signal that the performed efficiency correction process is model independent for the inclusive Λ analysis, as long as we use two independent kinematic variables for the phase space representation.

4 Comparison with transport models

Experimentally accessible spectra of final-state particles contain information integrated over the whole time of the collision process. To learn something about the reaction dynamics transport models are commonly used. They are based on microscopic models having the fundamental degrees of freedom for the actual energy scale and their interactions inside and solve the corresponding equations of motion numerically.
Their main application is in the field of heavy ion physics. For instance, the prediction of QCD of a phase transition to a quark gluon plasma indicated by J/Ψ modification can be studied within transport models. But there is no restriction to study also other hadronic reactions.
They offer a full time dependency and are based on experimental ingredients like cross sections or decay widths. Their goal is to simulate the reactions with a realistic input to learn something about particle production, scattering or absorption to finally reproduce the experimental spectra. A big advantage of transport models is that they are valid at every time step of a physical reaction from the initial defined state (e.g. the start of an A+A collision) to the final particle outcome because they are not based on a particular physical assumption. Statistical models, or models based on thermodynamical principles in general, have to assume some specific configuration (equilibrium state) and this is achieved only at a certain time during the process or even never, what is illustrated in Figure 4.1.

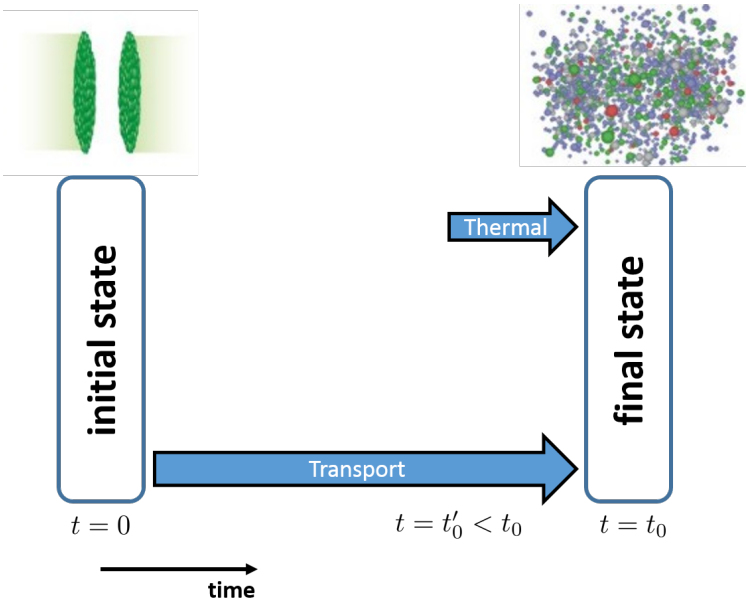

Figure 4.1: The advantage of transport in comparison to thermal models. One is able to simulate the whole reaction process because the model does not depend on a specific physical configuration. For example thermal models have to assume an equilibrium state, which is reached at a later time in the whole reaction process (or even never).

We use for the study of the p+Nb reaction two different transport models, UrQMD (v3.3p1) [Bas98] [Ble99] and GiBUU(v1.5.0) [Bus12]. Both models and their underlying structure are presented to get a feeling how they work, what they have in common and where they differ. But in general they solve with the Monte Carlo technique a large set of coupled partial integro-differential equations for the one particle phase space densities $f_i(x,p)$, where i denotes the particle species. In the non-relativistic limit they assume the Boltzmann form [Ble99]:

$$\frac{\mathrm{d}f_i}{\mathrm{d}t} \equiv \frac{\partial p}{\partial t}\frac{\partial f_i(x,p)}{\partial p} + \frac{\partial x}{\partial t}\frac{\partial f_i(x,p)}{\partial x} + \frac{\partial f_i(x,t)}{\partial t} = \mathrm{St}f_i(x,p), \tag{4.1}$$

where x and p are the position and momentum of the particle and $\mathrm{St}f_i(x,p)$ is the collision term.

4.1 Ultrarelativistic Quantum Molecular Dynamics - UrQMD

UrQMD is based on the Quantum Molecular Dynamics (QMD) approach [Bas98]:

4.1.1 Equations of motion

In general, in a QMD model each nucleon is represented by a coherent state which is parametrized using Gaussian wave packets:

$$\phi_i(\mathbf{x};\mathbf{q}_i,\mathbf{p}_i;t) = \left(\frac{2}{L\pi}\right)^{3/4} \exp\left(-\frac{2}{L}(\mathbf{x}-\mathbf{q}_i(t))^2 + i\mathbf{p}_i(t)\mathbf{x}\right), \tag{4.2}$$

and the total n-body wavefunction is assumed to be a direct product of coherent states (no anti-symmetrization for fermions):

$$\mathbf{\Phi} = \prod_i \phi_i(\mathbf{x};\mathbf{q}_i,\mathbf{p}_i;t). \tag{4.3}$$

The dynamics is governed by the equations of motion for each nucleon i. The starting point is the action S, which is defined as the integral over the Lagrangian functional depending on the wave function $\mathbf{\Phi}$:

$$S = \int_{t1}^{t2} dt\mathcal{L}[\mathbf{\Phi},\mathbf{\Phi}^*]. \tag{4.4}$$

If one assumes a Hamiltonian of the form "kinetic plus potential energy" ($H = \sum_i T_i + \sum_{i,j} V_{ij}$) and requires that the action S, defined in Equation (4.4), stays stationary under the variation of the coherent states, one obtains the equations of motion for each particle:

$$\dot{\mathbf{q}}_i = \frac{\partial \langle H \rangle}{\partial \dot{\mathbf{p}}_i}, \tag{4.5}$$

$$\dot{\mathbf{p}}_i = -\frac{\partial \langle H \rangle}{\partial \dot{\mathbf{q}}_i}. \tag{4.6}$$

These equations have the same structure as derived from Hamilton's principle in classical mechanics and are solved numerically for various kinds of interactions.

4.1.2 Collisions

The particle trajectories are determined by their equations of motion including also interactions V_{ij}. One can explicitly include collisions between particles with the condition that two particles collide, if their minimum distance d in the CM frame fulfills:

$$d \leq d_0 = \sqrt{\frac{\sigma_{tot}}{\pi}}, \tag{4.7}$$

where σ_{tot} is the total cross section for the collision. The cross sections are *a priori* not known and if available fitted to experimental data. For resonance excitation an effective parametrization based on phase space considerations is exploited. Also time reversibility or isospin symmetry is employed. Total elastic and inelastic cross sections for proton-proton and proton-neutron collisions are well known and incorporated in the model. Because the functional shape for these cross sections show a non-trivial behavior at small $\sqrt{s}$, UrQMD uses a look-up table.
The mostly unknown cross sections like hyperon-baryon resonance scattering are parametrized with help of the additive quark model, where the cross section depends only on the quark-content of the colliding hadrons:

$$\sigma_{tot} = 40 \cdot \left(\frac{2}{3}\right)^{n_M} \cdot (1 - 0.4x_1^s) \cdot (1 - 0.4x_2^s), \tag{4.8}$$

$$\sigma_{el} = 0.039 \cdot \sigma_{tot}^{2/3}, \tag{4.9}$$

where $n_M = m_1 + m_2$ and $m_i = 1(0)$ for particle i being a meson (a baryon) [Ble99]. The $x_i = s_i/(3 - m_i)$ (s_i is the number of strange quarks in hadron i) contain the fraction of strange quarks to non-strange quarks in the hadron i. It contains no explicit energy- or momentum dependence, which is valid at high energies, but maybe breaks down for cross sections close to threshold.

4.1.3 Ur + QMD

Up to now this was a description of the QMD model. The new feature of UrQMD is that it uses a covariant formalism i.e. the model is also valid at larger relativistic energies.
Its main improvements to the standard QMD model are [Bas98]:

- covariant dynamics
- an improved and extended collision term containing heavy baryon-resonances, strange particles and string excitation for high energy hadron-hadron interactions

String fragmentation becomes important at high energies, where we have a large momentum transfer Q^2. The running coupling of QCD becomes small and the excitation of color strings and their fragmentation to hadrons plays a role, whereas at lower energies the relevant degrees of freedom are hadrons and their resonances. In total, UrQMD contains 55 different baryon species like delta-resonances, hyperon-resonances etc. with masses up to 2.25 GeV/c^2 and 32 different meson species. For fulfilling baryon symmetry also their antiparticles are

included. All these particles can be produced and propagated explicitly in the model. Below $\sqrt{s} = 5$ GeV for baryon-baryon collisions and $\sqrt{s} = 3$ GeV for meson-baryon and meson-meson collisions the hadronic reactions are modeled with interactions of hadrons and their resonances [Ble99].

4.1.4 Initialization of the nucleus

We are interested in the specific case of pA simulations. UrQMD defines the nucleus according to the Fermi-gas ansatz.
Each nucleon is described by a Gaussian wave function defined in Equation (4.2) and the initialization must meet the requirement:

- $\sum_i \mathbf{v}_i = 0$, the nucleus is at rest,
- $\sum_i \mathbf{q}_i = 0$, the nucleus is centered at $\mathbf{0}$ in configuration space.

Additionally, the binding energy E/A matches the value predicted by the Weizsäcker mass formula and the density at the nucleus center is adjusted to nuclear saturation density.
The nucleons at the beginning of the simulation are distributed within a sphere with radius:

$$R(A) = r_0 \left(\frac{1}{2} \left[A + (A^{1/3} - 1)^3 \right] \right)^{1/3}, \tag{4.10}$$

where the parameter r_0 depends on the saturation density ρ_0 and is defined as:

$$r_0 = \left(\frac{3}{4\pi\rho_0} \right)^{1/3}. \tag{4.11}$$

The nucleon's momentum is chosen randomly between 0 and the Fermi momentum $p_F^{max} = (3\pi^2\rho)^{1/3}$. A potential problem is that the small number of nucleons distributed in the sphere introduce fluctuations in the mean density of the nucleus. To avoid this, after a nucleon placement the phase-space density is checked and if it is too high (e.g. the phase-space is already occupied by another nucleon) the location of the nucleon is rejected and a new location is chosen randomly.

4.2 Giessen Boltzmann-Uehling-Uhlenbeck model - GiBUU

The GiBUU model solves a generalized BUU equation numerically. Its main ingredients are:

4.2.1 Test particles

We have seen that in a QMD model the nucleons are parametrized by Gaussian wave packets ϕ_i. The GiBUU model uses a different approach to solve the BUU equation. The dynamical quantity studied is the phase space density $F(x,p)$. This phase space density represents the particles e.g. nucleons and are represented by so called test particles, which are commonly chosen as δ-functions in momentum- and coordinate space. The test particle

ansatz reads:

$$F(x,p) = \lim_{n(t)\to\infty} \frac{(2\pi)^4}{N} \sum_{j=1}^{n(t)} \delta(\mathbf{r} - \mathbf{r}_j)\delta(\mathbf{p} - \mathbf{p}_j)\delta(p^0 - p_j^0(t)), \tag{4.12}$$

where $n(t)$ denotes the number of test particles. As initial condition ($t = 0$) the number of test particles is set to $n(0) = N \cdot A$, where A is the number of real (physical) particles and N the number of ensembles (test particles per physical particles, usually set to $N \sim 1000$). To obtain the equations of motion for the test particles one starts from the generalized BUU equation and neglects the off-shell and collision term [Wei08] (usually called Vlasov equation):

$$[p_0 - H,F] = 0, \tag{4.13}$$

which describes a system with stable particles propagating through a mean-field. The used Poisson brackets are defined as follows (using Einstein convention of an implicit sum):

$$[A,B] \equiv \frac{\partial A}{\partial p_\mu}\frac{\partial B}{\partial x^\mu} - \frac{\partial A}{\partial x_\mu}\frac{\partial B}{\partial p^\mu}. \tag{4.14}$$

From Equation (4.13) one can calculate a time derivative for the one particle phase space density F:

$$\dot{F} = \frac{1}{1 - \frac{\partial H}{\partial p_0}} \left[\frac{\partial H}{\partial \mathbf{x}}\frac{\partial F}{\partial \mathbf{p}} - \frac{\partial H}{\partial \mathbf{p}}\frac{\partial F}{\partial \mathbf{x}} - \frac{\partial H}{\partial t}\frac{\partial F}{\partial p_0}\right]. \tag{4.15}$$

Using the test particle ansatz from Equation (4.12) in combination with the Vlasov Equation (4.13) one obtains another expression for the time derivative of F:

$$\dot{F} = -\frac{\partial F}{\partial \mathbf{p}}\dot{\mathbf{p}}_i - \frac{\partial F}{\partial \mathbf{r}}\dot{\mathbf{r}}_i - \frac{\partial F}{\partial p^0}\dot{p}_i^0. \tag{4.16}$$

A comparison of Equation (4.15) and (4.16) gives the equations of motion for the test particles:

$$\frac{\mathrm{d}\mathbf{r}_j}{\mathrm{d}t} = \Big(1 - \frac{\partial H}{\partial p_0}\Big)^{-1}\frac{\partial H}{\partial \mathbf{p}}, \tag{4.17}$$

$$\frac{\mathrm{d}\mathbf{p}_j}{\mathrm{d}t} = -\Big(1 - \frac{\partial H}{\partial p_0}\Big)^{-1}\frac{\partial H}{\partial \mathbf{r}}, \tag{4.18}$$

$$\frac{\mathrm{d}p_j^0}{\mathrm{d}t} = \Big(1 - \frac{\partial H}{\partial p_0}\Big)^{-1}\frac{\partial H}{\partial t}. \tag{4.19}$$

The term $\partial H/\partial p_0$ appears for "off-shell potentials" and vanishes in most cases [Wei08]. If it is zero we obtain the ordinary Hamiltonian equations of motion as already seen in the UrQMD section.

4.2.2 Particle production and collisions

In the GiBUU model particle production in the strangeness sector for elementary collisions is based on cross sections determined from the Tsushima resonance model [Tsu99]. The

Tsushima model uses an effective Lagrangian with the mesons π,η,ρ, K, where the first three are treated as exchange bosons, and baryons + baryon-resonances N, Y, $N(1650)$, $N(1710)$, $N(1720)$, $\Delta(1920)$ for which it was experimentally observed that they decay to kaons and hyperons. In the model it is assumed that every hyperon-kaon pair stems from a resonance decay $R \to Y + K$. The illustration is given in Figure 4.2 showing the Feynman diagrams used for calculations where $B = N$,Δ. The energy dependence of the calculated

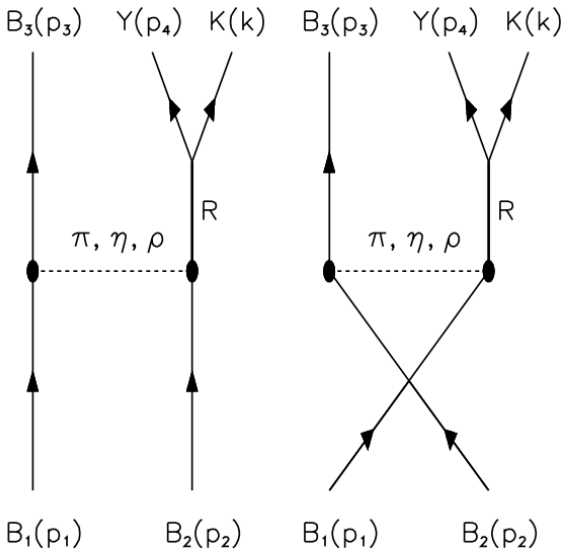

Figure 4.2: Feynman diagrams used in the Tsushima model for cross section calculations [Tsu99].

cross sections is parametrized in the form:

$$\sigma(B_1B_2 \to B_3YK) = a\Big(\frac{s}{s_0} - 1\Big)^b \Big(\frac{s}{s_0}\Big)^c, \tag{4.20}$$

where s is the invariant collision energy for the reaction, s_0 for the threshold, and a,b,c are parameters fixed in a way that the calculated cross section is reproduced.
GiBUU incorporates the parametrized cross section from Equation (4.20). The intermediate resonances are not explicitly produced in the transport simulations for strangeness production. Their influence is only indirectly included via the cross section calculations.
For higher energies GiBUU uses the string model PYTHIA [Sjö07] to describe two-body collisions. The default transition takes place at $\sqrt{s} = 2.6$ GeV for baryon-baryon collisions and $\sqrt{s} = 2.2$ GeV for meson-baryon collisions (valid for the version 1.5.0).
Elastic and inelastic YN-scattering is included with analytic functions obtained from fits to experimental data.

4.2.3 Nuclear ground state

The coordinates of neutrons and protons are chosen according to empirical density profiles of Woods-Saxon or harmonic oscillator type. The initial particle momenta are distributed to a local Thomas-Fermi approximation,

$$f_{n,p}(\mathbf{r},\mathbf{p}) = \Theta\Big[p_{F,n,p}(\mathbf{r}) - |\mathbf{p}|\Big], \tag{4.21}$$

where p_F ist the Fermi momentum

$$p_{F,n,p}(\mathbf{r}) = (3\pi^2\rho(\mathbf{r}))^{1/3}. \tag{4.22}$$

Proton and neutron matter densities serve as an input. The phase space densities are normalized to them:

$$\rho_{n,p}(\mathbf{r}) = g\int f_{n,p}(\mathbf{r},\mathbf{p})\frac{d^3p}{(2\pi)^3}. \tag{4.23}$$

At this point the single-particle phase-space densities f are fully determined. One defines the momentum density as:

$$n_{n,p}(\mathbf{p}) = g\int f_{n,p}(\mathbf{r},\mathbf{p})\frac{d^3r}{(2\pi)^3}, \tag{4.24}$$

which is normalized to $\int d^3p\; n_p(\mathbf{p}) = Z$, $\int d^3p\; n_n(\mathbf{p}) = A - Z$. By using $\sim 10^3$ test particles smooth distributions in momentum and coordinate space are achieved and one can start with the propagation according to the Hamiltonian equations of motion for the test particles.

4.2.4 Real and perturbative mode

Because transport simulations are very time consuming, especially due to the collision of test particles, the model includes two different simulation realizations. The idea behind this is that for low energetic reactions only a small part of the nucleons takes part in the process, whereas the rest stays close to the ground-state. One can then numerically assume that there is a group of active test particles involved in the process whereas the rest only acts as a background for the propagation of the active test particles. This leads to a definition of two types of test particles: active one which are called *perturbative* t and the remnant nucleus test particles which are called *real* r.
The restrictions for perturbative test particles are:

- perturbative test particles are not allowed to collide with each other: $t + t \nrightarrow$,
- the product of a perturbative and real test particle collision is again a perturbative test particle: $t + r \rightarrow t$,
- perturbative test particles are neglected in the calculation of the actual density.

These constraints for perturbative test particles allows a clear separation between real and perturbative test particles. Because of this concept one can split a perturbative particle into n realizations during a run which enlarges the statistic significantly. However, one should keep in mind that this is only an approximation to save computation time. To be really sure that the applicability of *perturbative* simulations is fulfilled one has to investigate the difference of the *real* and *perturbative* simulation mode in detail for a specific reaction.

4.3 Short summary

Category	**UrQMD** (3.3p1) [Bas98] [Ble99]	**GiBUU** (1.5.0) [Bus12]
Degrees of freedom	Smooth Gaussian wave packages. One packet represents one particle.	Test particles parametrized as sharp δ functions. One physical particle is represented by $\sim 10^3$ test particles.
Production of Strangeness	Includes 55 and 32 meson species which all can be explicitly produced and propagated. Strange particles are either produced directly or can stem from decaying resonances.	Based on Tsushima model [Tsu99]. Only the final state particles are produced, but not the intermediate resonances.
Scattering	Uses an effective cross section parametrization fitted to experimental data. Additive quark model for hyperon-baryon resonance scattering.	YN-scattering is parametrized with analytic functions fitted to available experimental scattering data.

4.4 UrQMD predictions

4.4.1 Normalization

In the last chapter we presented the normalization of the experimental data to the total cross section of the p+Nb reaction, which was $\sigma_{pNb} = 848 \pm 126$ mb [Aga13] [Tlu10]. UrQMD calculates the total cross section according to a simple geometrical model treating the nucleus as a disc $\sigma_{p+A} \sim \pi b^2$, where b is the impact parameter. This parametrization is much too simple, because it depends on the chosen impact parameter b and does not incorporate any effects from the nucleus surface. It is also not used in the model internally to calculate any quantities. To make a connection to the model and average over the nucleus surface we performed a simulation for the p+Nb reaction with the largest possible impact parameter, which is $b = 8.15$ mb. The geometrical cross section for this reaction is calculated by UrQMD to $\sigma_{geo} = 2087.82$ mb, which overestimates the experimental value already by $\sim 2.5\ \sigma_{exp}$. We simulated 1M events with UrQMD. In only 52.67% of the events a collision took place (the rest are empty events where the proton misses the nucleus). We use this information together with the geometrical calculated cross section to define a surface averaged cross section, which has a connection to the Niobium nucleus used in the simulation:

$$\sigma_{\mathrm{pNb,UrQMD}} = \sigma_{\mathrm{geo}} \times \frac{\text{Number of events where a reaction took place}}{\text{Number of total events}}. \tag{4.25}$$

This results in a surface averaged cross section of $\sigma_{\mathrm{pNb,UrQMD}} = 1099.82$ mb. We also checked other impact parameters, but the influence on the result is very small. We take this value of the surface averaged cross section to absolutely normalize the UrQMD simulation spectra.

4.4.2 UrQMD comparison and Σ^0 contribution

We compare now the efficiency corrected two-dimensional (p_t,y_{CM}) spectra with UrQMD predictions. The UrQMD data is normalized according to Equation 4.25. The solid lines from the fit with a Boltzmann-like function from the last chapter are plotted to illustrate the trend of the experimental data at low transverse momenta, where we have no experimental data points. Figure 4.3 shows the UrQMD simulation of "direct" Λs for the two dimensional phase space (p_t,y_{CM}) in comparison to the efficiency corrected experimental Λ yield. "Direct" in this context means that the simulation sample does not include Λs from decays of long lived resonances which are dominantly Σ^0s. Black are (also for the further plots) the experimental points whereas the cyan points are predictions of the simulation model. The "direct" yield does not reproduce the experimental data perfectly. Especially at lower transverse momenta $p_t \lesssim 450$ MeV/c simulation and experimental data are no longer in agreement (in the last rapidity bin also for larger momenta).

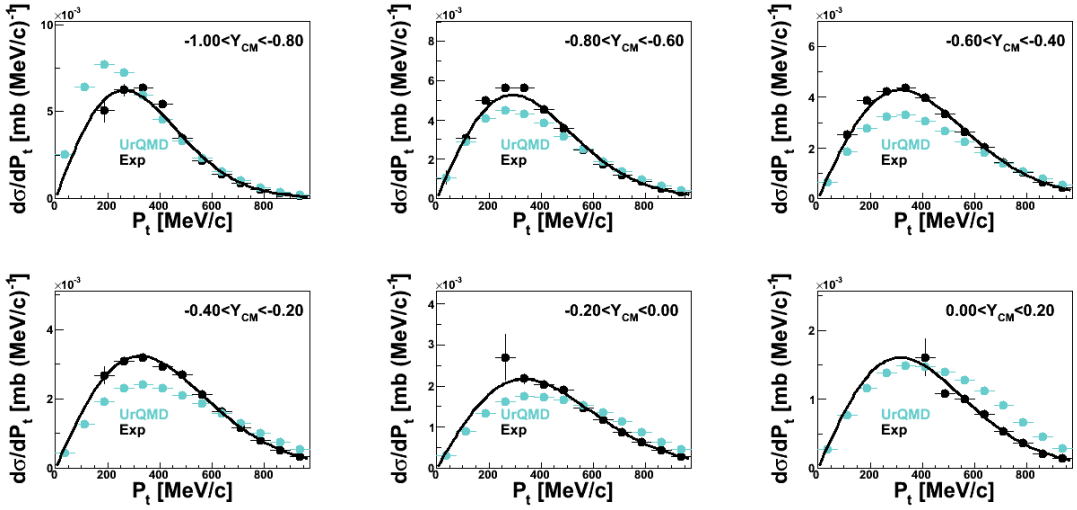

Figure 4.3: Comparison of the efficiency corrected experimental data (black) with UrQMD simulations (cyan) of "direct" Λs.

Additionally, the plotted simulation Λ yield is at this stage incomplete because we also have to take into account the contribution of "indirect" Λs stemming from Σ^0 decays. At the end of the transport calculation most of the Σ^0s did not decay. Experimentally it is observed that the Σ^0 decays almost exclusively into a $\Lambda\gamma$ pair. The HADES setup does not contain a calorimeter which would be necessary to distinguish Λs from Σ^0s by the detection of an additional γ. Therefore, in this inclusive analysis Λs and Σ^0s are indistinguishable and the spectra are a sum of "direct" and "indirect" Λs, which we have to consider also in the simulation. We estimated the contributions of "direct" Λs and "indirect" Λs from Σ^0s with UrQMD simulations. The model predicts a ratio of $\Lambda/(\Lambda + \Sigma^0) = 0.70$. We see that about 30% of the Λs are coming from long lived resonances.
There are two ways to add the Σ^0 contribution to the "direct" simulation output. The first one is to treat Σ^0s simply as Λs ($\Sigma^0 \equiv \Lambda$) and copy their kinematics. This is to a certain extent reasonable because in the Σ^0 decay to a $\Lambda\gamma$ ($E_\gamma \sim 80$ MeV) pair the photon changes only slightly the kinematics of the Λ at SIS energies and the Σ^0 4-vector stays nearly the same $p^\mu_{\Sigma^0} \approx p^\mu_\Lambda$ ($(m_{\Sigma^0} - m_\Lambda)/m_\Lambda \approx 6.9\%$). The second way is to simulate the decay of

the Σ^0 and incorporate the correct Λ kinematics. We investigated the second way in more details by taking a Σ^0 sample, simulating the decay with help of the GEANT package and comparing it to the case where the Σ^0s are treated as Λs. The result for the whole phase space is displayed in Figure 4.4.

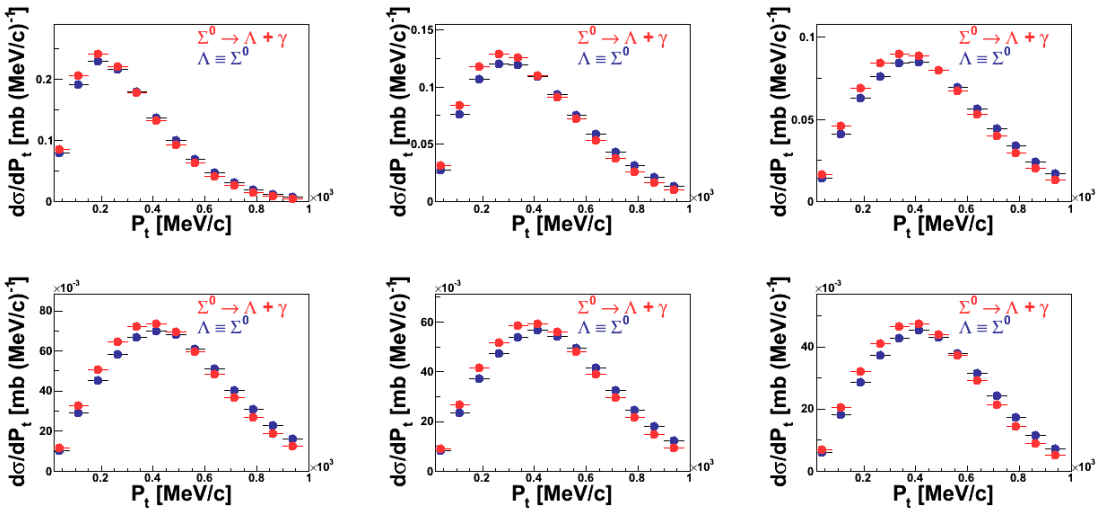

Figure 4.4: Comparison of two methods of adding the Σ^0 contribution to the "direct" Λ yield. The red points illustrate Λs from a Σ^0 decay whereby the blue points are Σ^0s treated as Λs. The decay shifts the yield to lower transverse momenta.

The red points illustrate Λs from the decay $\Sigma^0 \rightarrow \Lambda\gamma$ whereas the blue points represent Σ^0s which were treated as Λs. As we expected, the difference is small due to the fact that the photon changes only slightly the original Σ^0 kinematics. The transverse momenta of the Λs stemming from decays are shifted to lower values because of transfered momentum to the photon.
We want to include the correct Λ kinematics after the transport simulation. For this purpose we define a decay matrix in the following way (with the information obtained with the GEANT simulation presented in Figure 4.4):

$$\lambda(p_t,y_{CM})_{ij} \equiv \Big(\frac{\Sigma^0 \text{ treated as a } \Lambda}{\Lambda \text{ from } \Sigma^0 \text{ decay}}\Big)_{ij}, \tag{4.26}$$

for every phase space bin labeled by i,j. The matrix is illustrated in Figure 4.5. It was determined with a Σ^0 sample from UrQMD and should in general be universal, which means model independent. This will be tested in future with a different model.

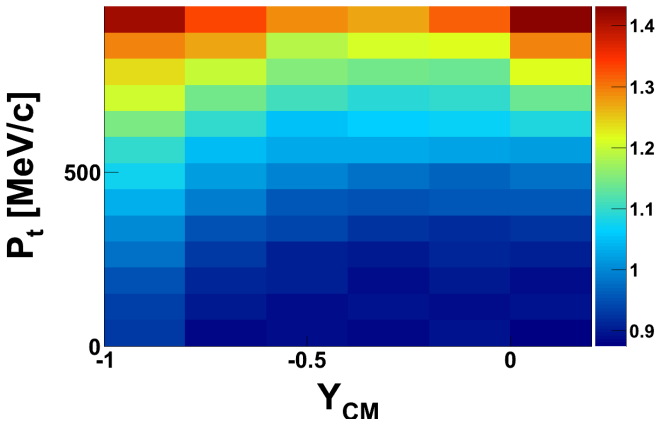

Figure 4.5: Decay Matrix to correct the Σ^0 simulation and to obtain the correct Λ kinematics.

The correction works as follows: after transport calculations we identify the "direct" Λs as usual and additionally the Σ^0s. These Σ^0s are corrected with the matrix λ_{ij} of Equation (4.26) in the same way we correct raw experimental data for efficiency to transform the Σ^0s into Λs, which have then the correct kinematics:

$$\Lambda(\text{from } \Sigma^0)(p_t,y_{CM})_{ij} = \left(\frac{\Sigma^0(p_t,y_{CM})}{\lambda(p_t,y_{CM})}\right)_{ij}, \tag{4.27}$$

where i,j label the phase space region as usual. In a last step we add this "indirect" contribution to the "direct" Λ production output to obtain the whole Λ yield. The total ("direct"+"indirect") Λ UrQMD signal is shown in the the plot in Figure 4.6 again for the whole (p_t,y_{CM}) phase space.

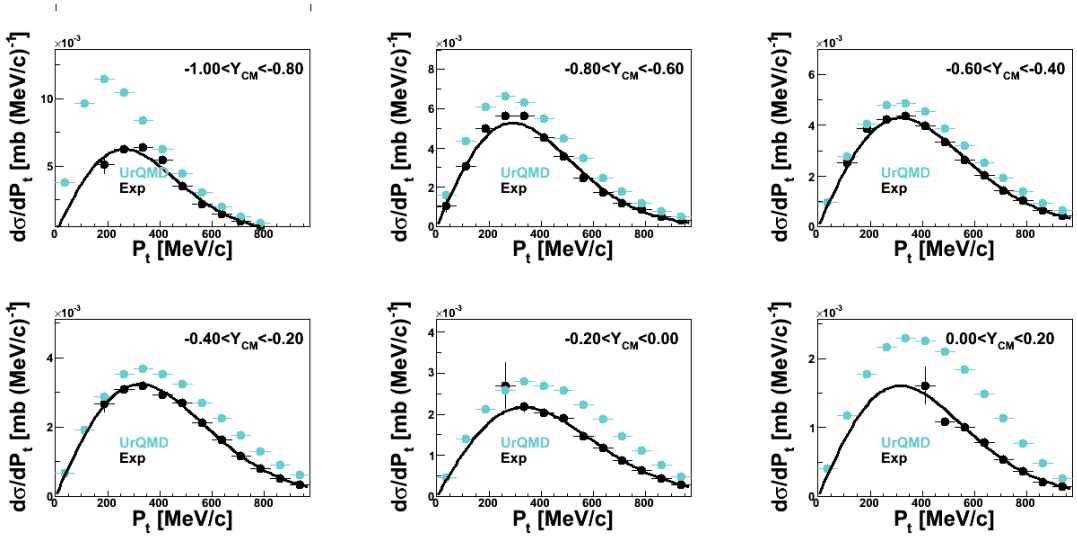

Figure 4.6: UrQMD predictions (cyan) compared to the experimental data (black). The UrQMD output contains the full yield of Λs directly produced and from Σ^0 decays with the correct kinematics.

The UrQMD model is able to describe the trend of the experimental data. However, the yield is too high in the whole rapidity range especially at the edges of the experimental phase space ($-1 < y_{CM} < -0.8$ and $0 < y_{CM} < 0.2$). Nevertheless, UrQMD gives promising results for a model "out of the box" without any tuning.
Before checking sophisticated mechanisms of the model like scattering or potential effects one should check first the production of particles. We simulated for this reason p+p reactions with a proton energy of 3.5 GeV and extracted the cross sections for several strangeness channels containing Λ or Σ^0 hyperons. The results are listed in Table 4.1. For p+p reactions at 3.5 GeV UrQMD uses a total cross section of 41.83 mb. The experimental values in Table 4.1 labeled with a * were measured by an exclusive analysis [Ber13] in the HADES collaboration and the other values were obtained by a fit to the world data with a phase space parametrization already presented in Equation (4.20).

Channel	UrQMD, σ [μb]	Exp, σ [μb]
$\Lambda p K^+$	176.7	45.0
$\Sigma^0 p K^+$	41.9	15.5
$\Lambda p \pi^+ K^0$	29.0	44.46*
$\Lambda n \pi^+ K^+$	5.02	24.3
$\Lambda p \pi^0 K^+$	7.63	18.9
$\Sigma^0 p \pi^+ K^0$	3.00	12.25*

Table 4.1: Production cross sections for p+p reactions at a proton kinetic energy of 3.5 GeV. Channels labeled with a * were measured by the HADES collaboration [Ber13]. All other experimental values were extracted by a phase space fit to existing world data.

In general, the cross sections do not match very well. It seems that especially the two simplest 3-body channels $\Lambda/\Sigma^0 p K^+$ are overestimated by the model. This could be a reasonable explanation why the UrQMD yield was too large in Figure 4.6. Fortunately, the HADES experiment measured also p+p reactions and a Λ analysis is ongoing [Lal13]. With experimental data we can better constrain the production channels and test UrQMD production mechanisms for Λs. Also the role of producing intermediate resonances $pp \rightarrow N^* p$ and the corresponding angular distributions has to be investigated. There exits also the possibility that these resonances interfere with each other what could change the spectra dramatically in comparison to an incoherent adding of different resonance contributions. Such effects can be studied with a partial wave analysis (PWA) [Ani12]. All this different possibilities have to be checked in detail for pp reactions and later also the influence on the p+Nb spectra has to be tested.

4.5 GiBUU predictions

4.5.1 Normalization

From the GiBUU output one can extract the cross section which the model uses for the simulation of the reaction. The normalization procedure depends on the chosen simulation mode:

- Perturbative simulations:

$$d\sigma = \frac{\text{Weight factor}}{\text{Number of xml files}}, \tag{4.28}$$

  where the *Weight factor* is calculated by the model and xml files are the output files of GiBUU if running in perturbative mode.

- Real simulations:

$$d\sigma = 2\pi b db \cdot c^{-1}, \tag{4.29}$$

  where the factor c is the product of *the number of used ensembles*, *number of runs at same energy* and *number of independent simulations* where the first two numbers are fixed at the beginning of the transport simulation.

4.5.2 Comparison of GiBUU predictions with experimental data

As stated in section 4.2.4, GiBUU offers the possibility for two different simulation concepts to save computation time. To check the qualitative behaviour of the model we used *perturbative* simulations. This gave us the opportunity to study changes in the model quite fast. For the first studies we also shifted the transition to the PYTHIA model to larger energies to be sure that all particles are produced according to the Tsushima resonance model. The authors of [Tsu99] claim that the Tsushima resonance model is applicable to invariant collision energies of $\sqrt{s} = 3.6$ GeV, which is larger than the experimental NN collision energy $\sqrt{s_{NN}} = 3.18$ GeV. From GiBUU developers itself it is proposed that HADES data should be described within one model consistently and the transition region was pushed by them to larger values [Wei12a] (in the new GiBUU version 1.6.0 which was not available as this work was written, the transition energy for baryon-baryon collisions will be set to $\sqrt{s_{NN}} = 3.4$ GeV [Wei13]). In all following spectras we added the Σ^0 contribution with the correct kinematics.
Figure 4.7 compares GiBUU predictions with the experimental data, again for the whole two-dimensional Λ phase space.

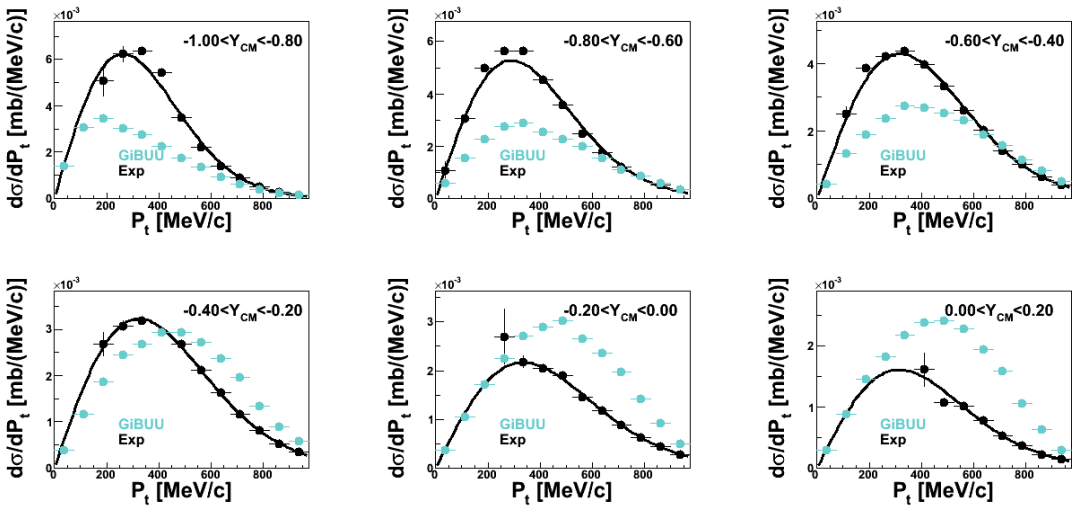

Figure 4.7: GiBUU predictions (cyan) based on resonance model calculations in perturbative mode compared to the experimental data (black).

We immediately see that the model underestimates the experimental data at lower rapidities, whereas at larger rapidities it overestimates it. We want to understand in detail which regions of the spectra are influenced by which mechanism. In an ongoing K^0 analysis in the HADES collaboration it was shown that it is necessary to scale production cross sections down, otherwise the yield of K^0s is too high [Lap13]. The scaling of neutral kaon cross sections will also influence the Λ production because of strangeness conservation. Table 4.2 shows the original production cross sections in the Tsushima resonance model and the applied scaling factor in brackets (obtained in the K^0 analysis).

Channel, $p+p \rightarrow$	Tsushima model, σ [μb]	Exp, σ [μb]
$\Lambda p K^+$	35.7	45.0
$\Sigma^0 p K^+$	17.5	15.5
$\Lambda p \pi^+ K^0$	75.9 (0.42)	44.46*
$\Lambda n \pi^+ K^+$	25.3	24.3
$\Lambda p \pi^0 K^+$	25.3	18.9
$\Sigma^0 p \pi^+ K^0$	24.6 (0.72)	12.25*

Table 4.2: Production cross sections for p+p reactions at a proton kinetic energy of 3.5 GeV implemented in the GiBUU model. The channels labeled by a star are measurements performed in the HADES collaboration [Ber13]. All other values were obtained by a fit using a phase space parametrization to world data. The numbers in brackets are the applied scaling factors to reproduce K^0 data [Lap13].

If we apply the scaling of the production cross section used in the K^0 analysis we obtain the results displayed in Figure 4.8.

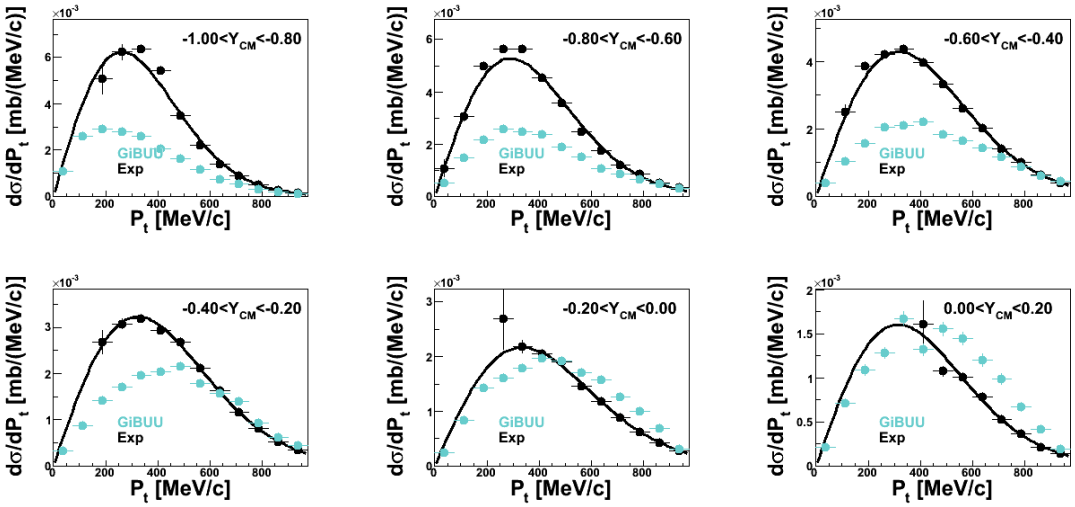

Figure 4.8: GiBUU model with scaled production cross sections compared to experimental data.

In comparison to Figure 4.7 we see that the production of Λs influences mainly large rapidities ($y_{CM} > -0.4$). In this region the Λ is produced and leaves the nucleus relatively undistorted. After the production scaling the yield is more in agreement with the experimental data.
This finding also implies that a different mechanism is present at lower rapidities. What we would expect is that lower rapidities are mainly populated by slower which means scattered or stopped Λs. To test this hypothesis and additionally find out if the scattering is primary elastic or inelastic we switched off the elastic Λ-nucleon scattering channel. The result is shown in Figure 4.9.

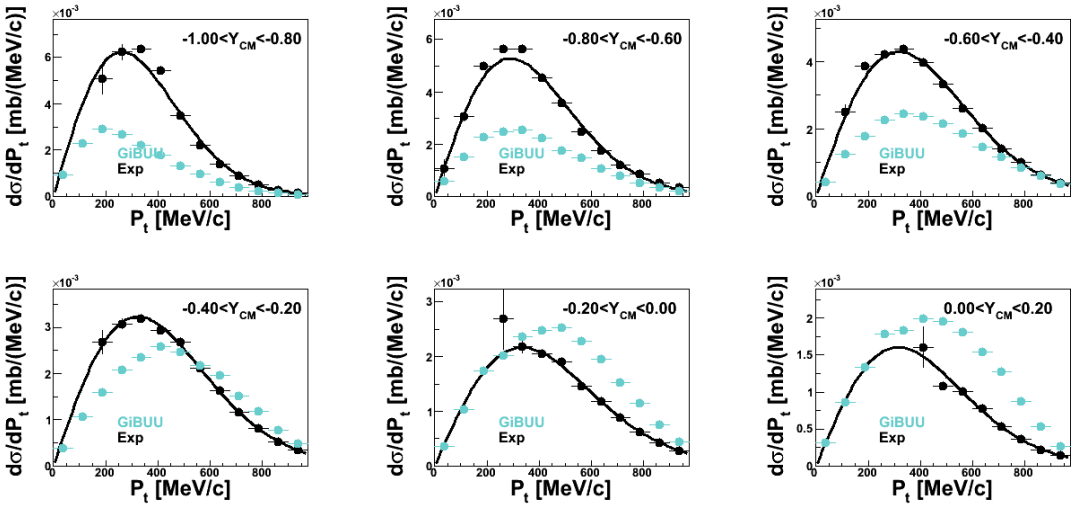

Figure 4.9: GiBUU model with scaled production cross sections and elastic Λ-nucleon scattering switched off.

The plot illustrates that the lower rapidities are only slightly influenced by elastic scattering as implemented in the model. Theoretical calculations predict that through

in-medium modifications the elastic Λp cross section decreases (see for example Figure 4.13 in the summary). This could be a hint that the region of target rapidity is mainly populated by Λs produced through inelastic channels. To investigate this and increase the absorption of Λs in the model we set the transition energy from the Tsushima resonance model to the PYTHIA model back to its default value, which is for baryon-baryon collisions $\sqrt{s} = 2.6$ GeV. With a proton kinetic energy of 3.5 GeV we reach a nucleon-nucleon collision energy of $\sqrt{s_{NN}} = 3.18$ GeV. Therefore, the first collision is for sure calculated within PYTHIA, but also secondary collisions could have enough energy to be over the threshold. The result is displayed in Figure 4.10.

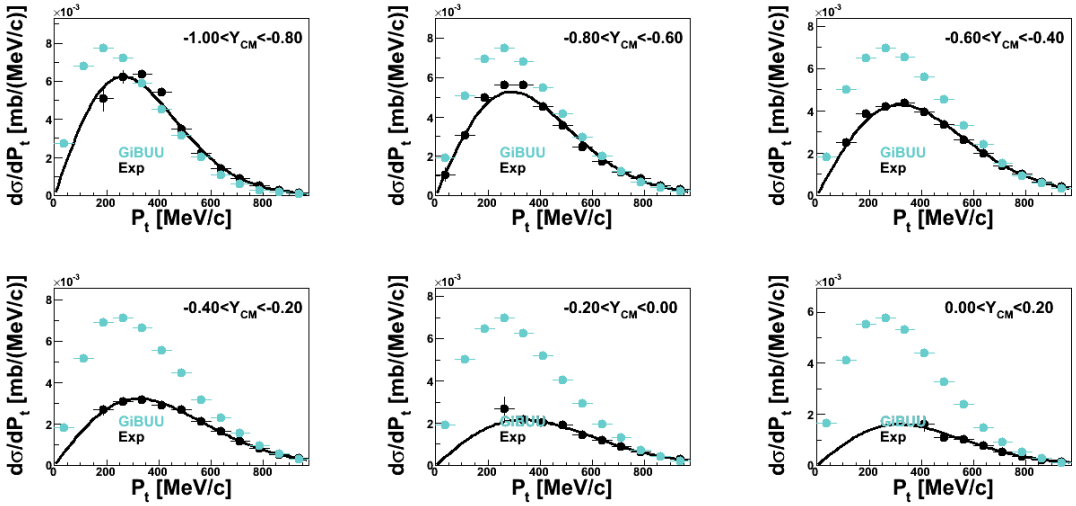

Figure 4.10: GiBUU model with the PYTHIA threshold set to its default value.

The simulation yield at lower rapidity is enhanced in comparison to simulations without using PYTHIA and is in better agreement with experimental data. This confirms the assumption that Λs in this region are mainly coming from additional inelastic channels. But additionally, also the yield at large rapidities is dramatically increased. This is an indication that it is not reasonable to use PYTHIA for strangeness production at SIS18 energies, at least for Λs. PYTHIA is in general designed on the "parton level" (quarks, gluons) with interactions using e.g. "hard processes" and has its strength in the energy region of tens to hundreds GeV (and is tuned to fit LHC data).
In a last step we simulated the p+Nb reaction with the *real mode* approach without using PYTHIA but including the scaling of production cross sections, which can be seen in Figure 4.11.

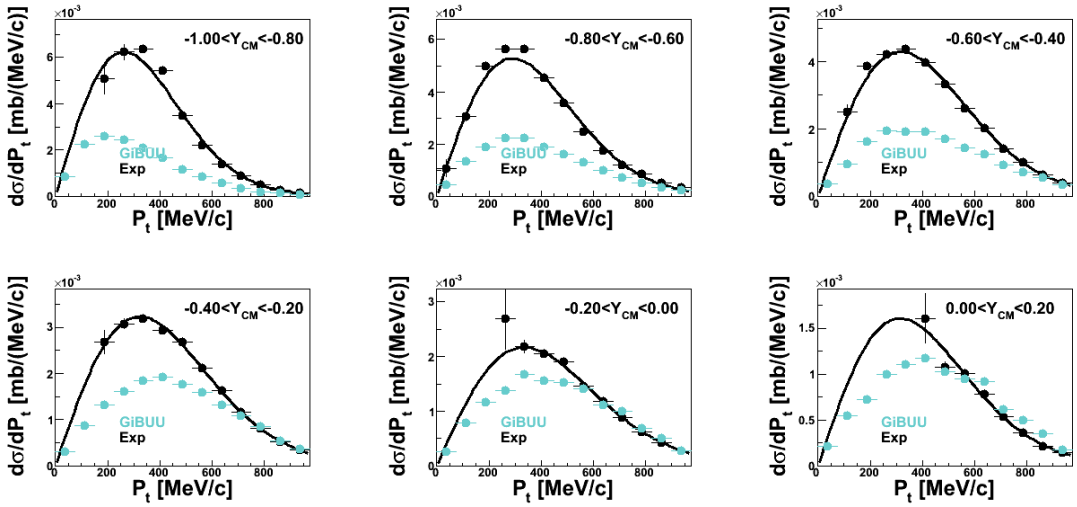

Figure 4.11: GiBUU model simulated in real mode. See text for further details.

We find no dramatic change in comparison to *perturbative* simulations based on the resonance model only. This we would expect because the number of participants in a p+Nb reaction at 3.5 GeV energies is about ~ 2.7 [Elg13], which is an indication that the requirements for a perturbative simulation are fulfilled. We can exclude the option that the data was not described by GiBUU because of using the wrong simulation mode. In conclusion, for fast checks of parameter changes it is reasonable to use the perturbative mode, for a more detailed investigation it is necessary to switch to the real mode. Especially for exploring in-medium modifications of hadrons it is mandatory to use real mode simulations.

4.5.3 Summary

We saw that UrQMD describes reasonably well the trend of the experimental distributions but fails to reproduce the yields. Especially, the "difficult" region of lower rapidities is populated by Λs. This could be a hint that in this range the mechanism of resonance decay becomes important. For instance the reaction:

$$NN \rightarrow N^*N \rightarrow NYK$$

where the resonance is explicitly produced and can scatter in the nucleus with other nuclei. Therefore, the angular distribution of Λs is influenced by its decaying mother resonance which could be an explanation why UrQMD describes better the stopping of Λs in the nucleus. An indication for resonance production was found in an experimental investigation of the two hyperon production channels $pp \rightarrow \Sigma^0 pK^+$ and $pp \rightarrow \Lambda pK^+$ for three different beam momenta ($p_{beam} = 2950, 3059, 3200$ MeV/c) performed by the COSY-TOF collaboration [Abd10]. For the $pp \rightarrow \Lambda pK^+$ they found a strong evidence for an intermediate resonance production $pp \rightarrow N^*p$ with the resonances $N(1650)S_{11}$, $N(1710)P_{11}$, and $N(1720)P_{13}$ by studying the differential cross section in the CM, Jackson, and helicity frames. This finding supports the argument that UrQMD describes the data better at low rapidities because it uses intermediate resonances for particle production.
A study of the global yield of the UrQMD output reveals a general overestimation especially at the HADES experimental accessible phase space edges. Fortunately, we have data

of a Λ analysis in p+p reactions where we are able to better constrain the production mechanism of Λs including angular distributions, branching ratios and production cross sections of the decaying resonances. The global behaviour of UrQMD can be best seen in the rapidity-density distribution in Figure 4.12. The shape of simulation data is in agreement with experimental data points but the yield is too high.

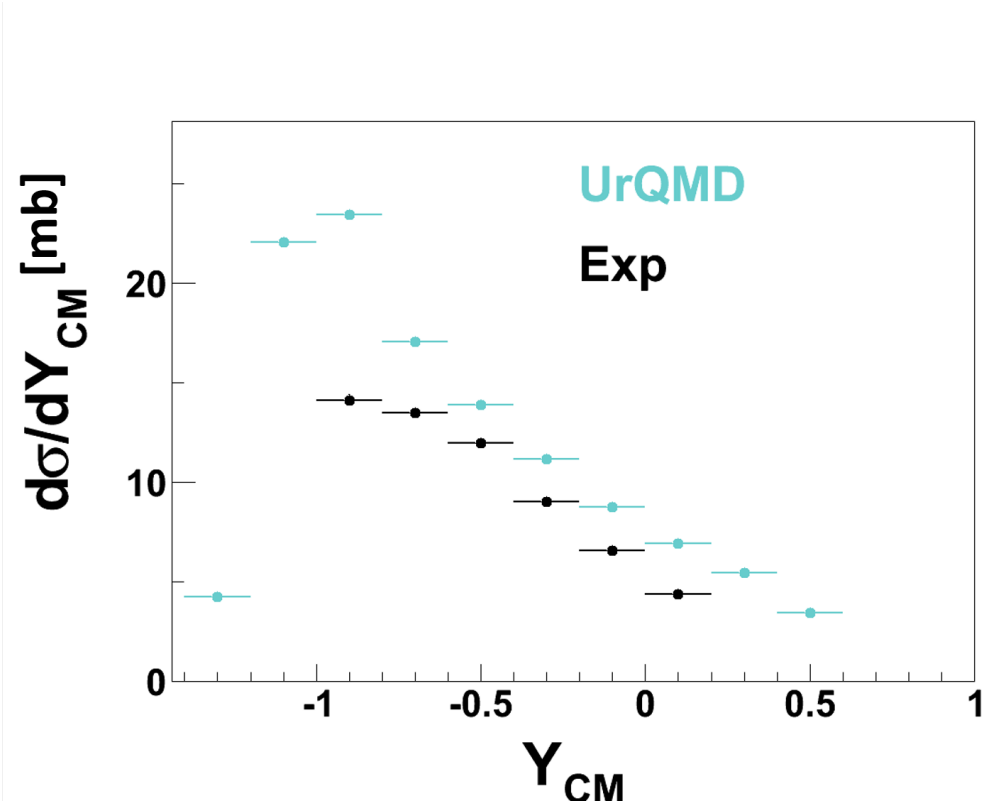

Figure 4.12: Rapidity-density of Λ hyperons (black) in comparison with UrQMD data (cyan).

The GiBUU model delivers a worse agreement. The overall yield of the original model shows some imbalance with an overestimation at larger rapidities and underestimation of experimental data in the region of target rapidity. At large values of rapidity GiBUU is mainly sensitive to the tuning of production cross sections. If we scale down the cross sections for elementary production the data gets in better agreement with experimental points. At lower rapidities the shape is completely off, which we account for some missing inelastic mechanism which causes that the absorption of Λs is not correctly implemented in the model.
In GiBUU, hyperons are produced directly in elementary reactions e.g. $NN \rightarrow NYK$ without any intermediate resonances. This could explain the large difference to the UrQMD model that a produced resonance which decays to a kaon hyperon pair plays an important role in the stopping kinematics of hyperons and their angular distributions.
Also the modifications of cross sections due to in-medium effects is presently not incorporated in the model, which are mainly changed due to Pauli blocking. The dependency of the cross sections on the surrounding medium is illustrated in Figure 4.13 which shows the total cross section as a function of the Λ energy. The green line corresponds to the experimental case of ground state density in the Niobium nucleus. However, the authors of this calculations point out that the incorporation of cross section modifications to the GiBUU model is in progress [Gai13]. The effect of including the correct cross section will be tested in future.

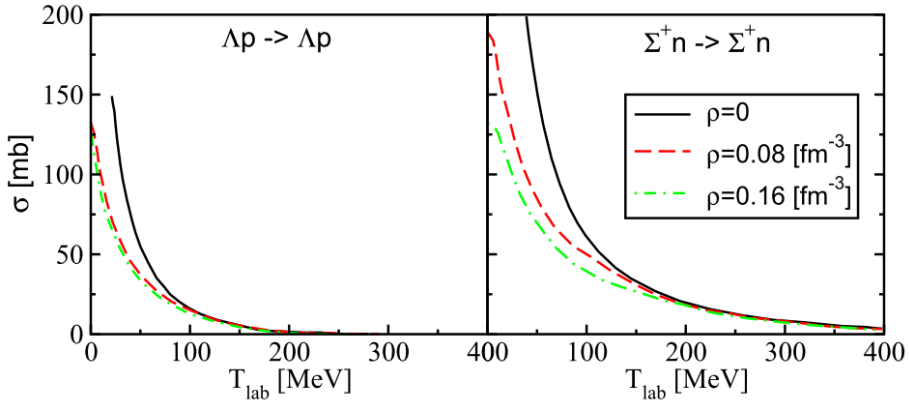

Figure 4.13: In-medium modifications of YN cross sections with increasing density according to [Gai13]. The green line corresponds to the case of saturation density in the Niobium nucleus.

The global behaviour of the simulation model can be also studied by looking at the rapidity distribution shown in Figure 4.14 (with production scaling). At large rapidities GiBUU is able to reproduce the experimental yield and the trend of the data. In this region the model is mainly sensitive to the tuning of Λ production channels. At around $y_{CM} < -0.4$ the distribution is no longer in agreement with experimental data. GiBUU predicts a more or less flat integral yield, whereas the experimental data is still rising going from large to low rapidities. We trace this effect for missing or wrong parametrized (inelastic) scattering channels.

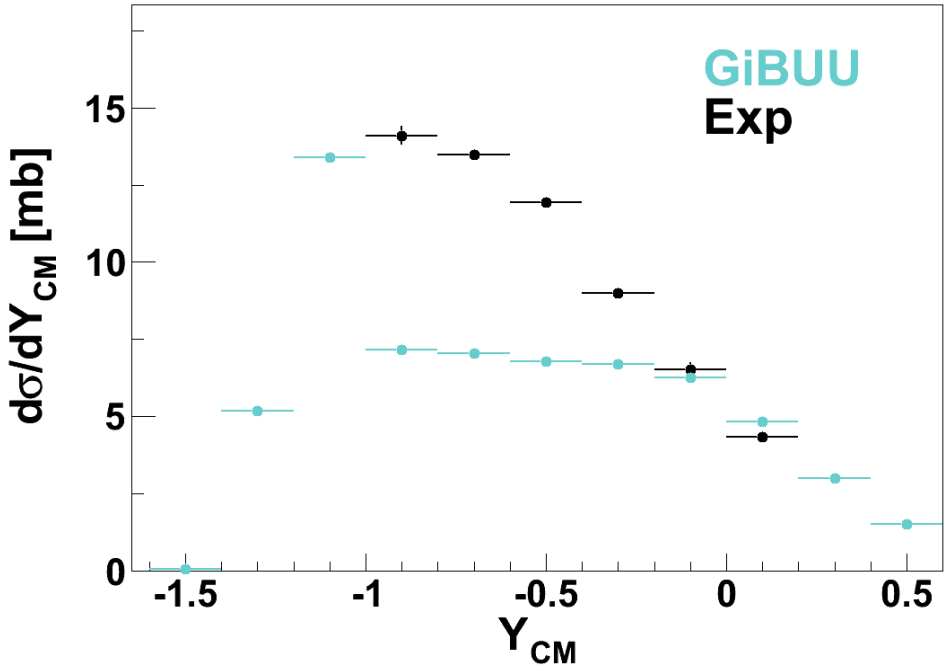

Figure 4.14: Rapidity-density distribution of experimental data in comparison with the GiBUU model (with scaled production cross sections).

5 Intensity Interferometry - proton-proton correlations

5.1 From heaven to earth

In the 50s, R. Hanbury Brown and R. Q. Twiss (HBT) developed a method called intensity interferometry to measure correlations between beams of light [Han56b]. If we think about interferometry then mostly about the case of amplitude interferometry. One of the most famous experiments of amplitude interferometry is the Young's experiment commonly known as the double-slit experiment, which became famous by revealing the mysterious properties of quantum mechanics. This kind of experiment is based on measuring a single-particle detection probability, whereas the HBT method is footed on determining the two-particle probability [Lis93]. A schematic view of both interference types is shown in Figure 5.1.

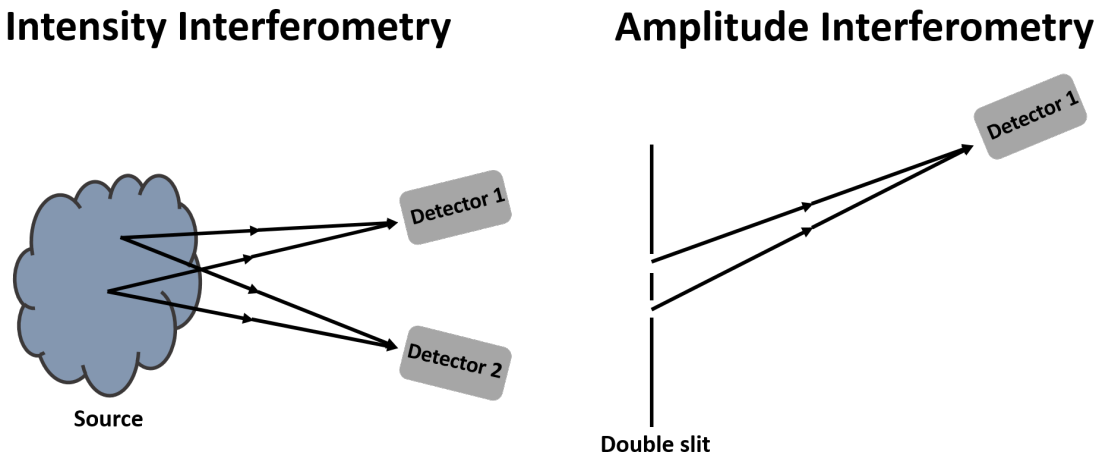

Figure 5.1: Schematic comparison of intensity (left panel) and amplitude interferometry (right panel) according to [Lis93]. In the intensity interferometry case the emitted quanta can travel two different paths respectively, which leads to interference effects.

The method of intensity interferometry consists of the measurement of the two-particle coincidence yield n_{12} and of the single particle yield n_1 and n_2. Out of these quantities the following correlation function is built:

$$C(\mathbf{p}_1,\mathbf{p}_2) = \frac{\langle n_{12} \rangle}{\langle n_1 \rangle \langle n_2 \rangle} \ . \tag{5.1}$$

The correlations are included in the coincidence yield and can be used to extract information about the source size of the light emitting system (we will present an example in the next section). Hanbury Brown and Twiss developed the formalism and applied it to radio-astronomy to measure (angular) source sizes of astronomical objects (e.g. they measured

the apparent angular source size of Sirius [Han56a]).
Independently in the 60s, Goldhaber *et al.* [Gol60] observed in an experiment of proton anti-proton annihilation an angular correlation among like sign pion pairs $\pi^{\pm}\pi^{\pm}$. The experiment originally aimed for finding the ρ_0 resonance with its decay into a $\pi^{-}\pi^{+}$ pair. They realized that this correlation was explainable with using Bose-Einstein statistic that governs the interaction between identical bosons due to wavefunction symmetrization. This was the starting point of using the HBT interferometry in high energy particle physics (called there the GGLP effect, but usually also in particle physics very often the term HBT is used).
Later in the year 1977, Koonin developed a model for two-particle correlations using protons to probe the reaction dynamics of a system at intermediate energies [Koo77]. If two protons are emitted from the same source, they interact via Coulomb and strong interactions. Additionally, the total wavefunction must be anti-symmetrized to obey the Fermi-Dirac statistic. For small source sizes the positive correlation due to the nuclear interaction dominates over the anti-correlation induced by the electromagnetic interaction between both protons and fermionic quantum statistic.
The discovery of the HBT effect in particle and nuclear physics opened a new field of research, which is nowadays called *femtoscopy*, because with such interference experiments one can resolve space-time characteristics of evolving systems at the fermi scale ($\sim 10^{-15}$ m). This became very important in analyses of heavy-ion reactions to gain information about the highly excited matter formed in the collision region of the two overlapping nuclei by studying correlations of the emitted particles. Modern analyses are able to extract extent, shape, orientation, and dynamical characteristics of the emission zone [Lis10].

5.2 Theoretical basics

5.2.1 The origin of the HBT effect

The correlation function is an abstract object. We want to give an illustrative description of HBT physics in a classical picture, which is based on considerations extracted from [Bay98]. One can think of two sources a and b separated by a distance R emitting spherical waves $\alpha \exp(ik|\vec{r}-\vec{r}_a| + i\phi_a)/|\vec{r}-\vec{r}_a|$ and $\beta \exp(ik|\vec{r}-\vec{r}_b| + i\phi_b)/|\vec{r}-\vec{r}_b|$, where α, β are the amplitudes of the waves and the ϕ_i are random phases. The waves are measured with two detectors at a distance L, which are separated by a distance d as illustrated in Figure 5.2.

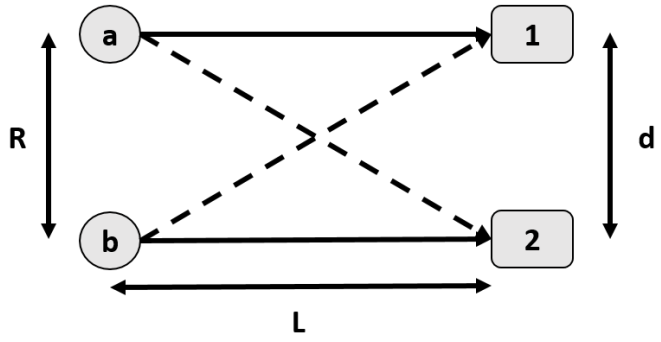

Figure 5.2: Two sources a and b emitting spherical waves, which are measured by the detectors 1 and 2.

With all this information one can calculate all relevant quantities, for example the total amplitude of both waves at the position of detector 1:

$$A_1 = \frac{1}{L}\Big(\alpha \exp(ikr_{1a} + i\phi_a) + \beta \exp(ikr_{1b} + i\phi_b)\Big), \tag{5.2}$$

where r_{ij} is the distance from source j to detector i. The observables used for light interferometry are the averaged (over the random phases ϕ) intensities derived from the squared amplitudes. The uncorrelated reference probability is simply the product of the single particle intensities $\langle I_1\rangle \cdot \langle I_2\rangle$. First multiplying and then averaging gives the potential coincidence yield $\langle I_1 I_2\rangle$. To extract the correlation signal we divide both signals. If no correlation would be present the ratio would be exactly one. For large separations of detectors and sources $L \gg R$ we obtain:

$$C(\vec{d}) = \frac{\langle I_1 I_2\rangle}{\langle I_1\rangle \langle I_2\rangle} = 1 + 2\frac{\langle |\alpha|^2\rangle \langle |\beta|^2\rangle}{\left(\langle |\alpha|^2\rangle + \langle |\beta|^2\rangle\right)^2} \cos(\vec{R}\cdot(\vec{k}_2 - \vec{k}_1)), \tag{5.3}$$

where $\vec{k}_i = k\hat{r}_i$ is the wavevector of the light seen in detector i. A correlation signal remains, which is induced by interference effects between both light waves and is interpreted on a quantum mechanical level as the influence of Bose-Einstein statistic acting between the identical photons. The latter correlation term in Equation (5.3) varies on a length scale $d = \lambda/\Theta$, where λ is the wavelength of the light and $\Theta = R/L$ the angular size of the source. By changing the separation d of the two detectors one can gain information about the extent of the light emitting system.

5.2.2 The Koonin-Pratt formalism

As we have seen, the HBT effect (in astronomy) can be interpreted as the interference between identical light-particles (photons). The mathematical framework in particle physics to calculate correlations between two particles which incorporates all the interactions between them is the Koonin-Pratt formalism [Koo77, Pra84, Pra87]. A central ingredient is the emission function also often called source function $g(\mathbf{p},x)$, which is a measure of the probability that a particle with momentum p is emitted at a space-time point x. The relation of the coincidence yield to microscopic quantities is given in the equation:

$$C(\mathbf{P},\mathbf{q}) = \frac{P(\mathbf{p}_1,\mathbf{p}_2)}{P(\mathbf{p}_1)P(\mathbf{p}_2)} = \frac{\int d^4x_1 d^4x_2 g(x_1,\mathbf{p}/2) g(x_2,\mathbf{p}/2) |\phi(\mathbf{q},\mathbf{r}_1 - \mathbf{r}_2 - \frac{t_1-t_2}{2m}\cdot\mathbf{P})|^2}{\int d^4x_1 g(x_1,\mathbf{p}/2) \int d^4x_2 g(x_2,\mathbf{p}/2)} \tag{5.4}$$

where $\mathbf{q}$ is the relative momentum between the two particles in the pair rest frame and $\mathbf{P}$ is the total momentum of the pair. The correlations which means all interactions of both particles are included in the relative wavefunction $\phi(\mathbf{q},\mathbf{r}_1 - \mathbf{r}_2 - \frac{t_1-t_2}{2m}\cdot\mathbf{P})$. The proton-proton correlation function includes three interactions (Strong, Coulomb, Pauli). For this reason it is necessary to solve the corresponding equations for the wavefunction and correlation function numerically (no explicit analytical form exists).
Two main assumptions are needed to construct Equation (5.4) [Lis93]. The first one is that both particles are emitted independently. The second particle never knew that the first particle left the source. This means, there are no additional correlations within the source and the correlations between both particles are only due to final state interactions. The second assumption is that the particles only interact with each other and not with the residue nucleus (or other fragments). The physical picture is that two particles are emitted

by the source and then the interaction is switched on, which is the reason why the final probabilities are correlated $P(\mathbf{p}_1,\mathbf{p}_2) \neq P(\mathbf{p}_1)P(\mathbf{p}_2)$ [Lis93].
We want to study correlations between protons produced in the p+Nb reaction. We do this as a function of the relative momentum in the CM system of both protons:

$$k = \frac{1}{2}|\mathbf{p}_1^* - \mathbf{p}_2^*|, \quad \mathbf{p}_1^* + \mathbf{p}_2^* = 0 \tag{5.5}$$

This definition of the relative momentum k is equivalent to the also often used Lorentz-invariant "q-vector":

$$q \equiv \frac{1}{2}\sqrt{-q_\mu q^\mu} = \frac{1}{2}\sqrt{(\mathbf{p}_1 - \mathbf{p}_2)^2 - (E_1 - E_2)^2} \overset{\text{CMS}}{=} \frac{1}{2}\sqrt{(\mathbf{p}_1^* - \mathbf{p}_2^*)^2} = |\mathbf{p}_1^*| = |\mathbf{p}_2^*| = k \tag{5.6}$$

where the * labels 3-vectors in the CM system. The source is often parametrized *a priori* in a Gaussian way neglecting any time dependence (which implies also no momentum dependence) with only one free parameter left, the source size R_g:

$$g(x,\mathbf{p}) \sim \delta(t) \exp -(|\mathbf{r}|/R_g)^2 \tag{5.7}$$

With this assumption of the source size together with the interactions between the particles the correlation function can be calculated with the Koonin-Pratt formalism. In Figure 5.3 an example of two proton-proton correlation functions $C(k)$ is plotted using two different Gaussian sources ($R_g = 2{,}3$ fm).

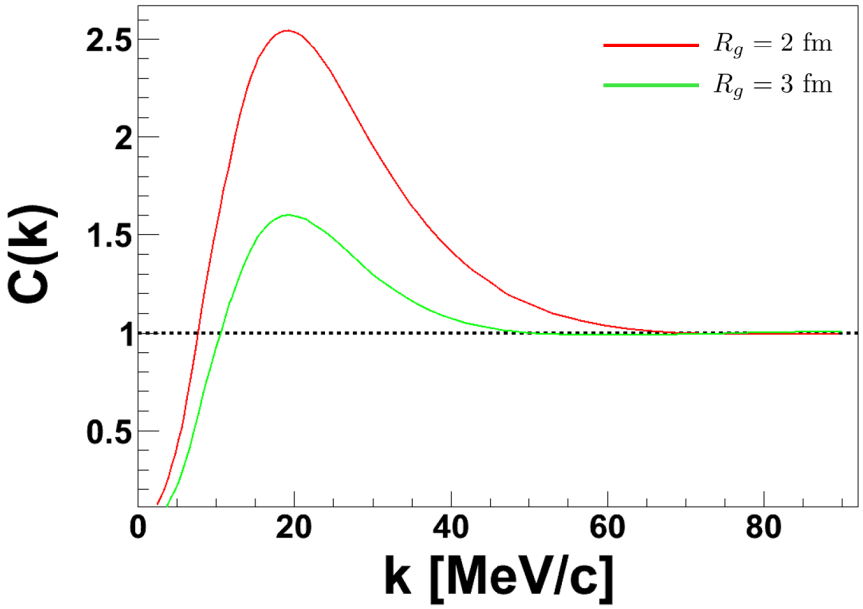

Figure 5.3: Proton-proton correlation function $C(k)$ calculated for two different source sizes according to the Koonin formalism.

It shows some anti-correlation behaviour in the momentum range $0 < k < 10$ MeV/c. This is induced by Pauli blocking and Coulomb repulsion acting between identical and charged fermions. The electromagnetic repulsion is a long range interaction and prevents the particles from ever having precisely equal finite momenta, which implies $C(k = 0) = 0, \forall R_g$.

The peak at $k \approx 20$ MeV/c is a characteristic feature of the attractive S-wave nuclear interaction between both protons (the magnitude of the S-wave scattering length is quite large of about 20 fm [Led01]). Its contribution to the (positive) correlation signal scales as $(a/r)^3$ [Koo77], where a is the range of the nuclear force. This explains the inverse behaviour of the attractive part in the correlation function, namely the larger the source the lower is the peak height, which is also illustrated in Figure 5.3, where the positive correlation dip decreases when going from a source size of $R_g = 2$ fm to $R_g = 3$ fm.

5.3 Experimental correlation function

The experimental correlation function is constructed as follows:

$$C(k) = \frac{P(\mathbf{p}_1,\mathbf{p}_2)}{P(\mathbf{p}_1)P(\mathbf{p}_2)} = \mathcal{N}\frac{N(k)_{\text{real}}}{N(k)_{\text{mixed}}} \cdot \Big(\xi(k)\Big). \tag{5.8}$$

The ingredients are $N(k)_{\text{real}}$ which denotes the momentum distribution (in the proton-proton CM system) of protons taken from the same event. $N(k)_{\text{mixed}}$ is the distribution of momenta using protons that belong to different events. By construction these protons could not be correlated. The event mixing technique is based on the principle that the mixed event "background" distribution has every physical property, i.e. the particle kinematics, correctly inside and is identical to the signal in all respects except of femtoscopic correlations. After calculating the ratio of both distributions the correlations between particles should remain. The function $\xi(k)$ normally plays a minor role and is used to parametrize possible long-range correlations (we do not consider long-range correlations in the analysis because they play a minor role and make itself felt by a raising of the correlation function for momenta $k > 100$ MeV/c). The normalization factor $\mathcal{N}$ is an important quantity, because it influences the peak height of the proton proton correlation (which means the extracted source size). It is chosen in a way that the correlation function is equal to one, where no correlations between the particles are expected ($C(k \gtrsim 100$ MeV/c$) = 1$).

5.3.1 Construction of the correlation function

In the inclusive Λ analysis we identified protons and negative pions with the information of their energy loss in the MDCs. Our analysis in this case was not very sensitive to misidentification because fake $p\pi^-$-pairs gave only contributions to the combinatorial background in the invariant mass distribution, which was subtracted afterwards.
When we construct the correlation function, we immediately check the identified protons for correlations without the intermediate step of subtracting misidentified particles. To reduce wrong correlation signals caused by misidentification, we improve the particle identification procedure. First, we use tighter graphical cuts in the energy loss vs. momentum plot and second, we use an additional particle information provided by the META system, namely the relation of the particle velocity $\beta = v/c$ to the momentum p. The relation reads as follows:

$$\beta(p) = \frac{p}{E} = \sqrt{\frac{p^2}{p^2 + m^2}}\ . \tag{5.9}$$

We see that Equation (5.9) has the particle mass m as free parameter inside. Different particle masses lead to different curves $\beta(p)$. This can be used to introduce additional

graphical cuts in the β vs. momentum distribution. A particle is only identified as a proton if it fulfills the dE/dx as well as the β graphical cut as a function of momentum. Figure 5.4 displays the dE/dx and β distributions for all charged particles separately together with the chosen graphical cut conditions, which are plotted as red dashed lines. In the right panel it is nicely shown that different particle species lead to separate curves in the β vs. momentum plot and we have nearly no overlap with contributions from other particles.

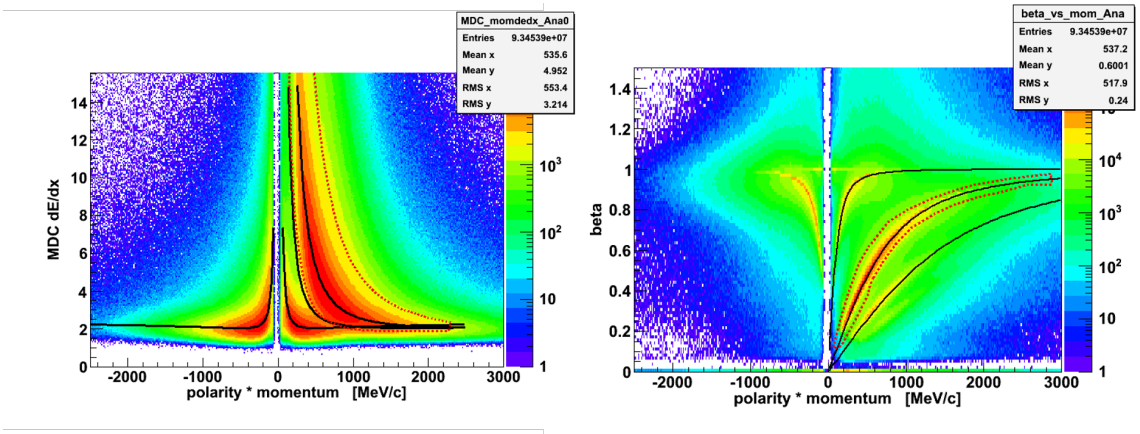

Figure 5.4: Protons are identified with the information from the energy loss and β vs. momentum distribution. We use graphical cuts illustrated by red dashed lines. If the particle passes both cut conditions it is identified as a proton.

With the identified protons we can start the correlation analysis. We expect correlations only between primary protons. To select primary protons we employ again the condition that the primary vertex calculated with all tracks from the event must lie inside the target cylinder, exactly as in the inclusive Λ analysis. Proton pairs identified as primary particles are treated further with determining the relative momentum (in the pair rest frame), which gives us in the end the momentum distribution for real events.
The relative momentum distribution for mixed events is more complicated to calculate. The procedure is to take a proton from event x and "correlate" it with a proton from event y, where $x \neq y$. To not introduce some additional (fake) correlations (i.e. long-range correlations appear due to the violation of energy and momentum conservation for mixed events) we try to stay as close as possible to the real event case. For this reason we applied two selection criteria. The first selection criteria is that the protons should stem from the same multiplicity class, which ensures that both protons have similar kinematics due to comparable impact parameters. In addition we use a second criteria that the protons should come from the same target region of the reaction. Both selections guarantee that the events which should be mixed have a very similar structure. To satisfy both requirements, we define multiplicity classes and target classes to classify the events. The size of this classes is a compromise between accuracy and enough statistic for the mixed event construction. We used the following values for multiplicity classes listed in Table 5.1 and for target classes listed in Table 5.2:

Multiplicity class	*Multiplicity (Charged particles)*
1	1-2
2	3-4
3	5-6
4	7-8
5	>8

Table 5.1: Definition of multiplicity classes used for the mixed event calculation.

Target class	*Target region (z-component) [mm]*
1	0-5
2	5-10
3	10-15
4	15-20
5	20-25
6	25-30
7	30-35
8	35-40
9	40-45
10	45-50
11	50-55
12	55-60

Table 5.2: Used target classes for the mixed event calculation.

We use the number of tracks in an event as multiplicity definition and the z-component of the primary vertex calculated with all tracks of an event as the target position of the particles. The events first have to pass the primary vertex selection and are then sorted by using their multiplicity information according to the defined multiplicity classes to be filled in *multiplicity pools*. If one pool is full the events are mixed, but only events which lie in the same target region. We have five multiplicity pools due to five multiplicity classes and in every pool 12 vertex classes respectively, which give $5 \times 12 = 60$ possible combinations of mixing. A short example: lets imagine we would have two events 1, 2 and event 1 would have five tracks inside and event 2 six. According to the prior multiplicity definition they are shifted to the *multiplicity pool* 3. If they would also lie in the same target class they are mixed after the multiplicity pool is filled with a certain number of events. The number of events which are necessary to fill one *multiplicity pool* is completely arbitrary and we have chosen 50 events (the chosen value should be not too large because the events should be measured close in time to have similar "environment" e.g. beam characteristics). With this procedure we can produce large statistic mixed event samples, normally one order of magnitude larger than the samples of real events. This means that the statistical errors in

the correlation function are governed only by the real event statistical errors. In Figure 5.5 we have plotted the proton pair distribution for real events (black) and mixed events (red) as a function of their relative momenta. Both distributions look quite similar, which indicates that the mixing method works reasonable.

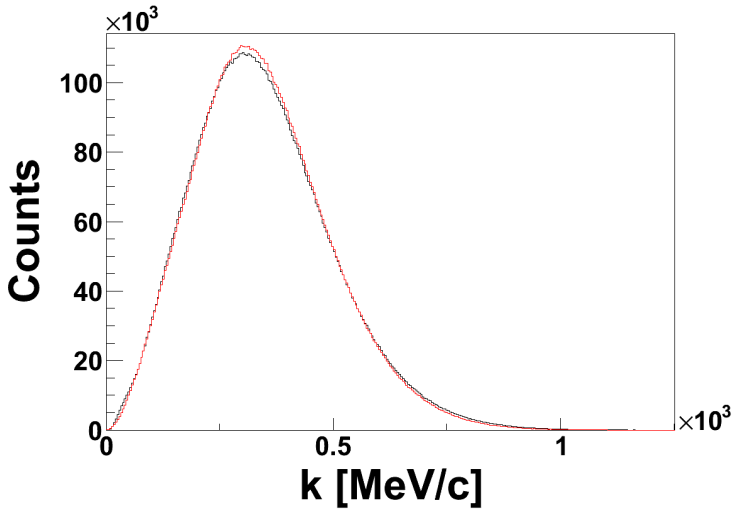

Figure 5.5: Comparison of the relative momentum distribution for real (black) and mixed (red) events. Both curves look very similar which illustrates that the event mixing method works reasonable.

With both distributions we can determine the correlation function by simply calculating the ratio of both distributions of Figure 5.5 (with a higher statistic for mixed events). This is illustrated in Figure 5.6 as a function of the relative momentum.

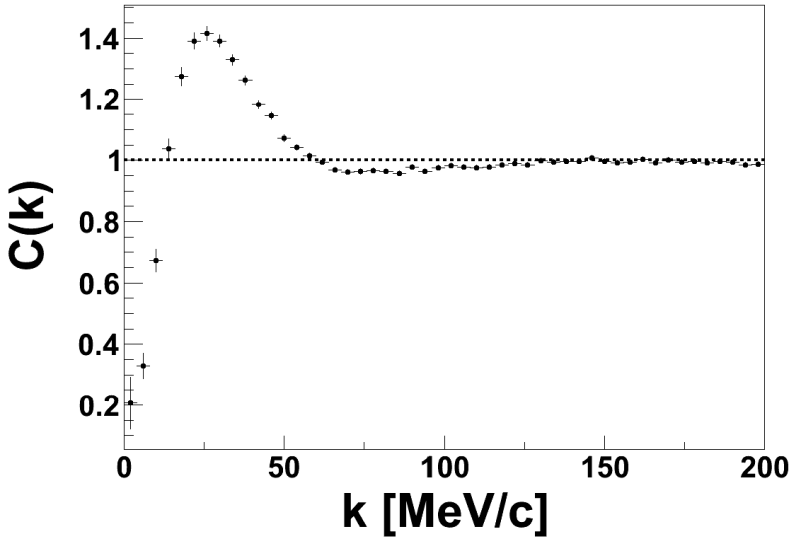

Figure 5.6: Correlation function for proton pairs determined with the methods explained in the text.

The experimental curve shows the expected behaviour with a suppression at small relative

momenta and a positive correlation due to S-wave nuclear interactions at $k \approx 20$ MeV/c. The real and mixed event distribution were both measured within the HADES acceptance. For this reason we have to take into account several efficiency effects, which we will explain in the next section.

5.3.2 Corrections

As discussed above, particle correlations become visible at small relative momenta in the CM frame of the two protons. Using the Heisenbergs uncertainty relation one can estimate the angle e.g. of the effect of wavefunction anti-symmetrization [Koo77] in the laboratory frame. The quantum statistic effect induces an anti-correlation over a range of relative momenta $\Delta p \approx \hbar/r$, which is translated to an angular anti-correlation $\Delta\phi = \Delta p/p \approx \hbar/rp$. For $r = 3$ fm and $p = 531$ MeV/c the estimation leads to $\Delta\phi = 7.1°$.
This illustrates, that the correlated pairs have a small opening angle in the laboratory frame. For close pairs the detector could have problems to distinguish both particle tracks. This effect is called track merging, because it could happen that two distinct tracks are merged together to one track. In the mixed event procedure we use always two different tracks by construction. If in the real event sample tracks are merged than they are missing and fake anti-correlations are introduced to the correlation function. To correct for this effect we use simulations and created a sample of protons with help of the UrQMD transport model and process it through the whole analysis chain (full scale analysis). After full scale analysis we calculate the correlation function as the ratio of real and mixed events exactly in the same way as in the experimental case. UrQMD calculates single-particle phase space distributions until their last collision (freeze-out). However, final state interactions are defined as interactions which happen after particles are emitted from a source, which means after freeze-out. For this reason, in UrQMD no final state interactions are included, which should result in a flat curve over all relative momenta (we present a method to calculate correlation functions from semi-classical transport theories in section 5.4). Deviations from a flat function have their origin in detector effects. The resulting correlation function obtained from UrQMD is plotted in Figure 5.7.

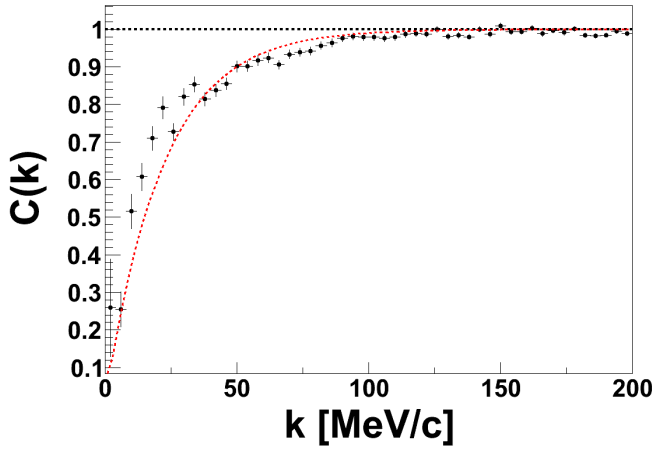

Figure 5.7: Correlation function determined with the UrQMD model. At small relative momenta the correlation function deviates from its expected flat behaviour, which can be accounted to track merging. The red dashed line is the correction function used to get rid of close track efficiency effects.

The correlation function shows some suppression at low relative momenta (also no nuclear S-wave peak is seen, which is a clear hint of missing final state interactions in the UrQMD model). We attribute the shown anti-correlation at small relative momenta in simulations to track merging during the tracking process. In future, we will simulate more statistic to better clarify the trend of the suppression at very small relative momenta $k < 20$ MeV/c. We can parametrize this effect with a correction function of the form:

$$f_{\mathrm{acc}}(x) = 1 - \exp(-a \cdot x/b), \tag{5.10}$$

where the chosen function automatically converges to the flat behaviour of the correlation function at large k. The corrected correlation function is calculated as follows:

$$C(k)_{\mathrm{corr}} = C(k)_{\mathrm{measured}}/f_{\mathrm{acc}}(k). \tag{5.11}$$

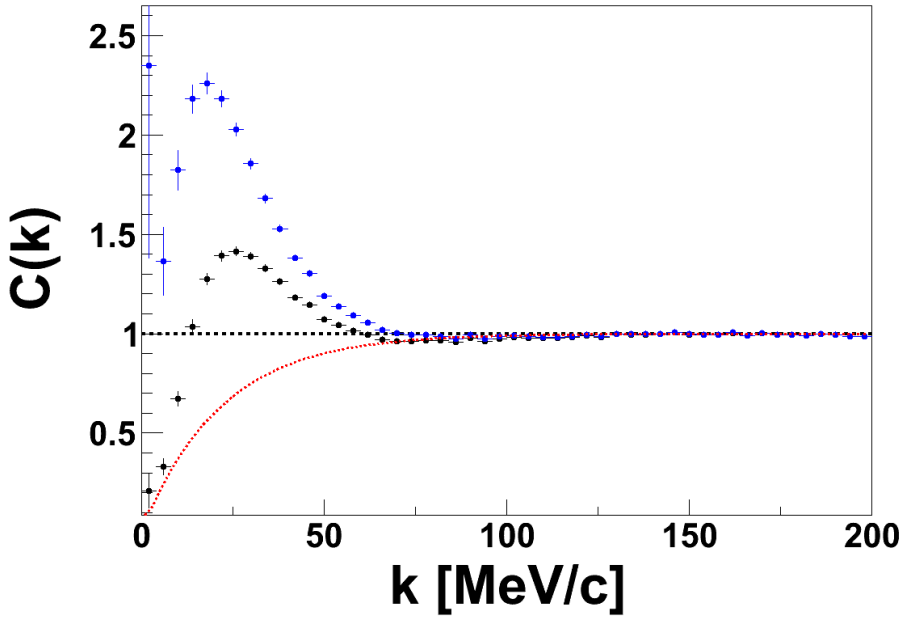

Figure 5.8: Effect of close track efficiency correction. The black curve illustrates the uncorrected curve, whereas the blue one shows the correlation function after correction using the red dashed correction function.

We see in Figure 5.8 that the peak height of the correlation function after the correction with the red dashed function increases, which results in a smaller Gaussian source size of the p+Nb system (which was suppressed due to track merging). The correction for very small relative momenta k seems not reasonable, because the data point after correction shows not the expected trend anymore.
Another efficiency effect we have to take into account is the finite momentum resolution of the detector. To check the influence of the finite resolution in the momentum reconstruction we used the event generator UrQMD to generate a proton phase space and extracted an ideal (no resolution effects) correlation function (how it is done is explained in the next section). Then we smeared the momenta of UrQMD with a resolution of $\Delta p/p \approx 1 - 2\%$

and calculated the correlation function again. The result is plotted in Figure 5.9 where the black correlation function corresponds to the ideal case of no smearing and the red curve is obtained after momentum smearing.

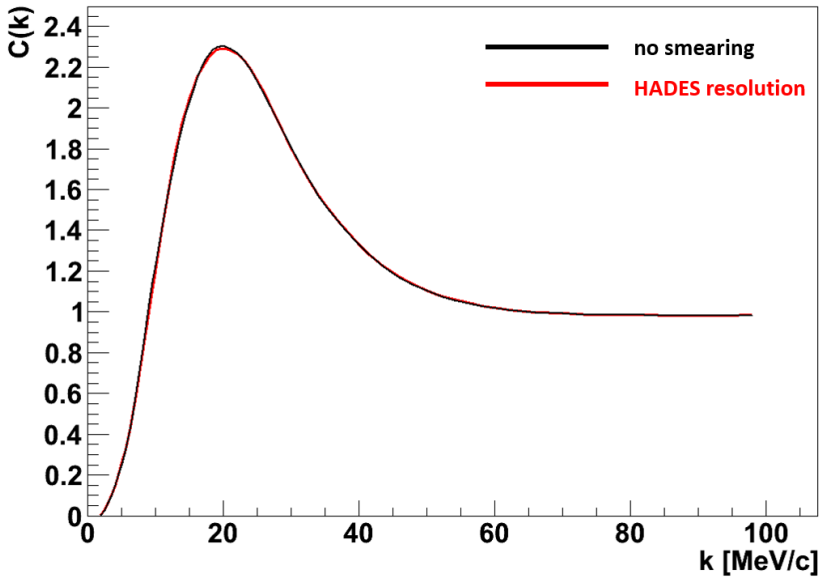

Figure 5.9: The effect of finite momentum resolution. The black curve shows the ideal case whereas red is obtained by phase-space points with smeared momenta $\Delta p/p \approx 1 - 2\%$.

This indicates that the finite momentum resolution plays a minor role in constructing the correlation function. That the influence of momentum resolution is a small effect was also reported by other collaborations e.g. by STAR, which constructed a Λp correlation function [Ada06].

5.3.3 Determination of the source size

The Koonin-Pratt equation delivers different correlation functions for different Gaussian source sizes R_g. To determine the source size of the p+Nb system at a proton energy of 3.5 GeV, we compare theoretical curves with the experimental data. The important quantity for the comparison of the correlation function with theory is the peak height. With a Gaussian source size of $R_g = 2.2$ fm we can reproduce the peak height of the system displayed in Figure 5.10. The grey band shows the systematic errors from the uncertainty in the close track correction by a variation of the parameters in a 20% range. This gives us an systematic error in the source size of $R_g = 2.2^{+0.23}_{-0.22}$ fm. What attracts the attention is that the width of the experimental curve is not reproduced by the theoretical model. This seems to be a hint that the source of the particle emitting system is of non Gaussian form, which was the assumption of the model. Such results were also found in other measurements of proton-proton correlations e.g. in Ar+KCl reactions in a similar energy range $\sqrt{s_{NN}} = 2.61$ GeV [Aga11a] or in Ca+Ca reactions at different projectile energies [Kot04].

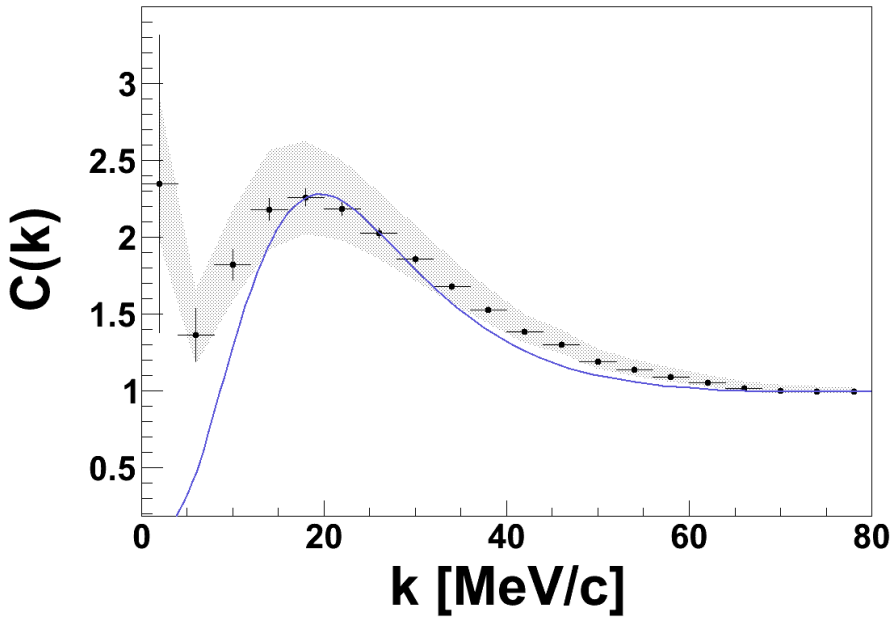

Figure 5.10: Experimental correlation function compared to the Koonin model with a source size of $R_g = 2.2$ fm (blue solid line). The grey band shows the uncertainty from the close track correction by varying the parameters by 20%.

The issue of using Gaussian sources was discussed in more detail by the authors of [Ver02]. They point out that most correlation functions in experiment can only reproduce the height, but not the width and want to understand if the non Gaussian dependency has its origin in the way the protons are emitted. Their main assumption is, that the proton emission has two components involving completely different time scales: a fast component and a much slower component that might originate from long time secondary decays, which give different contributions to the two-proton source. They define a simple two-component model (STCM) based on following assumptions of the emission process:

- an instantaneous fast component ($\tau_1 = 0$)
- a slow component with a sufficiently long decay time scale such that its correlation function is negligible ($\tau_2 \approx \infty$)

Lets define P_1 as single particle probability and $R(k)$ the correlation part in the correlation function $C(k) = 1 + R(k)$. One can subdivide with the above assumptions the single particle probabilities into a fast emission component $P_{1,fast} = fP_1$ and the remaining slow part $P_{1,slow} = (1-f)P_1$ ($P_1 = P_{1,fast} + P_{1,slow}$), where f is the fraction of fast emitted protons. The resulting correlation part will only reflect the fast component $R(k) = f^2 R_{fast}(k)$. With the STCM model they could describe the large momentum component of the correlation function ($840 < p < 1230$ MeV/c) rather good, which is displayed in the left panel of Figure 5.11 and was according to [Ver02] virtually identical to the imaging curve (imaging is a technique to obtain the source size from a measured correlation function by numerically inverting the Koonin-Pratt equation). However, the STCM model was also not able to describe the slow correlation part ($270 < p < 390$ MeV/c) as seen in Figure 5.11 in the

right plot (the dot dashed line is the correlation function using a Gaussian source whereas the solid line represents the STCM model). In this range the correlation function includes significant contributions from long lived proton sources.

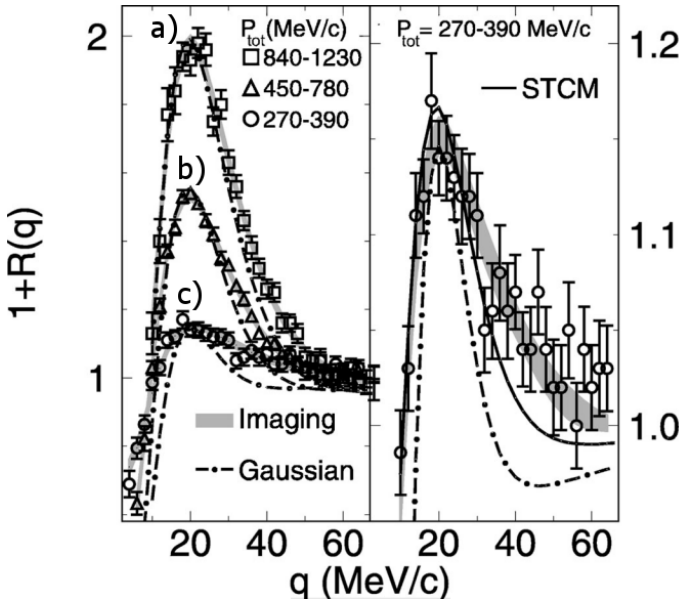

Figure 5.11: Comparison of measurements of experimental correlation functions obtained from ^{14}N+^{197}Au collisions at $E/A = 75$ MeV extracted from [Ver02]. The Gaussian source parametrization fails in all cases to describe the data. The right plot shows results from the STCM model, which is in better agreement with the data.

We can also apply the STCM model to our measured proton-proton correlation signal. For this purpose we weight the correlated part $R(k)$ with a fraction of fast protons $R(k) \rightarrow f^2 R(k)$ in the Koonin model. We have chosen $f^2 = 0.7$ and $R_g = 1.6$ fm to reproduce the peak height. For this parameter set the correlation function is more in agreement with the long tail $k > 20$ MeV/c, but there is still room for improvement especially at very low momenta shown in Figure 5.12.

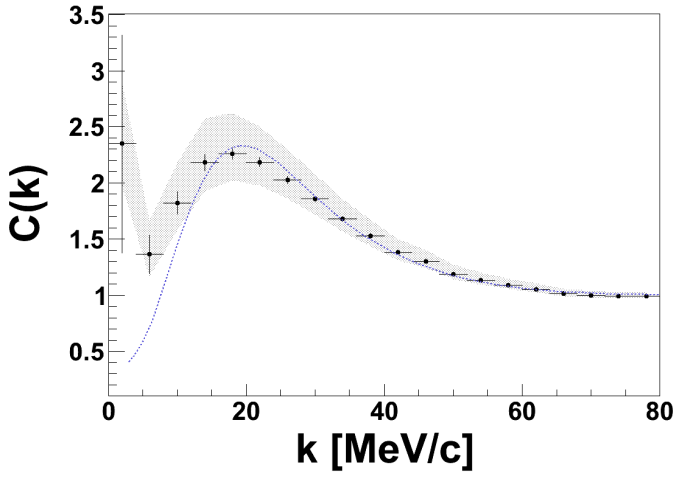

Figure 5.12: Applying the STCM model to the measured correlation function. The tail of the function is in better agreement, but the model fails to describe the part of low momenta.

The conclusion of [Ver02] is, that accurate information from correlation functions, when there are contributions from long lived sources, could be best obtained without making *a priori* assumptions about the emitting source. As stated above, there exist possibilities to extract the source size from a measured correlation function by a numerical inversions of the Koonin-Pratt equation (by discretizing it). A result of applying the inversion technique on the three measured correlation functions (given in three different momentum intervals) displayed in the left panel of Figure 5.11 is shown in Figure 5.13 (everything calculated by [Ver02]). The correlation functions *a*),*b*),*c*) of Figure 5.11 correspond to the sources *a*),*b*),*c*) in Figure 5.13.

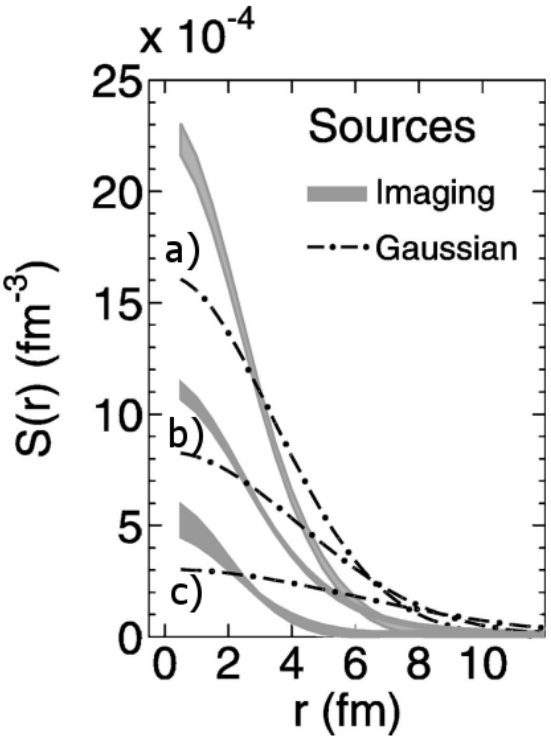

Figure 5.13: Inversion technique applied to the three measured correlation curves from [Ver02]. One can see the deviations from the Gaussian assumption of the emitting source and the source obtained by the inversion technique.

The Gaussian source assumption deviates clearly from the sources obtained by numerical inversion. This is a strong hint that the measured correlation functions in Figure 5.11 consist of contributions of protons of two different time scales. To come back to the measured correlation function in Figure 5.10, we saw that also in this case the assumption of a purely Gaussian source was not able to describe the data. This may also be an indication that we have to consider two different emission time scales and this will be checked in further investigations by calculating the experimental correlation function in different momentum intervals.

5.4 Comparison with simulations

Normally transport models are compared to experimental data using kinematic variables like p_t distributions. But there are also studies using correlation functions for comparison

with experimental measurements e.g. testing the influence of the asymmetry energy on the particle correlation [Kil11] in heavy ion collisions. With the just presented experimental proton-proton correlation function we can investigate the implementation of proton emissions in microscopic models in the p+Nb system.

5.5 Final state interactions in transport and source size of p+Nb

As discussed, correlations are induced by final state interactions after the particles leave the source. Transport theoretical models are based on classical Monte Carlo simulations and for this reason they cannot incorporate wavefunction (anti-)symmetrization between particles, which is of quantum statistical origin [Bys04]. But there are two methods to include this correlations afterwards. One method is to weight the particles e.g. identical bosons with a two-boson weight:

$$w_{ij} = 1 + \cos((p_i - p_j) \cdot (x_i - x_j)), \tag{5.12}$$

using particle momenta and coordinates at freeze-out. The second method which we will apply is to use so called afterburner codes in particular the "Correlation After Burner" (CRAB) from Scott Pratt [CRA00]. It uses single-particle phase space points at freeze-out generated with semi-classical transport codes. CRAB will calculate correlation functions with this particle information together with the knowledge of the impact parameter. Unfortunately, GiBUU does not provide the information of the freeze-out coordinates, so we were only able to test UrQMD. In GiBUU one would also be able to test the indirect influence of a kaon-nucleon potential (which should influence also the Λ because of strangeness conservation) or the influence of the Λ-nucleon force on a correlation function.
In the hybrid model of UrQMD+CRAB we can switch on the forces separately which are included in the proton-proton correlation function. To visualize their contributions we made on the one hand simulations, which contained only the electromagnetic and Pauli force, which are responsible for the suppression and on the other hand simulations with the strong force only which is responsible for the positive correlation signal. Both results are displayed in Figure 5.14.

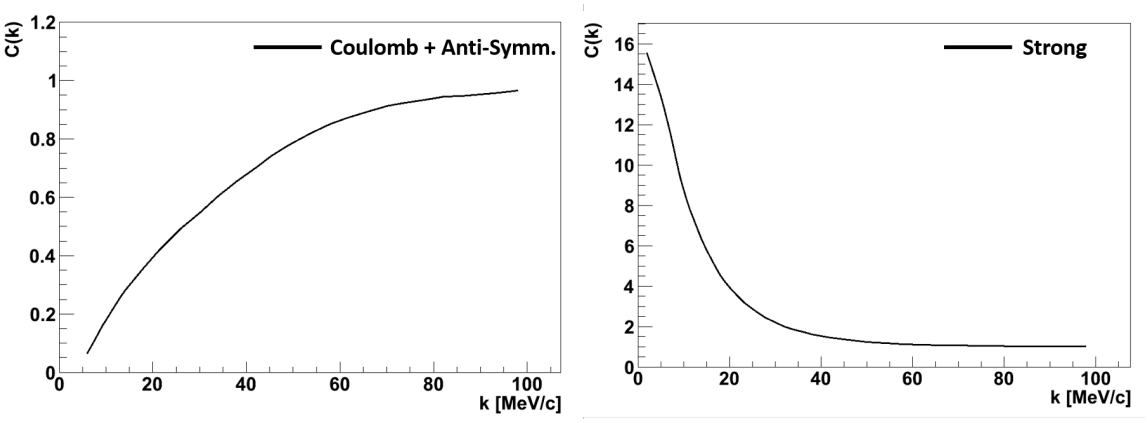

Figure 5.14: Contributions of the three forces to the correlation function. Left: Suppression due to Pauli blocking and the Coulomb force. Right: Positive signal induced by the strong S-wave nuclear interaction.

We see that the positive correlation signal, which is caused by the nuclear S-wave interac-

tion, would be still present and large at very low relative momenta k if electromagnetic and Pauli forces would be absent, which is a typical feature of an attractive strong interaction. The force due to the proton spin together with the Coulomb repulsion gives a suppression which starts already at $k < 100$ MeV/c. The overall proton-proton correlation function is a convolution of both effects, which explains its characteristic shape.

We can now compare the full correlation function generated with CRAB from UrQMD phase space points with the experimental results, which is done in Figure 5.15.

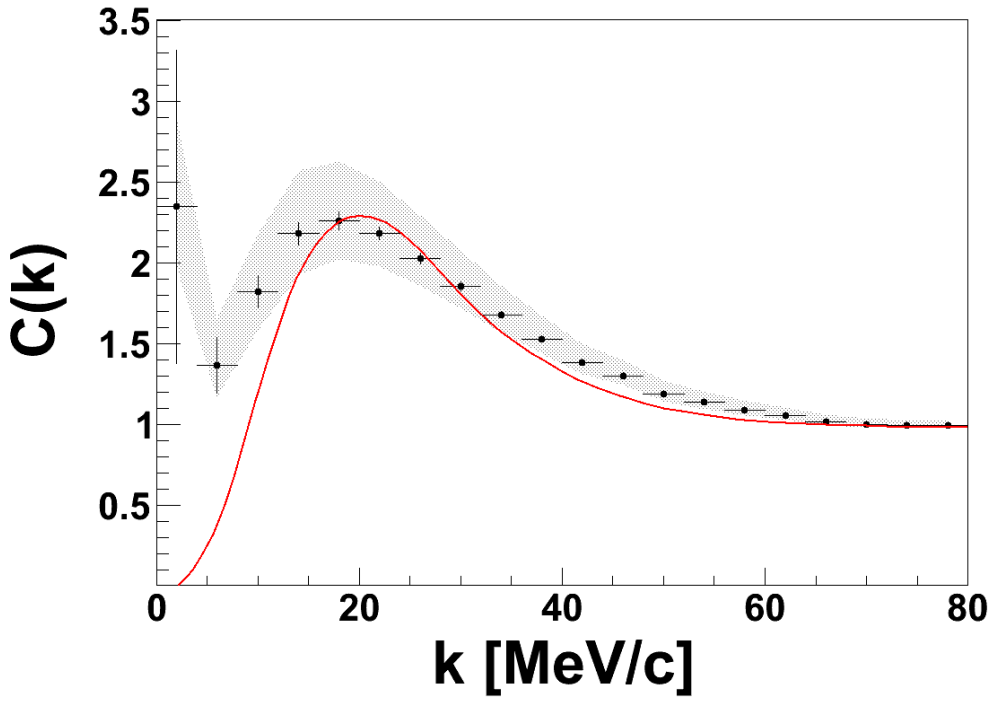

Figure 5.15: Comparison of the experimental curve with predictions from UrQMD (red).

The hybrid model of UrQMD+CRAB is also able to reproduce the height of the correlation function, which is the Gaussian source size of the p+Nb system. But also in this case the width is not in agreement with the theoretical model and needs a more detailed investigation.

5.5.1 Time dependence of the source

We have seen that UrQMD reproduces the height of the correlation function, which is the time-integrated function of all pairs emitted during the whole reaction. In simulations we are able to ask for protons which are emitted at a certain time from the source. This gives us the possibility to study a time dependent correlation function and extract a time dependent Gaussian radius $R(t)$. Figure 5.16 shows the freeze-out time for protons according to UrQMD simulations for the p+Nb system. Most protons stop to interact and are emitted from the source at $t \approx 13$ fm/c.

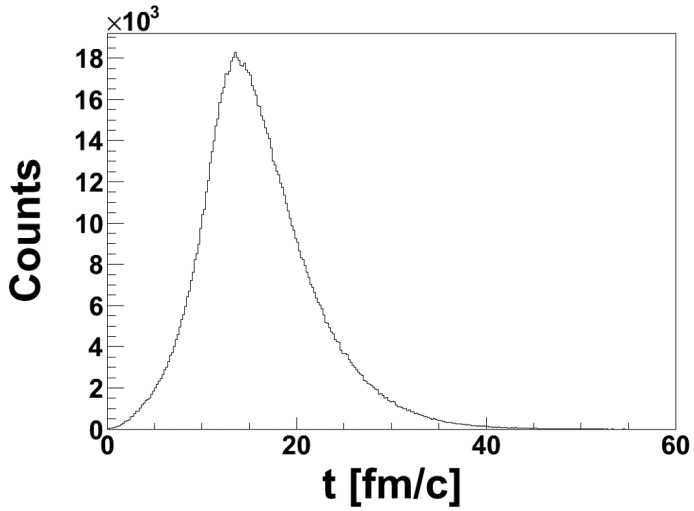

Figure 5.16: Freeze-out time distribution for protons in the p+Nb system. Most protons leave the source at $t \approx 13$ fm/c.

We can also plot the proton distribution in the laboratory frame for the whole freeze-out time evolution to see how protons are distributed in the coordinate space. This is done in Figure 5.17 (for very central events $b = 0 - 1$ fm).

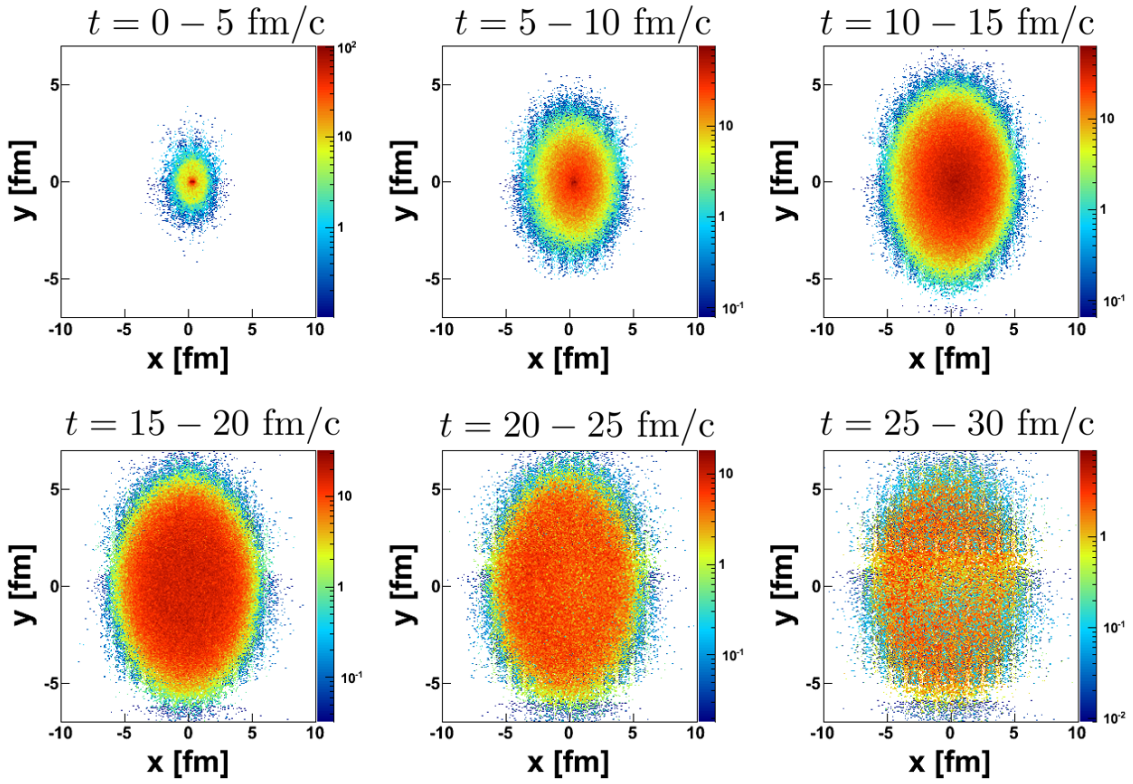

Figure 5.17: Distribution of UrQMD simulated protons in the coordinate space at different time intervals. The proton cloud expands during the time and dissolves in the last time bin.

The protons are very localized at the beginning of the reaction. Then the proton cloud starts to expand and dissolves at a time of about $t > 25$ fm/c. For this reason we would expect that also the source size increases with time. To investigate this hypothesis we can determine the correlation function from UrQMD simulations with CRAB at every time step and calculate the Gaussian source radius by comparing it to predictions from the Koonin model. In doing so we get the plot shown in Figure 5.18.

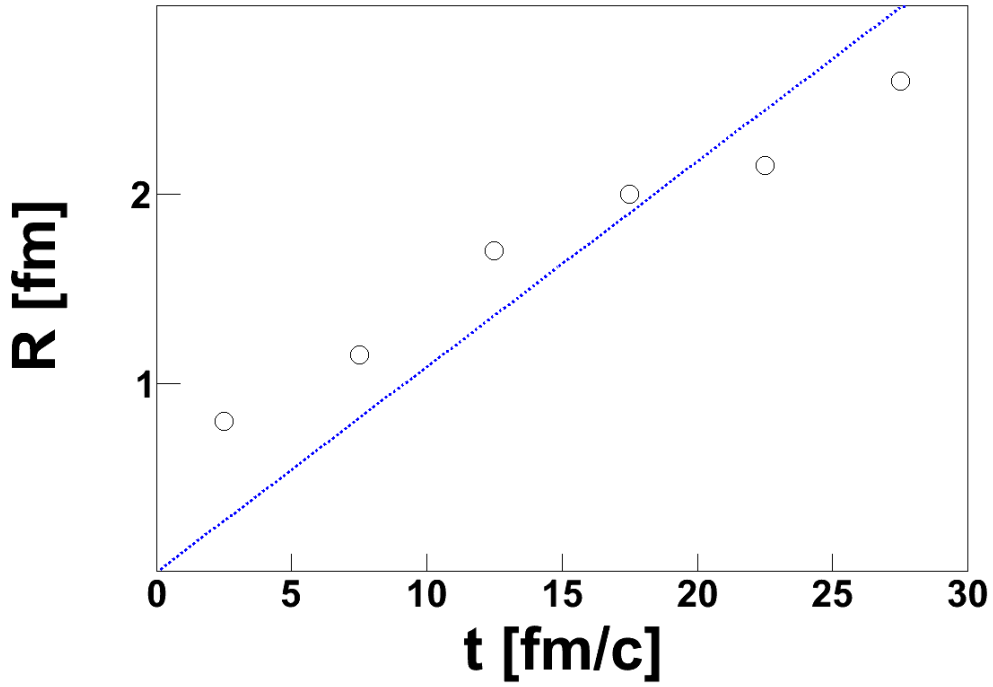

Figure 5.18: Gaussian source size as a function of the freeze-out time for protons simulated with UrQMD. The source size increases with the freeze-out time (almost linearly indicated by the blue dashed line).

The source size increases as expected in an almost linear behaviour. We fitted the trend of the data points with a straight line assuming that we do not have a source at zero freeze-out time. The slope of the line gives us a rough estimation of the velocity:

$$R_g(t) = v \cdot t, \; v \approx 0.11c \tag{5.13}$$

which is about 11% of the speed of light. This means that during the reaction the length at which the protons are influenced by each other due to final state interactions grows with time. If protons are emitted later from the source it is more probable that they are correlated.

6 Summary and Outlook

We discussed in the first part of this thesis the production of Λ hyperons in p+Nb reactions at a kinetic proton energy of 3.5 GeV. After processing $\sim 3.15 \cdot 10^9$ downscaled events we extracted about 1M Λ hyperons. This allowed us, to carry out a double differential analysis of the Λ phase space ($p_t \in$ [0,975] MeV/c, $y_{CM} \in [-1,0.2]$), which was on the one hand important to perform a reliable efficiency correction and on the other hand we were able to investigate the predictions of transport models in a very detailed way.
We compared two different transport models with experimental data, the UrQMD and GiBUU model. UrQMD gave reasonable results and described the trend of the experimental data over the whole two-dimensional phase space $dN/dp_t dy_{CM}$. However, the production of Λ hyperons was overestimated by the model in p+p reactions (too large cross sections) as well as in p+Nb, which became clearly visible at the edges of the experimental Λ phase space. In future investigations of the UrQMD model one has to check the influence of the resonance widths and their production cross sections by comparing it with measured p+p data. Only if the production in nucleon-nucleon collisions is described by the model, it makes sense to look at secondary processes. Nevertheless, it seems that the Λ absorption is better implemented in UrQMD because the model also populates the Λ phase space at lower rapidities. The big difference to the GiBUU model is that UrQMD produces explicitly resonances e.g. N^*s which can interact with other nucleons in the nucleus. The decaying resonance produces then the Λ hyperon. This effect might be the big advantage of the UrQMD model in comparison to the GiBUU model, which produces the particles from a phase-space parametrization of cross sections and has not the intermediate stage of resonance production inside (for strangeness). Also a work by the COSY-TOF collaboration [Abd10] showed that in the $pp \rightarrow \Lambda p K^+$ channel it is favored to produce intermediate resonances $pp \rightarrow NN^*$. An additional effect we have to take into account is that there exists the possibility that intermediate produced resonances can interfere with each other, which can be investigated with a partial wave analysis [Ani12]. This can be checked in p+p reactions in future and may also have an effect on the p+Nb spectra.
The GiBUU model delivered a worse agreement with the experimental data. The tuning of the production cross sections influenced only large rapidities and in this region it seems possible that the model can be tuned to the experimental data with a proper production scaling. This strengthens again the need of p+p data to perform this tuning. The next step after this production tuning is, to implement the absorption of Λs correctly with investigating in more detail the implemented scattering channels. If in the end GiBUU would be able to describe the data in a good way we could investigate in-medium Λ modifications.
To illustrate what is meant with this strategy, we display a work of an inclusive neutral kaon analysis also done in the p+Nb system at the same proton kinetic beam energy of 3.5 GeV, where the production and scattering implementations of GiBUU was tuned to describe the inclusive K^0 yield for the whole two-dimensional phase space (p_t,y) [Lap13] [Ber13].
For the kaon-nucleon interaction theoretical predictions exist that claim that neutral kaons

should feel a repulsive potential of $U_{KN}(\rho = \rho_0)_{k=0} \approx 35$ MeV if embedded in a medium [Pra07]. The interaction for kaons with a medium is displayed in Figure 6.1, showing the in-medium dispersion relation calculated with a relativistic mean-field and a chiral model as a function of the system density [Pra07].

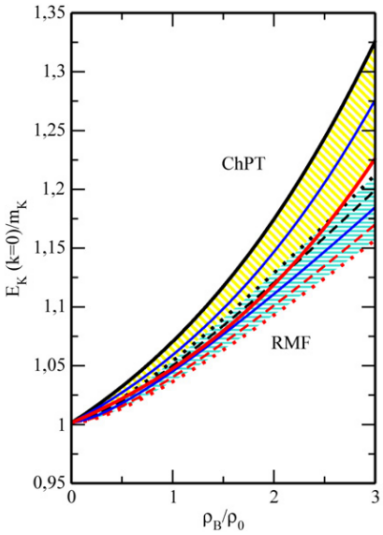

Figure 6.1: Repulsive neutral kaon potential calculated with a relativistic mean field and a chiral model. The repulsive potential value for kaons at rest is about 35 MeV at saturation density according to [Pra07].

The kaon-nucleon interaction is implemented with the chiral realization in the GiBUU model. It is possible to test the effect of the repulsive potential with simulations, where the interaction is switched on, and compared to a reference simulation without the potential. The results for the experimental two dimensional (p_t,y_{CM}) K^0 phase space (black dots) compared to a GiBUU model with the two different above mentioned simulation runs are presented in Figure 6.2.

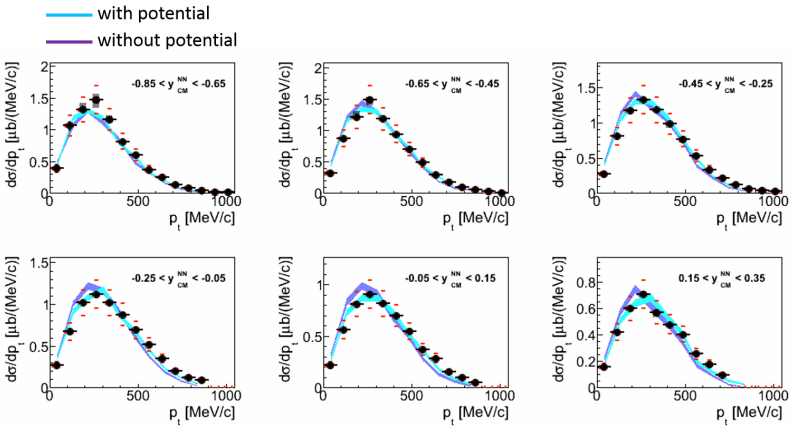

Figure 6.2: Two-dimensional phase space of an inclusive K^0 analysis performed in the HADES collaboration in the p+Nb system at a proton kinetic energy of 3.5 GeV [Lap13] [Ber13]. A comparison with GiBUU data shows that the model with a kaon-nucleon potential (cyan) included is more in agreement with experimental measurements.

The GiBUU model with a kaon-nucleon interaction (cyan) in Figure 6.2 is more in

agreement with the experimental data. This shows the principle, how potential effects are studied.
Even if the model is not able to describe the Λ data we can ask the question, if potential effects would be generally visible. In GiBUU, baryons interact with a Skyrme type potential. For protons and neutrons the single-particle potential reads ($i = n,p$) [Bus12]:

$$U_i(x,\mathbf{p}) = U_N(x,\mathbf{p}) + d_{symm}\frac{\rho_p(x) - \rho_n(x)}{\rho_0}\tau_i^3, \tag{6.1}$$

where $\tau_p^3 = 1$, $\tau_n^3 = -1$ and d_{symm} is the potential symmetry energy coefficient which is chosen to reproduce the symmetry energy in the Bethe-Weizsäcker-mass formula (leads to $d_{symm} \simeq 30$ MeV) [Bus12]. The potential U_N is the isospin averaged nucleon potential:

$$U_N(x,\mathbf{p}) = \frac{U_n + U_p}{2} = A\frac{\rho(x)}{\rho_0} + B\Big(\frac{\rho(x)}{\rho_0}\Big)^{\gamma} + \frac{2C}{\rho_0}\sum_{i=n,p}\int\frac{gd^3p'}{(2\pi)^3}\frac{f_i(x,\mathbf{p}')}{1+(\mathbf{p}-\mathbf{p}')^2/\Lambda^2}\,. \tag{6.2}$$

The six free parameters $A, B, C, \gamma, \Lambda, d_{symm}$ are fixed to fulfill several conditions (e.g. the condition that we stated above for d_{symm}). For particles with strangeness content the model uses a quark scaling assumption, namely, that strange baryons mainly interact with their non-strange quark content, which means the single-particle potential is scaled by a factor 2/3 (for one strange quark) $U_Y = 2U_N/3$. We can set this scaling to zero, which means that Λ hyperons stop interacting with the other nucleons via a Skyrme force (scattering is for sure still present). The result of this effect for the whole phase space is displayed in Figure 6.3, where the green curve corresponds to a simulation run with a Λ-nucleon interaction, whereas in the red curve the interaction was switched off.

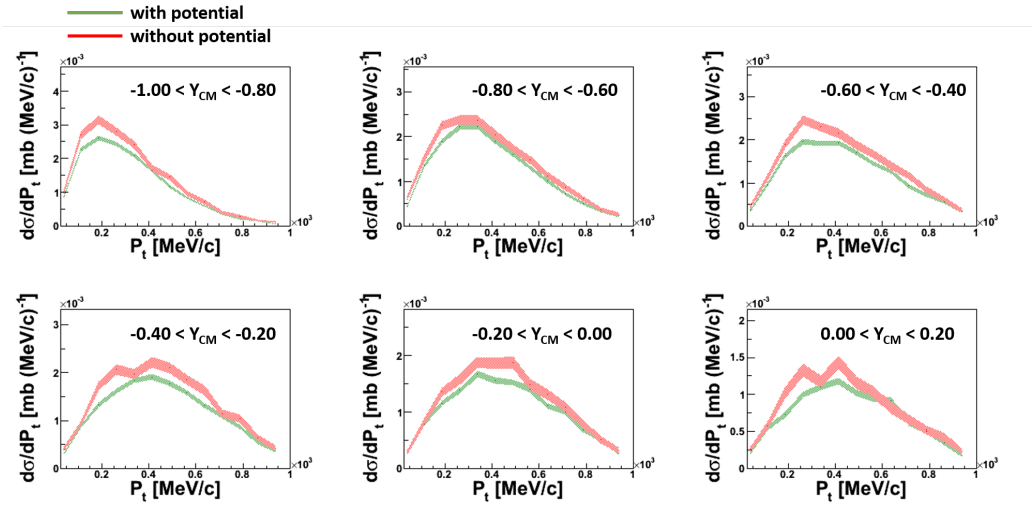

Figure 6.3: GiBUU simulations for Λ hyperons with Λ-nucleon interaction (green) compared to the case where the Skyrme interaction is switched off (red).

The curves in Figure 6.3 for the two different simulations are in principle distinguishable. This is a promising result, because it means that potential effects could also be extracted from the inclusive Λ analysis after the tuning is done.
If all this work will be done, we have tuned the production mechanism of Λs in p+A reactions where the environment is well known. We are then equipped to apply the models

to the more complex reactions of heavy ion collisions (e.g. Au+Au collisions measured with HADES), where we have to deal with evolving systems.

In the second part of this thesis we presented results of two-particle correlations between protons. We explained the mechanisms which are responsible for particle correlations and compared the experimental proton-proton correlation results to the theoretical Koonin model as well as to the microscopic UrQMD transport code. The height of the correlation function was reproduced by the model using a Gaussian source size of $R_g = 2.2^{+0.23}_{-0.22}$ fm, which was the outcome of UrQMD simulations. However, a conjecture of a Gaussian source seems to be a not fully realized approximation indicated by the width of the experimental correlation function. We discussed the problem of non-Gaussian sources with arguments taken from [Ver02], which constructed a model with the assumption that the shape of the proton source is different for protons that are emitted at completely different time scales. They developed a simple two component model (STCM), which fitted better to experimental data. We applied this model also to our measured proton-proton correlation function and also there the model showed slightly a better agreement.
The determination of the proton-proton correlation function was a first step in the analysis. We have now all tools ready which are necessary to calculate correlation functions especially to calculate the mixed event background. The next step would be to construct the more elaborate Λp correlation function in the p+Nb system. We have seen in simulations in chapter 5 that the strong interaction induces a large positive correlation contribution, if the repulsive Coulomb and Pauli interaction would be absent. A correlation function where the latter two are absent and which is only based on strong interactions is the Λ-proton function. A theoretical calculation of the Λp correlation function was performed by [Wan99b]. Their results are displayed in Figure 6.4, which shows in the upper panel the correlations obtained for a Λp pair and for comparison in the lower panel the pp case (as a function of the relative momentum $k = \frac{1}{2}|\mathbf{p}_1 - \mathbf{p}_2|$ in the pair rest frame).

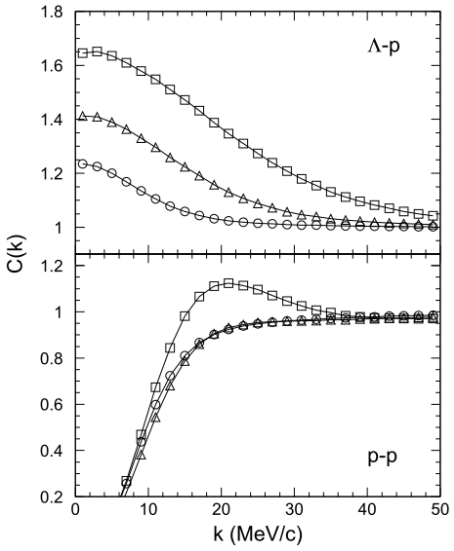

Figure 6.4: Calculation of the Λp (upper panel) and pp (lower panel) correlation function for three different source sizes $R_g = 4$ fm (squares), $R_g = 6$ fm (triangles) and 10 fm (circles) extracted from [Wan99b].

One can see in Figure 6.4 the advantage of the Λp correlation function. At larger source sizes $R_g > 6$ fm it is still possible to distinguish between different sources, while in the pp case the curves coincide because the anti-correlation dominates. We want to extract the cleaner Λp correlation function from Λs produced in the p+Nb system in future. It is then possible to study effects purely based on strong interactions without the suppressions as in the proton-proton case.
We calculated already the Λp correlation function with UrQMD simulations and the CRAB model for the p+Nb system. The result is displayed in Figure 6.5. The correlation function shows the expected behaviour of a positive correlation signal due to the strong nuclear interaction at low relative momenta.

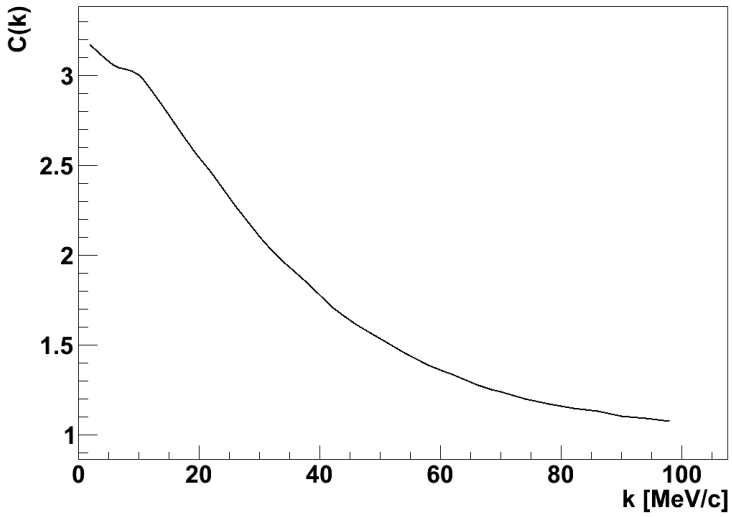

Figure 6.5: Λp correlation function obtained from UrQMD+CRAB for the p+Nb reaction, which shows the expected behaviour of a positive correlation signal at small relative momenta k.

Bibliography

[Abd10] M. Abdel-Bary.
Production of Λ and Σ^0 hyperons in proton-proton collisions.
Eur. Phys. J., A 46:27–44, 2010.

[Ada06] J. Adams et al.
Proton-lambda correlations in central Au+Au collisions at $\sqrt{s_{NN}} = 200$ GeV.
Phys. Rev., C 74:064906, 2006.

[Aga09] G. Agakishiev et al.
The high-acceptance dielectron spectrometer HADES.
Eur. Phys. J., A 41:243–277, 2009.

[Aga10] G. Agakishiev et al.
In-medium effects on K0 mesons in relativistic heavy-ion collisions.
Phys. Rev., C 82:044907, 2010.

[Aga11a] G. Agakishiev.
pp and $\pi\pi$ intensity interferometry in collisions of Ar+KCl at 1.76 AGeV.
Eur. Phys. J., A 47:63, 2011.

[Aga11b] G. Agakishiev et al.
Hyperon production in Ar+KCl collisions at 1.76A GeV.
Eur. Phys. J., A 47:21, 2011.

[Aga13] G. Agakishiev et al.
Inclusive pion and eta production in p+Nb collisions at 3.5 GeV beam energy.
Phys. Rev., C 88:024904, 2013.

[Aic85] J. Aichelin and Che Ming Ko.
Subthreshold kaon production as a probe of the nuclear equation of state.
Phys. Rev. Lett., 55:2661, 1985.

[Alv04] H. Alvarez Pol et al.
A large area timing RPC prototype for ion collisions in the HADES spectrometer.
Nucl. Intrum. Meth., A 535:277–282, 2004.

[Amb60] V. A. Ambartsumyan and G. S. Saakyan.
The degenerate superdense gas of elementary particles.
Sov. Astron., 4:187–201, 1960.

[Ani12] A. V. Anisovich.
Properties of baryon resonances from a multichannel partial wave analysis.
Eur. Phys. J., A 48:5, 2012.

[Bar01] J. Barrette et al.
Lambda Production and flow in Au+Au collisions at 11.5A GeV/c.
Phys. Rev., C 63:014902, 2001.

[Bas98] S. A. Bass et al.
Microscopic models for ultrarelativistic heavy ion collisions.
Prog.Part.Nucl.Phys, 41:255–369, 1998.

[Bay98] G. Baym.
The physics of Hanbury Brown-Twiss intensity interferometry: From stars to nuclear collisions.
Acta Physica Polonica, B 29:1839–1884, 1998.

[Ben09] M. L. Benabderrahmane et al.
Measurement of the in-medium K0 inclusive cross section in π^--induced reactions at 1.15 GeV/c.
Phys. Rev. Lett., 102:182501, 2009.

[Ber13] J. C. Berger-Chen.
private communication, 2013.

[Bet30] H. Bethe.
Theory of the passage of fast corpuscular rays through matter.
Annalen Phys, 5:325–400, 1930.

[Ble99] M. Bleicher et al.
Relativistic hadron-hadron collisions in the ultra-relativistic quantum molecular dynamics model.
J. Phys. G: Nucl. Part. Phys., 25:1859–1896, 1999.

[Bus12] O. Buss et al.
Transport-theoretical description of nuclear reactions.
Phys. Rept., 512:1–124, 2012.

[Bys04] *Modeling Bose-Einstein correlations in heavy ion collisions at RHIC*, 2004.

[Cha13] N. Chamel, P. Haensel, J. L. Zdunik, and F. Fantina.
On the maximum mass of neutron stars.
Int. J. Mod. Phys., E 22:1330018, 2013.

[CRA00] CRAB.
http://www.pa.msu.edu/∼pratts/freecodes/crab/home.html.
2000.

[Dem10] P. Demorest et al.
Shapiro delay measurement of a two solar mass neutron star.
Nature, 467:1081–1083, 2010.

[Dja10] H. Djapo and B.-J. Schaefer and J. Wambach.
Appearance of hyperons in neutron stars.
Phys. Rev., C 81:035803(11), 2010.

[Elg13] J. Elgeti.
http://web-docs.gsi.de/∼misko/overlap/interface.html.
2013.

[Fuk11] K. Fukushima and T. Hatsuda.
The phase diagram of dense QCD.
Rept. Prog. Phys., 74:014001, 2011.

[Gai13] *In-medium effects on hypernuclear formation*, 2013.

[Gea95] Geant.
http://www.asdoc.web.cern.ch/wwwasdoc/geant_html3/geantall.html.
1995.

[Gil07] A. Gil et al.
Front-end electronics development for the new resistive plate chamber detector of HADES.
JINST, 2:T11001, 2007.

[Gol60] G. Goldhaber, S. Goldhaber, W. Lee, and A. Pais.
Influence of Bose-Einstein statistics on the antiproton-proton annihilation process.
Phys. Rev., 120:300, 1960.

[Gro08] Particle Data Group.
Particle Physics Booklet.
Elsevier, 2008.

[HAD05] HADES Wiki/SimAna.
Normalization with LVL2 Trigger.
2005.

[Han56a] R. Hanbury Brown, and R. Q. Twiss.
A test of a new type of stellar interferometer on sirius.
Nature, 178:1046, 1956.

[Han56b] R. Hanbury Brown, and R. Q. Twiss.
Correlation between photons in two coherent beams of light.
Nature, 177:27–29, 1956.

[HGe08] HGeant.
http://www-hades.gsi.de.
2008.

[Kil11] M. A. Kilburn.
Proton-proton correlation functions as a probe to reaction dynamics.
PhD thesis, Michigan State University, 2011.

[Koo77] S. E. Koonin.
Proton pictures of high-energy nuclear collisions.
Phys. Lett., 70 B:43, 1977.

[Kot04] R. Kotte et al.
Two-proton small-angle correlations in central heavy-ion collisions: A Beam-energy and system-size dependent study.
Eur. Phys. J., A 23:271–278, 2004.

[Lal13] R. Lalik.
private communication, 2013.

[Lap09] K. Lapidus et al.
Dielectron production in *pp* and *dp* collisions at 1.25 GeV/u with HADES.
arXiv:nucl-ex/0904.1128, 2009.

[Lap13] K. Lapidus.
private communication, 2013.

[Led01] *Femtoscopy with unlike particles*, 2001.

[Leo97] A. Leonidov, M. Nardi, and H. Satz.
Hadron spectra from nuclear collisions.
Z. Phys., C 74:535–540, 1997.

[Li,96] G. Q. Li, and C. M. Ko.
Λ flow in heavy-ion collisions: The role of final-state interactions.
Phys. Rev., C 54:1897–1902, 1996.

[Li,98] G.Q. Li, and G.E. Brown.
K^+ versus Λ flow.
Eur. Phys., A 636:487–506, 1998.

[Lis93] M. Lisa.
Impact parameter-gated two-proton intensity interferometry in intermediate energy heavy ion collisions.
PhD thesis, Michigan State University, 1993.

[Lis10] M. Lisa, and S. Pratt.
Femtoscopically probing the freeze-out configuration in heavy ion collisions.
arXiv:0811.1352, 2010.

[Lor12] M. Lorenz.
Vector meson production in p+Nb reactions and statistical particle production in Ar+KCl collisions.
PhD thesis, Johann Wolfgang Goethe-Universität Frankfurt, 2012.

[Mac11] R. Machleidt and D.R. Entem.
Chiral effective field theory and nuclear forces.
Phys. Rept., 503:1–75, 2011.

[Opp39] J. R. Oppenheimer and G.M. Volkoff.
On massive neutron cores.
Phys. Rev., 55:374–381, 1939.

[Pra84] S. Pratt.
Pion interferometry for exploding sources.
Phys. Rev. Lett., 53:1219–1221, 1984.

[Pra87] S. Pratt, M. B. Tsang.
Viewing the liquid-gas phase transition by measuring proton correlations.
Phys. Rev., C 36:2390–2395, 1987.

[Pra07] V. Prassa et al.
In-medium effects on particle production in heavy ion collisions.
Nucl. Phys., A 789:311–333, 2007.

[Sah63] G. S. Sahakian and Yu. L. Vartanian.
On the possible phase states of matter at extremely high densities.
Il Nuovo Cimento, 30:82–104, 1963.

[Sak94] J. J. Sakurai.
Modern quantum mechanics.
Addison-Wesley, 1994.

[Sch08a] J. Schaffner-Bielich.
Hypernuclear physics for neutron stars.
Nucl. Phys., A 804:309–321, 2008.

[Sch08b] A. Schmah.
Produktion von Seltsamkeit in Ar+KCl Reaktionen bei 1.756 AGeV mit HADES.
PhD thesis, Technische Universität Darmstadt, 2008.

[Sie13] J. Siebenson.
Strange baryonic resonances below the $\bar{K}N$ threshold - Results from p + p reactions at the HADES experiment.
PhD thesis, Technische Universität München, 2013.

[Sjö07] T. Sjörstrand, S. Mrenna, and P. Skands.
A brief introduction to PYTHIA 8.1.
arXiv:hep-ph/0710.3820, 2007.

[Stu01] C. Sturm et al.
Evidence for a soft nuclear equation-of-state from kaon production in heavy-ion collisions.
Phys. Rev. Lett., 86:39, 2001.

[Tec06] Vector meson production in pA and πA collisions.
Technical Report, 2006.

[Tlu10] P. Tlusty, M. Weber, P. Salabura et al.
Production of charged pions in reaction p+Nb at 3.5 GeV.
Technical report, 2010.

[Tol39] R. G. Tolman.
Static solutions of Einstein's field equations for spheres of fluid.
Phys. Rev., 55:364–373, 1939.

[Tsu99] K. Tsushima, A. Sibirtsev, A. W. Thomas, and G. Q. Li.
Resonance model study of kaon production in baryon baryon reactions for heavy ion collisions.
Phys. Rev., C 59:369–387, 1999.

[van11] M. H. van Kerkwijk, R. P. Breton, and S. R. Kulkarni.
Evidence for a massive neutron star from a radial-velocity study of the companion to the black widow pulsar B1957+20.
Astrophys. J., 728:95, 2011.

[Ver02] G. Verde et al.
Imaging sources with fast and slow emission components.
Phys. Rev., C 65:054609, 2002.

[Vid11] I. Vidaña, D. Logoteta, C. Providência, A. Polls, and I. Bombaci.
Estimation of the effect of hyperonic three-body forces.
Europhys. Lett., 94:1102, 2011.

[Wan99a] Z. S. Wang, Amand Faessler and C. Fuchs and T. Waindzoch.
Lambda collective flow in heavy ion reactions.
Nucl.Phys., A 645:177–188, 1999.

[Wan99b] F. Wang, and S. Pratt.
Lambda-proton correlations in relativistic heavy ion collisions.
Phys. Rev. Lett., 83:3138–3141, 1999.

[Web11] M. Weber.
Dielektronen Spektroskopie in kalter Kernmaterie.

PhD thesis, Technische Universität München, 2011.

[Wei08] J. Weil.
Dilepton production in elementary nuclear reactions within a BUU transport model.
Master's thesis, Justus-Liebig-Universität Giessen, 2008.

[Wei12a] J. Weil, H. van Hees, and U. Mosel.
Dilepton production in proton-induced reactions at SIS energies with the GiBUU transport model.
Eur. Phys. J., A 48:111, 2012.

[Wei12b] S. Weissenborn, D. Chatterjee, and J. Schaffner-Bielich.
Hyperons and massive neutron stars: the role of hyperon potentials.
Nucl. Phys., A 881:62–77, 2012.

[Wei12c] S. Weissenborn, D. Chatterjee, and J. Schaffner-Bielich.
Hyperons and massive neutron stars: vector repulsion and $SU(3)$ symmetry.
Phys. Rev., C 85:065802, 2012.

[Wei13] J. Weil.
private communication, 2013.

[Yuk35] H. Yukawa.
On the Interaction of Elementary Particles.
Proc. Phys.-Math. Soc. Jpn., 17:48, 1935.